Study of the III-nitride based nanostructures

By Hao Tang

Supervisor: Prof. T. Wang

Jan 2014

A Thesis Submitted for the Degree of Doctor of Philosophy in the Department of Electronic and Electrical Engineering of the University of Sheffield

Abstract

The III-nitrides has wide application in opto-electronic devices, including green/blue light-emitting diodes (LEDs), laser diodes and solar cells. This thesis addresses the fundamental issues of these devices from a concern of efficiencies.

InGaN-based LEDs present efficiency losses (droop) at higher injection intensities. By relieving the quantum-confined-stark effect (QCSE), the nanorod structure reduces the electron-longitudinal-optical phonon coupling strength by 40% on average, as measured by the Huang-Rhys Factor. Consequently, a weaker indirect Auger recombination could potentially curb the droop. Besides, surface plasmon polariton–exciton coupling leads to 5.5 times enhancement of the internal quantum efficiency (IQE) and is found to be motivated by the carrier delocalization effect. Both SP and nanorods contribute to high LED efficiencies.

The whispering gallery mode ring cavities are studied in the Finite Difference Time Domain (FDTD) approach in order to design high efficiency nitride laser diodes. For InGaN based rings with a radius of 1000-1500nm, the ideal Q-factor reaches 10^6 at the resonance wavelength around 500nm. The mode splitting effect with separation of bonding and anti-bonding modes is observed as a result of the interference between rings. A 2-3 times enhancement of the Q-factor can be realized when two rings is 25-50nm apart. Q-factors reduce when two rings have a deviation in size.

InGaN based quantum dot (QD) solar cell taking advantages of both the intermediate band solar cell (IBSC) structure and prominent piezoelectric fields in III-nitrides is theoretically researched. The IB provided by QDs increases the short circuit current density, and the piezoelectric field enhances the open circuit voltage. The optimized structure reaches a highest conversion efficiency of 55.4%. The InGaN QD structures are viable for high performance nitride solar cells.

List of Publications

Journal Publications

1. **H. Tang**, T. Wang and B. Liu. Understanding InGaN based intermediate band solar cells considering the piezoelectric fields. In submission to *IEEE Photonic. Tech. L.* in Jan 2014.

2. P. Renwick, **H. Tang**, J. Bai and T. Wang. (2012). Reduced LO-phonon-exciton interaction in InGaN/GaN nanorod structures. *Appl. Phys. Lett.* 100:182105 - 182107

3. P. Renwick, **H. Tang**, Q. Wang, R. Smith and T. Wang. (2011). Enhanced internal quantum efficiency of an InGaN/GaN quantum well as a function of silver thickness due to surface Plasmon coupling. *Phys. Stat. Sol. C*, 8(7-8): 2176-2179

Conference Contributions

1. **H. Tang**, B. Liu and T. Wang. (2013). Theoretical study of GaN/InGaN Intermediate Band solar cells. UK Nitrides Consortium (UKNC) Summer Conference, University of Sheffield, UK

2. **H. Tang**, Y.P. Gong, P. Renwick and T. Wang. (2012). Observing surface Plasmon coupling with InGaN quantum well through temperature dependent photoluminescence. UK Nitrides Consortium (UKNC) Summer Conference, University of Sheffield, UK

3. P. Renwick, **H. Tang**, Y. P. Gong, K. Xing, J. Bai and T. Wang. (2012). Study of LO-phonon and exciton interaction in GaN/InGaN MQW nanorod structures UK Nitrides Consortium (UKNC) Winter Conference, University of Bath, UK

4. P. Renwick, **H. Tang** and T. Wang. (2011). Evaluating Internal Quantum

Efficiency of Green LEDs via Electroluminescence UK Nitrides Consortium (UKNC) Winter Conference, University of Manchester, UK

5. P. Renwick, **H. Tang**, Q. Wang, R. Smith and T. Wang. (2010). Enhanced internal quantum efficiency of an InGaN/GaN quantum well as a function of Ag thickness due to surface Plasmon coupling. International Workshop on Nitride Semiconductors, Tampa, Florida, USA.

Acknowledgements

I'd like to express my deepest thanks to my supervisor, Prof. Wang. He opens a door to the amazing world of gallium nitride through which I'm able to appreciate the essence and beauty of harmony in physics. He also helps me to cultivate a pleasing blend of rigorous, committed, modest and dedicative character. Such positive personalities will be lifelong beneficial in my exploration of future career and life.

I also want to express my sincere thanks to Dr Bin Liu and Dr Qi Wang, who always give me courage to overcome detailed problems in everyday scientific research. Many thanks to Dr Jie Bai for sharing me the schematic diagram of standard nanorod fabrication processes, and to Yipin Gong for growing samples and taking reciprocal space maps. Many thanks to Paul Renwick for fabricating the nanorod structure, sharing the SEM image of the nanorod, fabricating Ag-coated samples, and taking the AFM image of the Ag-coated sample surface. I also appreciate the useful talks and discussion on general physics with my colleagues Dr Yaonan Hou, Dr Taeki Kim, Rick Smith, Kun Xing and Fernando Guzman. The comfortable yet efficient working atmosphere as well as corporative colleagues add to delightful memories of research as being tough and challenging.

And lastly, I would like to express my thanks to my family. With their encouragement tremendous courage springs in my heart, and family is like a peaceful harbor where the young sailor can rest and get refreshed.

Content

1. Introduction

1.1.Development of III-Nitride based optoelectronics application

The research on GaN dates back to 1969 when Maruska et.al[1], for the first time, grew the single crystal GaN film on sapphire substrate by the hydride vapour phase epitaxy (HVPE) technology. Later in 1971, the GaN based blue LEDs fabricated using the metal-insulator-semiconductor type were reported by Pandove et.al[2]. However, before 1986, the research on GaN based LEDs faced two major challenges: obtaining the *p*-type GaN and materials of high quality. Figure 1.1 presents the number of publications on III-nitrides between year 1965- 2000[3].

In 1986, Akasaki et.al. grew a high-quality GaN film on a sapphire substrate using a so-called two-step growth approach[4], which has now been widely used. Later this group also achieved p-GaN which was activated by means of low energy electron beam irradiation (LEEBI)[5]. These two major breakthroughs lead to the fabrication of the world's first GaN based LEDs with p-n junctions in year 1989.

In year 1992, Nakamura et.al. was successful in obtaining *p*-GaN using a very cost-effective approach, namely, annealing under N_2 ambient at a high temperature. This led to realization of the mass production. Subsequently, Nakamura et.al. reported the GaN-based double heterojunction LEDs[6,7]. Since then, the research for III-nitrides optoelectronic devices had started to soar. This corresponds to period (d) in Figure 1.1.

GaN-based LEDs, which can be used to produce a variety of colours or wavelength has become one of the major focuses of III-V nitride optoelectronic devices. Using the idea of fabricating the heterojunction LEDs raised by Nakamura's group, nitride

LEDs in all visible range, such as blue, green and yellow, etc, have been consequently fabricated[8,9]. Since 2000, UV LEDs in the UV spectrum range from 210nm to 380nm have also been reported by different groups[10,11,12].

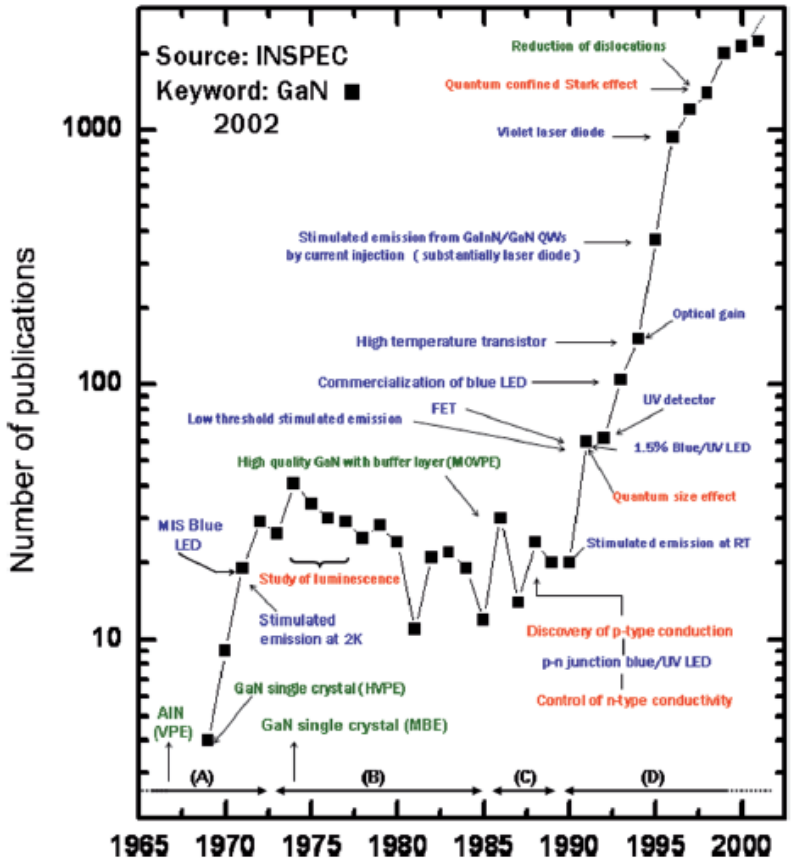

Figure 1.1. Number of yearly publications for III-nitrides during year 1965 – 2000 [3]

Apart from LEDs, the development of InGaN/GaN based laser diode is also remarkable. The first electrically injected laser diode in the blue spectrum range was reported by Nakamura's group in 1996[13]. As the material quality and device structure were being improved, more laser diodes with higher performance were reported[14,15]. The laser diode in the green spectrum range[16]has only been successfully fabricated in recent years. In addition to the conventional Febry-Perot lasing cavity, other lasing mechanism such as the whispering gallery mode has been researched[17,18].

The GaN-based solar cell has been more emphasized since the band gap energy for

InN is found to be around 0.7eV instead of 1.9eV[19]. The wide span of band gap energy for nitrides enables the optimization of solar cell design for a high efficiency[20,21].

1.2. Current challenges in nitrides and research aims of this thesis – a concern of the efficiency

Currently, great challenges in the field of III-nitrides are mainly concerned about the material quality and efficiencies of the nanostructure. The current challenges and corresponding research aims are studied in four separate chapters (Chapter 3 – Chapter 6).

1. The efficiency droop for InGaN/GaN light-emitting diodes (LEDs) is a severe challenge for LED commercialization. Typically, the internal quantum efficiency exhibits a peak value at low injection current density and then drops quickly with further increasing the injection current. This potentially stops a wide application of current GaN-based LEDs.

This study aims to understand the relationship between the efficiency droop and the strain for nitride LEDs. It's found that strain relaxation through fabricating QWs into a nanorod array structure reduces the electron-longitudinal-optical phonon coupling strength, which is closely associated with the Indirect Auger recombination (IAR) process[22]. Therefore, a nanorod structure potentially minimize the efficiency droop[23].

2. Although the surface plasmon(SP)-exciton coupling effect has been widely suggested to improve the internal quantum efficiency of LEDs, the research on the underlying mechanism is still in an early stage. The in-depth understanding of the exciton–SP coupling effect is required.

This study aims to investigate the influence of the exciton delocalization on the

exciton-SP coupling. A model based on the dipole-dipole coupling [24] explains the influence of the in-plane wave-vector on the coupling performance, and the wave vector varies for localized and delocalized excitons at different temperatures.

3. Fabricating high Q-factor Laser diodes (LDs) in the visible spectrum is of great significance, but it is still in its infancy for III-nitrides. The fabrication process for LDs with traditional lasing mechanism is complicated and not economical[25]. Lasing based on the whispering gallery mode (WGM) calls on further research.

This study aims to provide a useful theoretical study of whispering gallery mode InGaN based ring cavities for future experimental research in this group. It gives the optimal ring radius for single WGM InGaN ring cavity and suggests further improvement of Q-factors by employing the mode splitting effect in the array of ring cavities.

4. Nitride based solar cells are expected to be promising due to the wide spectrum span, but performances of the nitride based solar cells reported so far is not satisfactory. While the multiple junction solar cell structure has been successfully adopted for many other material systems, it is not practical for nitrides because of the difficulties in fabricating the *p*-GaN layer in this structure[26]. An alternative method has to be developed to allow for multi-level photon absorption for high solar cell conversion efficiencies.

This study aims at designing the InGaN based quantum dot (QD) solar cell which takes advantages of both the intermediate band solar cell (IBSC) structure and the prominent piezoelectric field in III-nitrides. An optimized structure for InGaN QD IBSC is designed that reaches a highest conversion efficiency of 55.4% for single-level IBSCs. It provides possibilities of fabricating InGaN based solar cells with ultra high energy efficiency.

1.3. Thesis Structure

The thesis focuses on the mechanisms in III-nitride nanostructures and stresses the concern of efficiency for III-nitride opto-electronic devices. This thesis covers the theoretical and experimental research that relates to the mechanisms and efficiencies of GaN/InGaN-based light emitting diodes(LEDs), laser diodes(LDs) and solar cells. Various nanostructures have been covered including the nanorod structures, surface plasmon coupling, whispering gallery mode cavities and intermediate band solar cell structures.

Chapter Two provides a holistic view of the background knowledge for nitrides. Five sections are included in this chapter. Section 2.1 reviews the basic properties of GaN-based materials, and the piezoelectric field is highlighted as an important feature for the nitrides. Section 2.2 is associated with the issue of nanorods which is studied in Chapter 3. This section includes the principles of nanorod structures, the quantum stark confined effect and Auger recombination. Section 2.3 analyzes the basic mechanisms of plasma and surface plasmon for the study in Chapter 4. Section 2.4 introduces the mechanism of cavities, the whispering gallery mode and the definition of the quality factor, which support the theoretical study in Chapter 5. Section 2.5 studies the principles of solar cells, current challenges for the nitride solar cells, basic mechanisms of the intermediate band solar cell (IBSC) and the rationale for quantum dot(QD) IBSC. They support the theoretical work on InGaN QD-IBSCs for Chapter 6.

Chapter Three is focused on the experimental work on InGaN QW nanorod structures using the temperature dependent photoluminescence (PL) measurement. The first section studies the emission energy and line-width (full width half maximum, or FWHM) for the nanorod structure. The second section further probes the effect of nanorod structures in reducing the electron-phonon coupling as measured by the Huang-Rhys factor.

Chapter Four studies the relationship between the exciton-SP coupling and the exciton delocalization process. The first section highlights the essence of exciton-SP coupling and the lack of research on the influence of exciton delocalization on SP coupling . The second section presents the work using the temperature dependent PL measurement. The effect that exciton-SP coupling is enhanced by the exciton delocalization process is explained.

Chapter Five studies the InGaN-based whispering gallery mode (WGM) ring cavities theoretically. The first section explains the finite difference time domain (FDTD) approach and studies the quality factors (Q-factors) for single InGaN-based WGM ring cavity. The second section studies the mode splitting effect in a pair of rings close to each other. The mechanism for mode splitting, scales of mode split energy and influences on the Q-factor are analyzed in details.

Chapter Six studies the InGaN QD intermediate band solar cell (IBSC) theoretically. The first section explains the basic mechanism for InGaN QD-IBSCs and gives the optimized band structure calculated by the $k \cdot p$ method. The second section explains the influence of the piezoelectric field on the open circuit voltage of solar cells, which is an important feature for InGaN QD IBSCs. In the third section, the current-voltage functions are applied to the optimized InGaN QD-IBSC and the solar cell conversion efficiencies are obtained.

Chapter Seven is the chapter of conclusion. It once again highlights the contribution of the work in this thesis on the various III-nitride based nanostructures. A short plan of future research tasks is also stated in order to improve the quality of the III-nitride nanostructures and efficiencies of III-nitride based opto-electronic devices.

Reference

[1] Maruska, H. P., & Tietjen, J. J. (1969). The preparation and properties of vapor-deposited single-crystal-line GaN. *Appl. Phys. Lett.*, 15(10):327-329

[2] Pankove, J. I., Miller, E. A., & Berkeyheiser, J. E. (1971). GaN electroluminescent diodes. IEEE In *Electron Devices Meeting, 1971 International* 17: 78-79

[3] Takahashi, K., Yoshikawa, A., & Sandhu, A. (Eds.). (2007). *Wide bandgap semiconductors: fundamental properties and modern photonic and electronic devices*. New York: Springer. pp, VII

[4] Amano, H., Sawaki, N., Akasaki, I., & Toyoda, Y. (1986). Metalorganic vapor phase epitaxial growth of a high quality GaN film using an AlN buffer layer. *Appl. Phys. Lett.*, 48:353-355

[5] Amano, H., Kito, M., Hiramatsu, K., & Akasaki, I. (1989). P-type conduction in Mg-doped GaN treated with low-energy electron beam irradiation (LEEBI). *Jpn. J. Appl. Phys*, 28(12): L2112-L2114

[6] Nakamura, S., Mukai, T., Senoh, M., & Iwasa, N. (1992). Thermal annealing effects on p-type Mg-doped GaN films. *Jpn. J. Appl. Phys*, 31(2B), L139-L141

[7] Nakamura, S., Senoh, M., & Mukai, T. (1993). P-GaN/N-InGaN/N-GaN double-blue-light-emitting diodes. *Jpn. J. Appl. Phys*, 32: L8-L10

[8] Nakamura, S., Senoh, M., Iwasa, N., & Nagahama, S. I. (1995). High-brightness InGaN blue, green and yellow light-emitting diodes with quantum well structures. *Jpn. J. Appl. Phys.*, 34(7): L797-L799

[9] Mukai, T., Yamada, M., & ShujiNakamura, S. (1999). Characteristics of InGaN-

based UV/blue/green/amber/red light-emitting diodes. *Jpn. J. Appl. Phys.*, 38: 3976-3978

[10] Taniyasu, Y., Kasu, M., & Makimoto, T. (2006). An aluminium nitride light-emitting diode with a wavelength of 210 nanometres. *Nature*, *441*(7091), 325-328

[11] Wang, T., Lee, K. B., Bai, J., Parbrook, P. J., Airey, R. J., Wang, Q., & Cullis, A. G. (2006). Greatly improved performance of 340nm light emitting diodes using a very thin GaN interlayer on high temperature AlN buffer layer. *Appl. Phys. lett.* 89(8): 081126-081128

[12] Yasan, A., McClintock, R., Mayes, K., Darvish, S. R., Kung, P., & Razeghi, M. (2002). Top-emission ultraviolet light-emitting diodes with peak emission at 280 nm. *Appl. Phys. Lett.* 81(5):801-803

[13] Nakamura, S., Senoh, M., Nagahama, S. I., Iwasa, N., Yamada, T., Matsushita, T., & Sugimoto, Y. (1996). InGaN-based multi-quantum-well-structure laser diodes. *Jpn. J. Appl. Phys.*, 35 (1): L74-L76

[14] Iida, K., Kawashima, T., Miyazaki, A., Kasugai, H., Mishima, S., Honshio, A., & Akasaki, I. (2004). 350.9 nm UV laser diode grown on low-dislocation-density AlGaN. *Jpn. J. Appl. Phys.* 43: 499-501

[15] Yoshida, H., Yamashita, Y., Kuwabara, M., & Kan, H. (2008). A 342-nm ultraviolet AlGaN multiple-quantum-well laser diode. *Nature Photonics*, *2*(9): 551-554

[16] Miyoshi, T., Masui, S., Okada, T., Yanamoto, T., Kozaki, T., Nagahama, S. I., & Mukai, T. (2009). 510--515 nm InGaN-Based Green Laser Diodes on c-Plane GaN Substrate. *Appl. Phys. Express*,2: 062201-062203

[17] Choi, H. W., Hui, K. N., Lai, P. T., Chen, P., Zhang, X. H., Tripathy, S., ... &

Chua, S. J. (2006). Lasing in GaN microdisks pivoted on Si. *Appl. Phys. Lett.,* 89(21): 211101-211103

[18] Tamboli, A. C., Schmidt, M. C., Hirai, A., DenBaars, S. P., & Hu, E. L. (2009). Observation of whispering gallery modes in nonpolar m-plane GaN microdisks. *Appl. Phys. Lett.*,94(25): 251116-251118

[19]Wu, J., Walukiewicz, W., Yu, K. M., Ager Iii, J. W., Haller, E. E., Lu, H., & Nanishi, Y. (2002). Unusual properties of the fundamental band gap of InN. *Appl. Phys. Lett.*, 80:3967-3970

[20] Honsberg, C., Jani, O., Doolittle, A., Trybus, E., Namkoong, G., Ferguson, I., & Payne, A. (2004, June). InGaN–A new solar cell material. In *Proceedings of the 19th European Photovoltaic Science and Engineering Conference, Paris, France*, 15-20

[21] Wu, J., Walukiewicz, W., Yu, K. M., Shan, W., Ager Iii, J. W., Haller, E. E., & Kurtz, S. (2003). Superior radiation resistance of InGaN alloys: Full-solar-spectrum photovoltaic material system. *J. Appl. Phys.*, 94: 6477-6450

[22] Kioupakis, E., Rinke, P., Delaney, K. T., & Van de Walle, C. G. (2011). Indirect Auger recombination as a cause of efficiency droop in nitride light-emitting diodes. *Appl. Phys. Lett.*, 98(16):161107-161109

[23] Renwick, P., Tang, H., Bai, J., & Wang, T. (2011). Reduced longitudinal optical phonon-exciton interaction in InGaN/GaN nanorod structures. *Appl. Phys. Lett.*, 100(18): 182105-182108

[24] Rindermann, J. J., Pozina, G., Monemar, B., Hultman, L., Amano, H., & Lagoudakis, P. G. (2011). Dependence of resonance energy transfer on exciton dimensionality. *Phys. Rev. Lett.*, 107(23): 236805-236809

[25] Li, K. H., Ma, Z., & Choi, H. W. (2011). High-Q whispering-gallery mode

lasing from nanosphere-patterned GaN nanoring arrays. *Appl. Phys. Lett.*, 98(7): 071106-071108

[26] Yamamoto, A., Islam, M. R., Kang, T. T., & Hashimoto, A. (2010). Recent advances in InN-based solar cells: status and challenges in InGaN and InAlN solar cells. *Phys. Status Solidi C*, 7(5): 1309-1316

2. Background

2.1. Basic properties of GaN

2.1.1 Crystal structure

III-Nitrides typically exhibit a wurtzite crystal structure[1]. The schematic diagram for wurtzite GaN is shown in Figure 2.1. The blue atoms representing Ga atoms and the red atoms representing N atoms form the hexagonal close packed layers. The Ga atoms can also be replaced by other atoms such as In and Al in the wurtzite crystal structure. The two parameters *a* and *c* satisfies: $c/a = (8/3)^{1/2} \approx 1.633$.

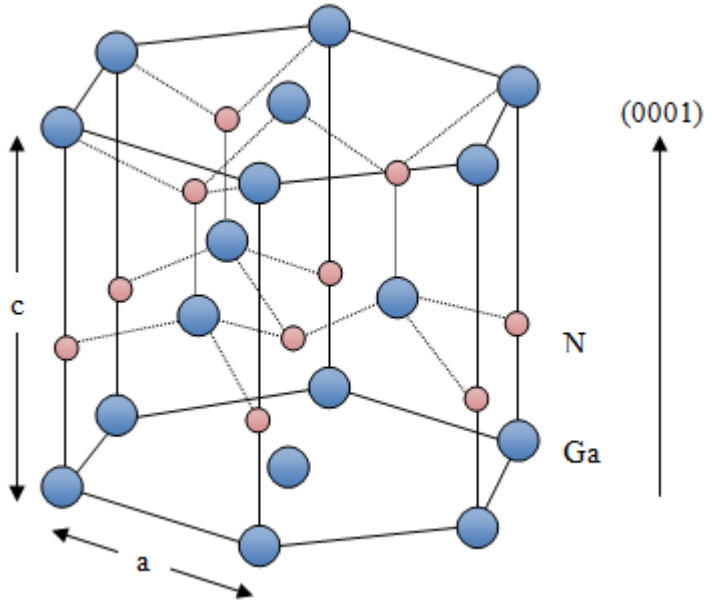

Figure 2.1 Schematic diagram of wurtzite GaN structure. The blue atoms represent the Ga atoms and the red atoms represent the N atoms.

In the crystal structure of GaN, different planes of the lattice exhibit different electrical and symmetry properties. Figure 2.2 provides the schematic diagrams for four most common planes in the GaN crystal structure and they are conventionally named as c-plane, m-plane and a-plane [2].

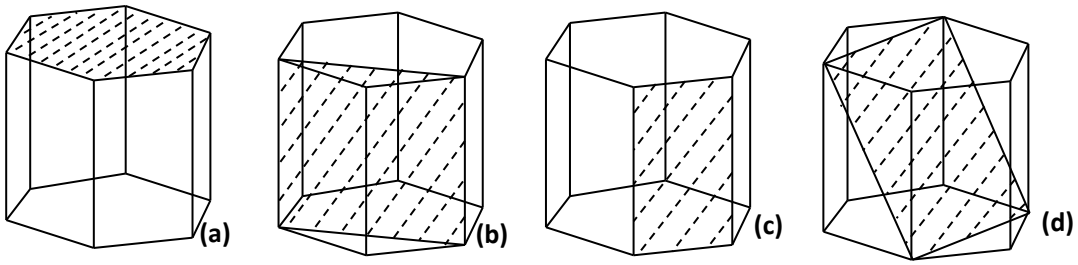

Figure 2.2 Schematic diagram of different planes in wurtzite GaN crystal lattice. (a) c-plane {0001}, (b)a-plane {11$\bar{2}$0}, (c) m-plane {1$\bar{1}$00}, and (d) semi-polar {11$\bar{2}$2} plane.

2.1.2 Electronic band structure

In the typical wurtzite GaN structure, the band structure is composed of one conduction band and three valence bands, namely, the heavy hole (*hh*) band, light hole (*lh*) band and the split-off (*so*) band. The schematic diagram of GaN band structure is provided in Figure 2.3.

The band energy E_g is normally regarded as the energy gap between the bottom of the conduction band and the top of the *hh* valance band. E_g for GaN is 3.42eV [1]. The energy gap between the *hh* band and *lh* band at $k = 0$, E_{cr}, and the energy between the *lh* band and the *so* band at $k = 0$, E_{so}, have been given in Figure 2.3.

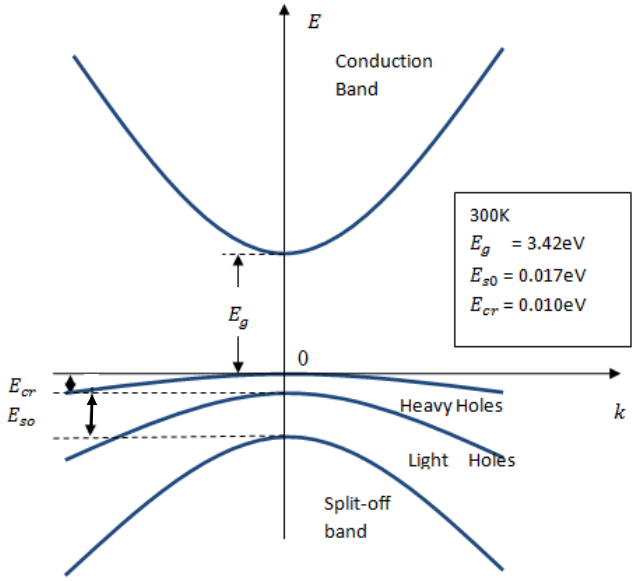

Figure 2.3 Schematic diagram of the band structure for GaN

The band energy for GaN at 3.42eV corresponds to the ultraviolet range. The

$In_xGa_{1-x}N$ (x is the In content) compound material covers a complete visible spectrum range, especially the blue and green spectrum, which enables the application of various optical devices. The band energy for Indium Nitride (InN) has been identified to be 0.77eV instead of 1.9eV, since a high crystal quality of InN was achieved by J. Wu et.al. using the molecular beam epitaxy (MBE) in 2002[3].

For many parameters of the compound materials, such as the mass, they follow the Vegard's law, i.e. the linear interpolation method. However, for the band energy of the $In_xGa_{1-x}N$ (x is the In content) compounding semiconductor, a bowing factor is highlighted, especially for InGaN with a high Indium content. The bowing factor, which is estimated to be 1.43[4], potentially lowers down the band energy from that worked out by the linear interpolation method. The band energy for $In_xGa_{1-x}N$ satisfies the following expression as a function the Indium composite *x*:

$$E_g = E_{g\_GaN} \cdot (1-x) + E_{g\_InN} \cdot x - 1.43 \cdot x \cdot (1-x) \qquad (2.1)$$

Table 2.1 lists the common parameters including the bandgap and the mass of electrons and holes for wurtzite AlN, GaN and InN, which are retrieved from literature[1, 5].

Table 2.1 Bandgap Eg, electron mass and hole mass for wurtzite nitride semiconductors (AlN, GaN and InN) at 300K

	AlN	GaN	InN
E_g(eV)	6.10	3.42	0.77
Δ_{cr} (eV)	-0.169	*0.010*	*0.040*
Δ_{so} (eV)	0.019	*0.017*	*0.005*
Electron mass (m_e^*/m_0)	m_t^*=0.32 m_l^*=0.30	m_t^*=0.20 m_l^*=0.20	m_t^*=0.07 m_l^*=0.07
Hole mass (m_h^*/m_0)	m_{hht} = 10.42 m_{hhl} = 3.53	m_{hht} = 1.60 m_{hhl} = 1.10	m_{hht} = 1.63 m_{hhl} = 1.63

The effective mass is a very important concept for the electric band structure. The effective mass of electrons and holes for AlN, GaN and InN has been summarized in Table 2.1, suggesting that for the wurtzite materials, the effective mass is anisotropic. m_t^* refers to the transverse effective mass, and m_l^* refers to the longitudinal effective mass.

Correspondingly, the energy-momentum dispersion curve for the conduction band and the valence band satisfies Eq(2.2.a) and Eq(2.2.b) respectively.

$$E_k = E_c + \frac{\hbar^2}{2m_n^*} k^2 \tag{2.2.a}$$

$$E_{k'} = E_v - \frac{\hbar^2}{2m_n^*} k'^2 \tag{2.2.b}$$

Where E_c and E_v are the conduction band energy and the valence band energy respectively. m_n^* is the effective mass for the electrons and m_h^* is for the holes[6]. The wave number k can be either 3D, 2D, 1D or 0D depending on the dimensions of the materials.

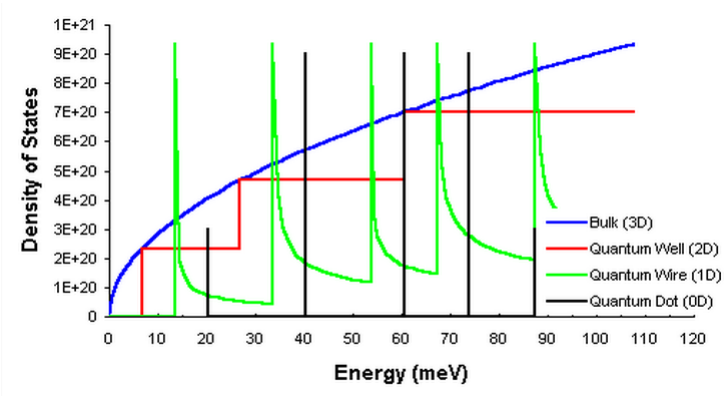

Figure 2.4 Density of states for the bulk (3D), quantum well (2D), quantum wire (1D) and quantum dot (0D) structures[7]

Low dimension structures have been widely studied in nitride materials. The density of states (DoS) for the 3D (bulk), 2D(quantum well), 1D(quantum wire) and 0D (quantum dot) structures have been illustrated in Figure 2.4. For the 2D quantum well structure, DoS is continuous but in a step-like shape, while for the 0D quantum

dot structure, DoS is in a delta function.

2.1.3 Polarization

For GaN-based materials, there exist both the spontaneous polarization and the piezoelectric polarization. Spontaneous polarization is caused by the dipole which is formed by the separation of the positive and negative charge centers. In the perfect wurtzite structure, the *c/a* ratio should be 1.633 as shown in Figure 2.1. However, in the III-nitride crystal structure, the *c/a* ratio slightly deviates from 1.633 and such a deviation is positively correlated to the spontaneous polarization[8]. For $In_xG_{1-x}N$ alloys, the compounding value for the spontaneous polarization can be calculated by the linear-interpolation method, i.e. the Vegard's law. $P_{SP}(x) = x\cdot P_{SP}^{InN} + (1-x)\cdot P_{SP}^{GaN}$, where x is the In composite for $In_xG_{1-x}N$.

Apart from the spontaneous polarization, a more prominent effect for the GaN-based semiconductor alloys is the piezoelectric polarization, as a result of lattice-mismatch induced strain between two layers. ε_1 and ε_2 represent the isotropic in-plane strain, and ε_3 is the strain along the c axis. The expressions for ε_1, ε_2 and ε_3 are given in Equation (2.3):

$$\varepsilon_1 = \varepsilon_2 = (a-a_0)/a_0 \tag{2.3.a}$$

$$\varepsilon_3 = (c-c_0)/c_0 \tag{2.3.b}$$

Where a and c are the lattice constants as illustrated in Figure 2.1. a_0 and c_0 are the lattice constants at equilibrium. The piezoelectric polarization along the c-direction can then be described as:

$$\vec{P}_{PZ}\cdot\vec{c} = (e_{33}\varepsilon_3 + e_{31}(\varepsilon_1+\varepsilon_2))\cdot\vec{c} \tag{2.4}$$

where e_{33} and e_{11} are the piezoelectric coefficients[8]. The total polarization is the sum of the spontaneous polarization and the piezoelectric polarization: $P = P_{SP} + P_{PZ}$. The value of the polarization is in a unit of C/m^2.

The piezoelectric field in the III-V nitrides of the wurtzite structure is much stronger than other III-V semiconductor materials, such as the GaAs-based materials. Since the polarization is mainly along the z-direction, among the four planes as illustrated in Figure 2.2, c-plane shows a strong polarization, a-plane and m-plane show no polarization, and the semi-polar plane $\{11\bar{2}2\}$ shows partial polarization. Currently, most of III-nitride samples are grown on the c-plane.

2.2. Nanorod structures for InGaN QWs

2.2.1 The nanorod structure

The nanorod structures of GaN/InGaN LEDs have been extensively studied.[9,10,11] Comparing with the bulk structure, the nanorod structures demonstrate many advantages. For a GaN based structure on c-plane sapphire, the built-in electric field would reduce the overlap of electric and hole wavefunctions, which leads to the quantum-confined stark effect (QCSE) and reduces the internal quantum efficiency (IQE). However, nanorod structure could partially release some strain and correspondingly reduces the QCSE[9]. Besides, light could be better collected from the active layer in the nanorod structure, and therefore the light extraction efficiency is enhanced[9].

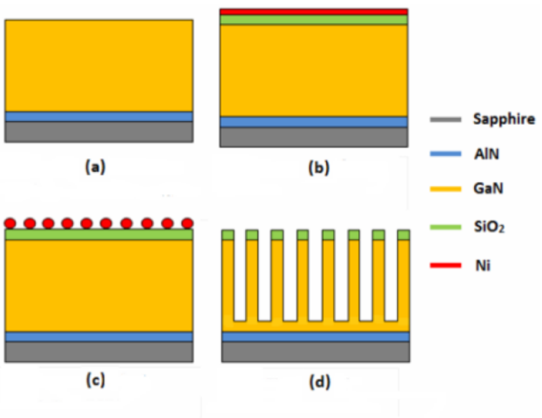

Figure 2.5 Schematic diagram of fabricating GaN nanorods

The following is the typical fabrication processes of GaN nanorods in the group of Nitrides in the University of Sheffield[12], as illustrated in Figure 2.5: An AlN buffer layer is grown between the [0001] sapphire and the GaN layer (normally contains the InGaN quantum well structure). A 200nm-thick SiO_2 film is deposited on the GaN template, and a 10nm-thick nickel film is further deposited. The sample is then annealed in the N_2 atmosphere at 850 ℃ for 60 seconds. This enables the formation of self-organized nickel islands in a diameter of around 200nm. In the process of etching the SiO_2 film by reactive ion etching (RIE), these self-organized Ni islands serve as a mask so that the SiO_2 nanorods are fabricated. The SiO_2 nanorods become a second mask for further etching the GaN layer into the GaN nanorods. This process is fulfilled using inductively coupled plasma (ICP).

2.2.2 Quantum-Confined Stark Effect (QCSE)

The Quantum-confined Stark effect (QCSE) exists in the quantum structure such as quantum wells(QW) and quantum dots(QD). It describes the influence of the external electric field on the absorption and emission spectrum of light[13,14].

The QCSE is prominent in the nitride quantum structures. A strong piezoelectric field is formed along the growth direction, because of the lattice mismatch between the InGaN QW or QD and the GaN barrier. In the presence of the electric field, the electrons and holes move towards opposite directions along the *c*-axis within the QW. The recombination between the electrons and holes becomes more difficult because the overlap between the electron and hole wavefunctions is reduced due to the QCSE. In addition, the conduction band and valence band inside the QW or QD are tilted due to the electric field, making the emission band-gap reduced and thus causing a red-shift of the emission peak wavelength. Figure 2.6 illustrates the change in band structure due to the QCSE. The QCSE can be reduced when there is abundant injection of the electron-hole pairs, leading to a screening effect. They can flatten the tilted bands and make the emission peak wavelength blue shifted.

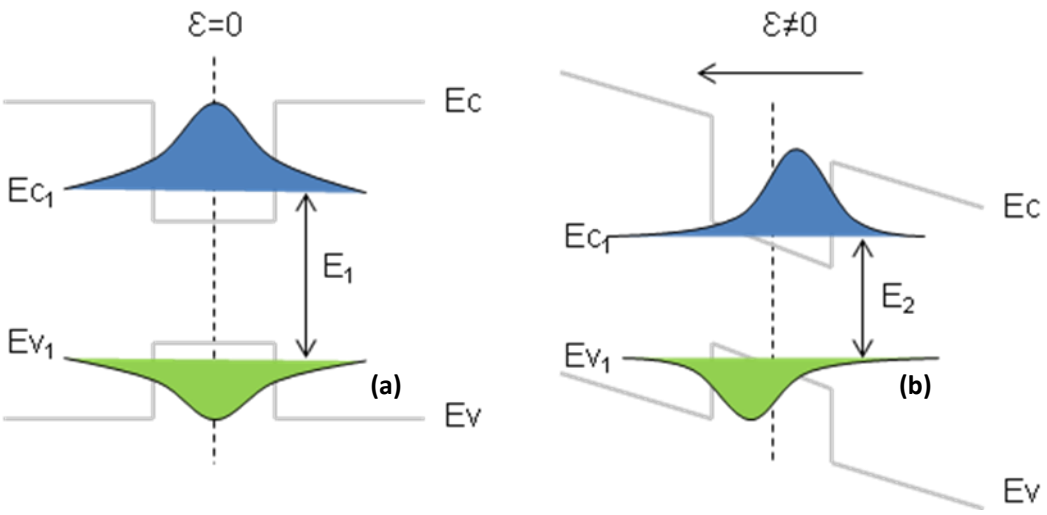

Figure 2.6 Schematic diagram of the band structure (a) without and (b) with the QCSE effect

QCSE is closely correlated with the polarization properties in nitrides materials, since the polarization field is the main cause of QCSE. The QCSE can be avoided or relieved by growing the non-polar and semi-polar films, when the polarization field is eliminated or reduced.

For LED devices, a lower degree of QCSE is desired so that the recombination of electrons and holes is largely advanced. However, QCSE is favorable in the solar cell devices[15]. The separation of the electron and hole wavefunction could prevent the recombination, thus improving the light conversion efficiency.

2.2.3 Auger recombination and the LED droop mechanism

A light emitting diode (LED) essentially consists of a *p*-*n* junction formed on a chip of semiconductor material. Under a forward bias, the electrons and holes are injected from the *n* region to the *p* region, and from the *p* into the *n* region, respectively[16]. At the active region, the electrons and holes recombine and then spontaneously emit photons.

Currently, LEDs have found wide applications such as traffic signals, visual display, etc. The technology of LEDs has been largely advanced owing to the research of GaN-based materials, the III-nitrides. The alloys of GaN (E_g = 3.42eV), InN (E_g =

0.77eV) and AlN (E_g = 6.10eV) grown by MOCVD enable the fabrication of LEDs in all visible light ranges (white, blue and green light from InGaN/GaN, and red, orange, yellow and green light from AlGaInP) [16]. Detailed growth and fabrication technologies for GaN-based LEDs differ in different groups. For instance, the GaN layer can be grown in different substrates, sapphire, SiC, silicon, etc. Normally, in order to achieve a high efficiency, the quantum structures (eg. QW and QD) are generally used as an active region.

Three important parameters for characterizing performances of LEDs are: the internal quantum efficiency (*IQE*), the light extraction efficiency (*ExE*) and the external quantum efficiency (*EQE*). They follow a relationship that: *EQE = IQE* ExE*. [17] The IQE can be estimated simply through performing the temperature dependent PL measurement[18]. The light extraction efficiency for nitride LEDs is limited because GaN has a relatively high refractive index and hence the critical angle is very small. The external quantum efficiency is the ratio of the emitted light power from the LED device and the incident power.

The mechanism of efficiency droop has been researched extensively[19,20,21,22], but is still under intensive debate. A number of models have been proposed, such as the electron overflow and defects[20].

The Auger process has been regarded as another major cause for the efficiency droop[21]. The Auger recombination process means that the emitted energy from the recombination of an electron and a hole is used to excite another electron to higher energy state instead of giving out light. The third carrier at higher energy level normally loses the excess energy via thermal vibrations. Auger recombination include two mechanisms, the direct Auger recombination and the indirect Auger recombination, as illustrated in Figure 2.7.

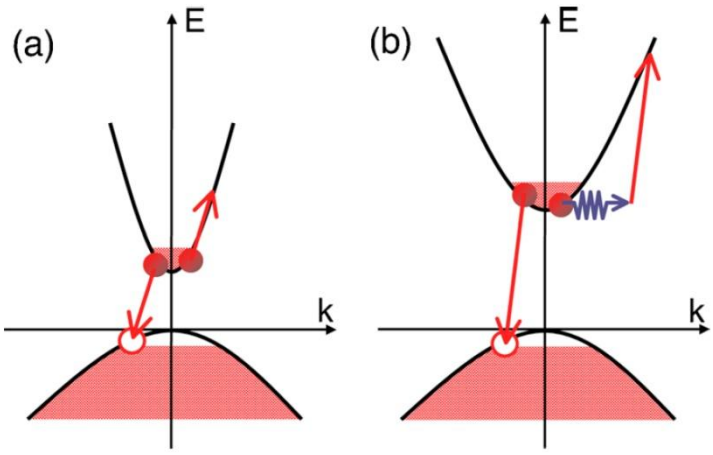

Figure 2.7 The schematic diagram of (a) direct Auger recombination and (b) indirect Auger recombination[21]

In the direct Auger recombination, the third carrier gains the energy and is directly excited to the higher energy state without a change in the momentum. For the indirect Auger recombination, the third carrier has to change its wave number by gaining additional momentum. The change of momentum is facilitated by the scattering mechanism and it enables the third carriers to be excited to a wider range of final energy states. The scattering mechanism includes the electron-phonon interaction and charged defect scattering.

In InGaN alloys, the indirect Auger recombination is found to be prominent and is regarded as an significant issue for the efficiency loss[21].

2.3. Surface plasmon coupling with InGaN QWs

2.3.1 Plasmon, surface plasmon and surface plasmon polarion

A Plasmon is a quantized plasma oscillation, similar to a phonon in a lattice vibration[23]. Plasma is the fourth fundamental state of matter after solid, liquid and gas. Plasma contains a high density of charged particles, i.e. the positive ions and negative ions or electrons. In the metal, plasma oscillation can be observed because the metal contains a large amount of free electrons and they oscillate around the

fixed positive ions.

The free electron in the metal oscillates at a typical frequency, the plasma frequency, which depends on the density of electrons. When incident light with a frequency smaller than the plasma frequency of the metal radiates onto the metal surface, light is reflected by the metal. Only the light with a higher frequency than the plasma frequency will be transmitted through the metal, while the electric field of light with a lower frequency than the plasma frequency will be screened by the electrons in the metal[24]. For most metals, their plasma frequency, ω_p, is in the range of ultraviolet (PHz). The metals reflect almost all visible light and that's why they look shiny under the sun.

A surface plasmon[25] is a special kind of plasmon that is only confined at the surface: $E=E_0 \exp[i(k_x x + k_z z - \omega t)]$. As illustrated in Figure 2.8.a, at the boundary, the wave number has to satisfy: $k_{z1}/\varepsilon_1 + k_{z2}/\varepsilon_2 = 0$ .Where ε_1 is the permittivity of the metal, and ε_2 is the permittivity of the dielectric. k_{z1} and k_{z2} are the wave-number components along z direction for the metal and the dielectric respectively[26]. In the meantime, from the definition, the wave number has to satisfy: $k_x^2+k_{z1}^2 = \varepsilon_1 (\omega/c)^2$ and $k_x^2+k_{z2}^2 = \varepsilon_2 (\omega/c)^2$. Therefore, k_x becomes: $k_x = \frac{\omega}{c}(\frac{\varepsilon_1\varepsilon_2}{\varepsilon_1+\varepsilon_2})^{1/2}$, considering the free electron model, $\varepsilon(\omega)=1-\omega_p^2/\omega^2$. When k_x increases towards infinity, ω approaches a limit value:

$$\omega = \frac{\omega_p}{\sqrt{1+\varepsilon_2}} = \omega_{SP} \qquad (2.5)$$

The limit value of ω is the surface plasmon frequency ω_{sp}[27], and $\omega_{sp} = \omega_p/\sqrt{2}$ when $\varepsilon_2 = 1$. i.e. when the dielectric is the air. These features are illustrated in the dispersion curve in Figure 2.8.b with k_x as a function of ω. $\hbar\omega_{sp}$ is the surface plasmon energy E_{sp}.

k_x

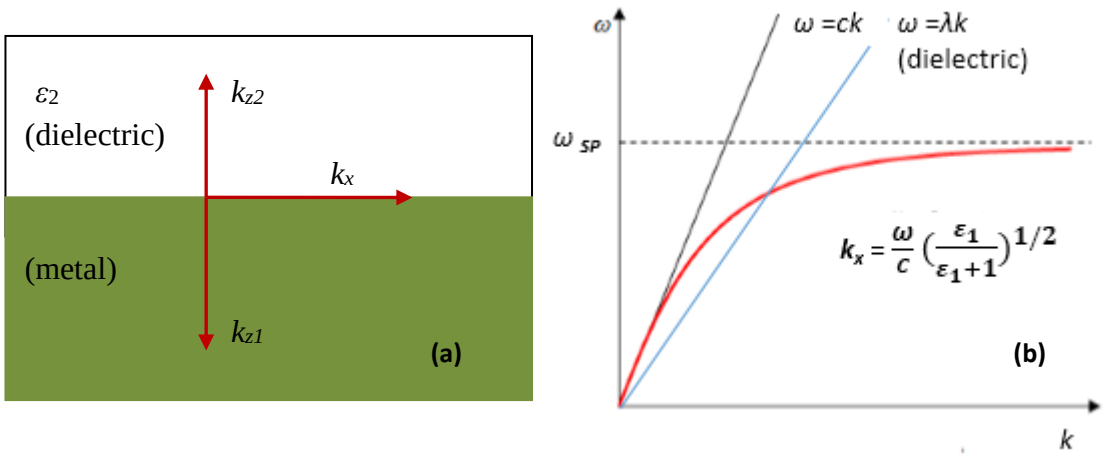

Figure 2.8 (a) Schematic diagram of the interface of metal and dielectric. (b)The dispersion curve for surface plasmon

For different metals, the surface plasmon energy varies: 2.77eV (448nm) for Ag, 2.33eV (435nm) for Au, 2.50eV (496nm) for Ni, 2.85eV (435nm) for Pt and 3.44eV (360nm) for Al[28]. The values in the brackets suggest the corresponding wavelength for the resonance energy. For these metals, the resonance energy falls into the visible region. At the surface plasmon energy, dk/dω is at a maximum value that suggests an extremely high density of states (DOS).

Surface plasmon polariton is the coupling between a photon and the surface plasmon[29]. Normally the dispersion line of light mode is tangent to the dispersion curve of surface plasmon mode at the origin, as illustrated in Figure 2.8.b. Since the momentum p satisfies: $p = \hbar k$, the wave-number k indicates the strength of momentum. The surface plasmon mode always has a higher momentum than the light mode, and thus is not able to couple to the light mode. .

In order to make the surface plasmon polariton (SPP) possible, the momentum for light mode has to be changed by increasing the wave-number k . A viable way is to pass light into a block of glass (dielectric constant larger than one) before it reaches the metal. In this circumstance, the dispersion line inside the dielectric could intersect with the SPP dispersion curve, i.e. the light mode could couple to the SPP mode.

The surface plasmon can also be converted back to light mode through different approaches. When the surface plasmon wave propagates in the rough space, it reduces the momentum to match that for the light mode and hence becomes radiative. This is a very critical process in the surface plasmon opto-electronic devices since the light emission and extraction is the main concern for these devices. The metal in a grating format could promote the coupling of surface plasmon to a light mode..

2.3.2 Exciton localization and delocalization in InGaN QWs

Exciton localization refers to the phenomenon that electrons or holes are confined in the local potential minima of the InGaN band energy surface. This can be caused by In clustering in InGaN material. Exciton localization cannot be observed directly or visualized, but it can always be reflected in the photoluminescence spectra. For exciton recombination in localized potential surfaces, the emitted photon has a lower energy which causes a red shift of the PL emission energy[30].

The localized excitons can be delocalized, i.e. to get out of the confinement of the localized potential surfaces, as temperature increases to a certain level. Normally, in the temperature dependent PL measurement of InGaN wafers, the S-curve of the emission energy can always be observed [31]. In the temperature range of 100K -200K, the PL emission peak energy blue-shifts which goes against the trend of thermal expansion. Such blue-shifts are caused by the exciton delocalization as temperature rises. As temperature goes up further, the delocalization process is weaker compared with the effect due to thermal expansion. Therefore, the overall effect of the PL emission energy is red shifted. Consequently, the degree of the blue shift of the PL emission energy at the intermediate temperature range is a parameter for the scale of exciton delocalization [30].

For localized excitons, their wavefunction in the k space is more wide spread and this facilitates the recombination of excitons. The internal quantum efficiency has been found to be higher for QWs with strong localization [32]. The delocalization

leads to band gap renormalization and contributes to the efficiency droop [19]. However, exciton delocalization has been found to promote the surface plasmon-exciton coupling and thus enhancing the IQE for Ag-coated QW samples in this study.

2.4. InGaN-based ring cavities

2.4.1 Optical cavity

Cavity is a critical part of a laser, which is the acronym for Light Amplification by Stimulated Emission of Radiation. A stimulated emission is the main mechanism for lasers[33],

Cavity is the premise for stimulated emission, because in the gain media of the cavity, the population inversion can be realized when the number of electrons in the excited states outweighs the number of electrons in the lower states. The power of circulating light confined in the cavity can be amplified and eventually compensate the optical loss.

Lasers are classified into many categories, including the semiconductor laser diode (LD), gas lasers and conventional solid state lasers. Semiconductor LD has many advantages compared with other lasers. First of all, the semiconductor LD is compact, robust and thin. Besides, it works at a relatively low power level, being pumped by the electric current directly. These features lead to a high power-conversion efficiency comparing with other lasers [16]. The laser diode in the visible spectrum range (visible LDs) will be an emerging market in the near future with wide applications in entertainment and data application. The GaN-based semiconductors with a direct wide-bandgap is regarded as an ideal material for making visible LDs.

Whisper gallery mode (WGM) cavities have been suggested for nitride-based

micro/nano rings and disks. High quality factors have been reported for such WGM cavities[34].

2.4.2 Whispering gallery mode

Whispering gallery mode (WGM) is a widely used resonating mechanism in the cylindrical structure resonator, i.e. the disk cavity and ring cavity. The name of whispering gallery derives from the phenomenon first discovered in St Paul's Cathedral in London by Lord Rayleigh[35] . Along circumference of the circular wall, the sound wave known as whisper-gallery wave propagates, and the sound can only be heard in some points while in other points the sound is diminished. The formation of the WGM is illustrated in Figure 2.9 (Note that wave propagation can be both clockwise and anticlockwise, and Figure 2.9 only shows the first scenario). The circumference equals to the product of the wavelength and an integer in order to form the resonance. After the discovery of whisper gallery modes in sound waves, the WGM has been found in a wider application of optical resonators. The cylindrical and spherical structures with a relatively high dielectric constant can well confine the light and the resonant eigenvalues (frequencies) of the dielectric spheres was calculated[36,37].

In WGM cavities, circulating light propagates around the periphery as a result of total interaction reflection since the material for resonators normally has a higher dielectric constant than the surrounding medium, which is usually the air. The dielectric constant, or the permittivity of a material, *epsilon,* is a critical factor for the properties of WGM[38]. In practical work for optics, the refractive index is more frequently used. The relationship between refractive index *n* and the dielectric constant follows: $n = \sqrt{\varepsilon_r \mu_r}$, where ε_r is the relative permittivity of the dielectric material and μ_r is the relative permeability. For the dielectric material, μ_r is normally close to 1 and hence $n_0 \approx \sqrt{\varepsilon_r}$.

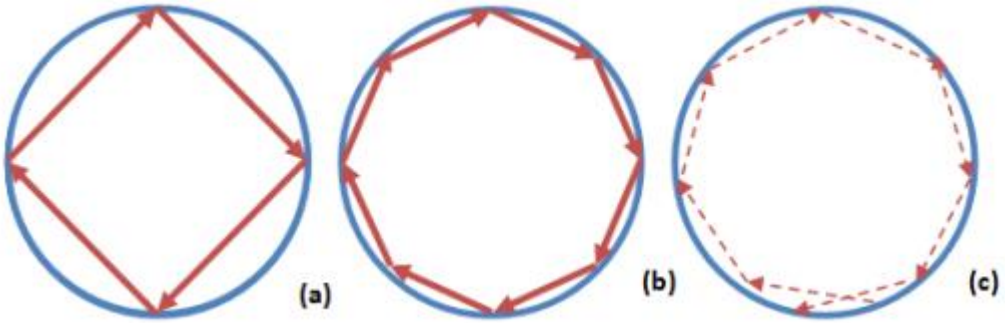

Figure 2.9 Schematic diagram of whispering gallery mode with (a) low mode number (b) large mode number, and (c) off-resonance of whispering gallery mode

The refractive index, *n*, can be regarded as the ratio of light speed inside the dielectric material v_R to that in the vacumm air *c*. There is the relationship between the wavelength in dielectric medium λ_R and the wavelength in vacuum air: $\lambda_R = \lambda_0 V_R/c = \lambda_0/n$. For a given cylindrical cavity, the total circumference path, roughly equals to the product of the wavelength in the medium and an integral, which is the mode number *m*.

$$2\pi nR \approx m\lambda_R \tag{2.6}$$

The calculated radius *R* is called the mode radius, which is normally 80%-90% of the physical radius of the resonator. The mode spacing between the mode *m* and *m+1*, the one higher to *m*, can be expressed as $\lambda^2/2\pi nR$[39].

The WGM in optical cavities is essentially an interaction between the medium and the time-varying electromagnetic field. The Maxwell's equations (2.7.a,b,c&d) free of source and charge can be applied to the dielectric resonators.

$$\nabla \times H = \varepsilon \frac{\partial E}{\partial t} \tag{2.7.a}$$

$$\nabla \times E = -\mu \frac{\partial H}{\partial t} \tag{2.7.b}$$

$$\nabla \cdot H = 0 \tag{2.7.c}$$

$$\nabla \cdot \varepsilon E = 0 \tag{2.7.d}$$

Where ε and μ denote the permittivity and permeability respectively. μ is very close to the permeability of vacuum. Normally the Helmholtz equation is used to describe the electromagnetic field in the whispering gallery mode.

$$[\nabla^2+\omega^2\mu\varepsilon]\, E = 0 \qquad (2.8)$$

Where ω is the angular frequency. Due to the circular symmetry, sometimes the cylindrical coordinate (r, φ) is adopted and the electric field becomes: $E(r, \varphi, t) = E(r)\, e^{i(m\varphi-\omega t)}$. Substituting this into Equation(2.8) gives the Bessel function and can be solved analytically[40]. In this thesis, the finite-difference time-domain (FDTD) method is adopted, which is a numerical approach.

2.4.3 Quality factor

The quality factor is one of the most important indices to describe the resonator's performance. The quality factor (Q-factor) is the ratio of the total power to the loss of power in the cavity. A higher Q-factor indicates that the resonator is more efficient in confining the light which is desired for the optical resonator.

One universal relationship for the Q-factor is: $Q \equiv \omega \frac{U}{P}$. Where U is the total energy the electromagnetic field in the cavity, ω is the angular frequency and it follows: $\omega=2\pi c/\lambda$. λ is the wavelength in vaccum air. $U = \int \frac{1}{2}(\varepsilon E^2 + \mu H^2) dV$. P is the power loss, and it can be calculated by measuring the total flux outflows in all directions[41]. Besides, quality factor can be an indicator of the time for natural energy decay inside the resonator. A longer decay time is expected for the resonator with a higher Q-factor. A third method to measure the Q-factor, which is a practical way in experiments, is related to the linewidth (FWHM) of the resonance peak: $Q = \omega\tau = \omega/\Delta\omega_{FWHM}$.

Since the Q-factor is essentially an gauge of the energy loss, a fourth method of obtaining Q-factors derives from the expression for complex propagation constant: k

$= \omega/c = \beta + i\alpha/2$. Where k is the complex wave number, the real part $\beta = 2\pi/\lambda_o \in \mathbf{R}$ is the phase constant with λ_o being the wavelength in vacuum air. The imaginary part represents the loss mechanism and $\alpha \in \mathbf{R}$ is named as intensity attenuation coefficient. The expression for Q-factors becomes:

$$Q = \frac{\beta}{|\alpha|} = \frac{\mathrm{Re}(\omega)}{2|\mathrm{Im}(\omega)|} \tag{2.9}$$

Since the nature of quality factor is always the same from different interpretations, there should be a consistent result of the quality factor from these various methods within certain error allowance[42].

2.5. InGaN-based solar cells

2.5.1 Principles of solar cells

The solar cell is another important application of optoelectronics [16]. While LEDs convert the electricity to light, the solar cell operates in the opposite way, by converting the light to electricity directly in the photovoltaic (PV) effect. The solar energy is a main source of the renewable energy.

The photovoltaic (PV) process has three critical components. First of all, the absorption of light (photons) generates the electron-hole pairs inside the solar cells. Secondly, the electrons and holes are separated to avoid the recombination which would otherwise lower down the light conversion efficiency. Thirdly, the separated charged carriers are extracted to the external circuits and to be utilized.

Since a solar cell is essentially a p-n junction working at a reversed voltage, the Shockley's current-voltage equations are applied to the solar cells[43]. A schematic diagram of the solar cell I-V properties is provided in Figure 2.11.

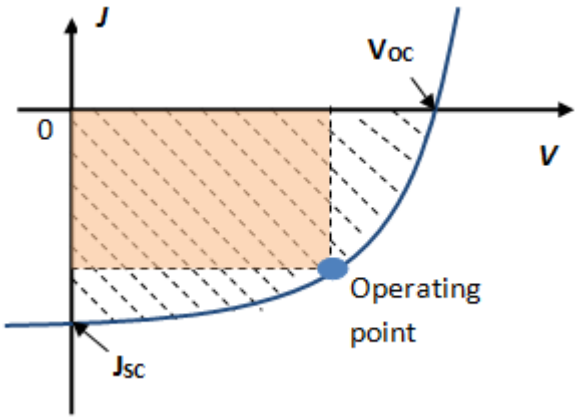

Figure 2.11 Schematic diagram of the current-voltage properties of solar cells.

The current-voltage equation for a solar cell is given in Equation (2.10)[43]:

$$J = J_{sc} - J_0(e^{V/K_BT} - 1) \tag{2.10}$$

When $J = 0$, the open circuit voltage V_{oc} can be obtained:

$$V_{OC} = k_B T \ln(J_{SC} / J_0 + 1) \tag{2.11}$$

The photon generated current density J_{sc} and the open circuit voltage V_{oc} are marked in Figure 2.11. J_0, the reverse saturation current density in solar cell current-voltage functions can be expressed by Equation (2.12):

$$J_0 = qN_C N_V (\frac{D_n}{N_A L_n} + \frac{D_p}{N_D L_p}) \exp(-\frac{E_g}{K_B T}) \tag{2.12}$$

Where N_c and N_v are the effective density of states in conduction band and valence band, respectively; N_A and N_D are the doping level for p-layer and n-layer, respectively; D_n and D_p are the diffusion coefficients of electrons and holes, respectively; and L_n and L_p are the diffusion length of electrons and holes, respectively.

The solar cell conversion efficiency is a main issue for solar cells, and it follows: $\eta = \frac{FFV_{oc}J_{sc}}{p_i}$, where P_i is the input power, and J_{sc}, V_{oc} and FF are the short-circuit current density, open-circuit voltage and filling factor respectively.

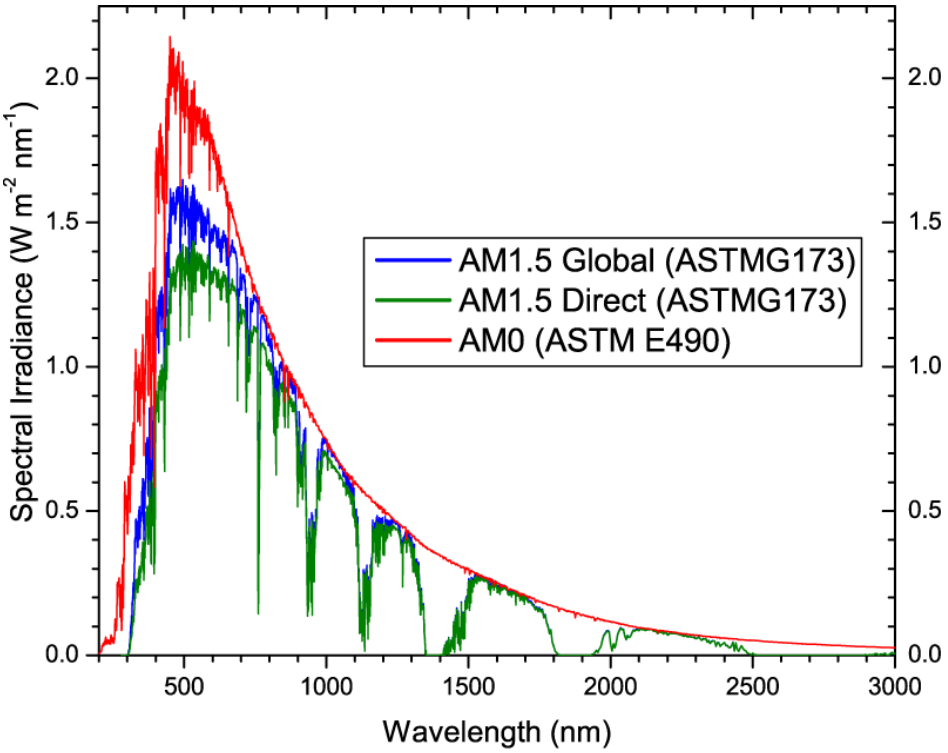

Figure 2.12 Standard solar spectrum[44]

The short circuit current density J_{sc} , also known as the photon generated current density, is the primary concern for solar cells. The solar power density varies for light of different wavelengths. The standard solar spectrum is given in Figure 2.12[44]. The AM 1.5 spectrum refers to the solar cell spectrum at the earth. Several clear troughs can be observed in the AM1.5 spectrum since the atmosphere of the earth (such as CO_2, gas H_2O, O_3, etc) absorbs some light power. Sometimes the Blackbody equation is adopted to model the solar spectrum analytically[45] and the spectrum it renders is consistent with the AM1.5 spectrum. The peak of the solar spectrum appears at around 1.1eV in the infrared spectrum. Therefore, in order to enhance the light conversion efficiency and the photon generated current density J_{sc}, the solar cell should cover a wide span of spectrum, especially the infrared range. This raises certain requirements on the band structure of the absorption materials.

As for the open circuit voltage V_{oc}, it equals to the separation of the quasi Fermi levels of the conduction band and the valence band, and is related to the incident

light power density. The third important parameter that affects the solar cell conversion efficiency is the filling factor. At the operating point, the output power is maximized comparing with any other points in the I-V curve. In Figure 2.11, an area formed by the I-V curve and the coordinates is highlighted in shadow, and a rectangle is highlighted in orange. The ratio of the rectangular area to the shadow area is called the filling factor. Generally the commercial solar cells should have a filling factor higher than 0.7. By improving any of the three parameters, J_{sc}, V_{oc} and FF , the solar cell conversion efficiency can be enhanced.

2.5.2 Advantages and challenges for InGaN-based solar cells

III-nitride semiconductors have direct bandgaps and their bandgaps cover the complete visible spectrum and a major part of the ultraviolet, which exactly corresponds to the solar spectrum. Therefore, the InGaN alloys are most promising materials that can be potentially fabricated into solar cells with an ultra-high efficiency [16].

So far, the research on III-nitride solar cells is in its infancy. There exist a number of fundamental challenges in both technology and structural design. One of the intrinsic challenges is that the well-known multiple-junction structure which has been successfully employed for the fabrication of conventional solar cells cannot be applied for the fabrication of III-nitride based solar cells due to a fundamental issue on *p*-GaN[46,47]. It is well-known that *p*-GaN needs to be exposed to nitrogen ambient at a high temperature in order to be activated. Furthermore, any activated *p*-GaN can return to its originally passivated state if it is exposed to an hydrogen-contained ambient (such as NH_3) at a high temperature for the growth of any further structure. Therefore, *p*-GaN needs to be the final layer of solar cells in order to both facilitate the *p*-GaN activation and avoid being deactivated. This causes a dilemma for the InGaN multiple-junction solar cells. Therefore, innovation on other structures for nitride-based solar cells is highly suggested for a high solar cell conversion

efficiency in practice.

2.5.3 Basic mechanism of intermediate-band solar cells (IBSC)

Theoretically, the concept of intermediate-band solar cells (IBSCs) provides an alternative option for high efficiency solar cells based on a single junction. Luque and Mart í[48]predicted a thermodynamic upper limit efficiency of up to 63.1% for an IBSC with a single intermediate band (IB) under full concentration, i.e., 46000 suns. IBSCs provide an effective approach to high solar cell conversion efficiency. .

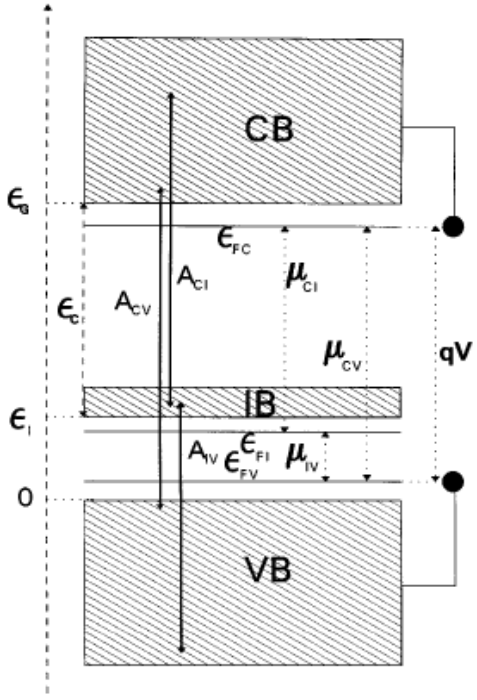

Figure 2.13 Schematic diagram of the structure of IBSC with single intermediate band[48]

The basic structure of IBSC [48] is provided in Figure 2.13. The eigenstate of the conduction band of the quantum dot is regarded as the intermediate band (IB), and VB and CB refer to the valence band and the conduction band of the barrier. Two levels of photon absorption can be realized under this mechanism. The IB can be formed by various ways such as the quantum dot systems[49]and doping of transition metals[50],etc

Several assumptions have been raised for the IBSC structure: Firstly, even though

the IB causes an extra absorption of photons (A_{IV} as illustrated in Figure 2.13), no carriers are extracted from the IB, and the excited electrons on the IB will further be excited to the CB. Electrons and holes can only been extracted from CB and VB respectively, and nonradiative recombination is not considered. Secondly, there must be a quasi Fermi level for each band (CB, IB or VB). Thirdly, the open circuit voltage V_{oc} is not affected by the introduction of IB and is maintained as the separation between the Fermi levels for CB and VB.

Multiple IB solar cells using this IBSC model have been studied in many later research, and their efficiency could not exceed 63% for the single IB solar cell. This is believed to be caused by the arbitrary arrangement of the energy level of IB and the matrix bandgap. It's pointed out that[45], a maximum efficiency of 74.6% (under full concentration) could be reached if the matrix bandgap and energy levels of four IBs are optimized. The maximum efficiency with three IBs reaches 73.1% (under full concentration) when the matrix bandgap and three IB energy levels are set to be 2.25eV, 1.73eV, 1.44eV and 1.23eV respectively[45] .

2.5.4 Rationale for Quantum Dot IBSC

The phonon bottleneck effect is a special feature for quantum dots. When electrons are injected to higher states in the quantum structure, they have to rely on phonon scattering to relax to lower states of the quantum structure. Phonon scatting has to follow both the energy conservation and the momentum conservation. In the quantum well (QW) structure, these can be easily satisfied because the momentum, or the transverse wave number, for the dispersion curve of the QW[51] is continuous. However, for the QD system, the wave number on the dispersion curve is not continuous. The energy separation between electron inter subbands may not match the energy of an optical phonon, e.g. the LO phonon energy of GaN as 91meV. In this scenario, electron relaxation via phonon emission is greatly suppressed. Therefore, there lacks effective channels for the carrier relaxation in the QD system,

causing the so-called phonon bottleneck effect [52,53,54].

For IBSC, there are premises that each IB has to be supported by a quasi Fermi level [51] and the photon generated current density is collected at the open-circuit voltage of the barrier. In the QW system, due to the continuous transversal wave number and easy electron relaxation via phonon scattering, the separation of three quasi-Fermi levels can hardly be sustained[55]. However, for the QD system, the “phonon bottleneck" effect avoids electron relaxation and helps to maintain the three quasi-Fermi levels. Although the phonon bottleneck effect is a problem for QD lasers because it causes difficulties in carrier relaxation, it is a favorable property for the QD IBSCs [49]. The phonon bottleneck effect is the fundamental rationale for the feasibilities of QD IBSCs.

Reference

[1] Vurgaftman, I., & Meyer, J. R. (2003). Band parameters for nitrogen-containing semiconductors. *J. Appl. Phys*., 94(6): 3675-3696

[2] Zhu, T., & Oliver, R. A. (2012). Unintentional doping in GaN. *Phys. Chem. Chem. Phys.*14(27): 9558-9573

[3] Wu, J., Walukiewicz, W., Yu, K. M., Shan, et al. (2003). Superior radiation resistance of InGaN alloys: Full-solar-spectrum photovoltaic material system. *J. Appl. Phys.*, 94: 6477-6480

[4] Wu, J., Walukiewicz, W., Yu, K. M., et al.(2002). Small band gap bowing in InGaN alloys. *Appl. Phys. Lett*., 80:4741-4744

[5] NSM. Archive. (2013).Semiconductor parameters (InN, GaN and AlN). Retrieved from http://www.ioffe.rssi.ru/SVA/NSM/Semicond/

[6] Suzuki, M, T. Uenoyama, A. Yanase, (1995). First-principles calculations of

effective-mass parameters of AlN and GaN. *Phys. Rev. B.*, 52(11): 8132-8139

[7] Zeghbroeck, B.V. (2006) . Principles of Semiconductor Devices, Colarado University

[8] Bernardini, F., Fiorentini, V., & Vanderbilt, D. (1997). Spontaneous polarization and piezoelectric constants of III-V nitrides. *Phys. Rev. B.*, 56(16): R10024 -R10031

[9] Renwick, P., Tang, H., Bai, J., & Wang, T. (2012). Reduced longitudinal optical phonon-exciton interaction in InGaN/GaN nanorod structures. *Appl. Phys. Lett.*, 100(18):182105-182107

[10] Park, Y. S., Holmes, M. J., Shon, Y., Yoon, I. T., Im, H., & Taylor, R. A. (2011). GaN nanorods grown on Si (111) substrates and exciton localization. *Nano. Res. Lett.* 6(1): 81-94

[11] Kawakami, Y., Kaneta, A., Su, L., Zhu, Y., Okamoto, K., Funato, M., ... & Kishino, K. (2010). Optical properties of InGaN/GaN nanopillars fabricated by postgrowth chemically assisted ion beam etching. J. Appl. Phys.,107(2): 023522-023527

[12] Xing, K., Gong, Y., Bai, J., & Wang, T. (2011). InGaN/GaN quantum well structures with greatly enhanced performance on a-plane GaN grown using self-organized nano-masks. *Appl. Phys. Lett.*, 99(18):181907-181909

[13] Friedrich,H. (1990). *Theoretical Atomic Physics.* Berlin: Springer-Verlag. pp,85

[14] Miller, D. (1984). Band-Edge Electroabsorption in Quantum Well Structures: The Quantum-Confined Stark Effect. *Phys. Rev. Lett.* 53: 2173–2176

[15] Toledo, N. G., & Mishra, U. K. (2012). InGaN solar cell requirements for high-efficiency integrated III-nitride/non-III-nitride tandem photovoltaic devices. *J. Appl. Phys.*, 111(11):114505-114509

[16] Li, S. S. (2006). *Semiconductor physical electronics, 2nd ed*. Berlin: Springer. pp, 488, 357,521-523

[17] Dai, Q., Shan, Q., Wang, J., Chhajed, S., et al. (2010). Carrier recombination mechanisms and efficiency droop in GaInN/GaN light-emitting diodes. *Appl. Phys. Lett.*, 97(13): 133507-133507

[18] Okamoto, K., Niki, I., Scherer, A., Narukawa, Y., Mukai, T., & Kawakami, Y. (2005). Surface plasmon enhanced spontaneous emission rate of InGaN/GaN quantum wells probed by time-resolved photoluminescence spectroscopy. *Appl. Phys. Lett.*, 87(07): 071102-071104

[19] Xu, J., Schubert, M. F., Noemaun, A. N., Zhu, et al (2009). Reduction in efficiency droop, forward voltage, ideality factor, and wavelength shift in polarization-matched GaInN/GaInN multi-quantum-well light-emitting diodes. *Appl. Phys. Lett.*, 94(1): 011113-011115

[20] Piprek, J. (2010). Efficiency droop in nitride based light emitting diodes. *Phys. Status Solidi A*, 207(10): 2217-2225

[21] Kioupakis, E., Rinke, P., Delaney, K. T., & Van de Walle, C. G. (2011). Indirect Auger recombination as a cause of efficiency droop in nitride light-emitting diodes. *Appl. Phys. Lett.*, 98(16):161107-161109

[22] Renwick, P., Tang. H, & Wang. T. (2011). Evaluating Internal Quantum Efficiency of Green LEDs via Electroluminescence. UK *Nitrides Consortium (UKNC) 2011 winter conference, Manchester UK*

[23] Bittencourt, J. A. (2004). Fundamentals of Plasma Physics. New York: Springer. pp,132

[24] Böer, K. W. (2002). *Survey of Semiconductor Physics 1,2nd ed.*. New Jersey:

John Wiley & Sons. pp, 525

[25] Ritchie, R. H. (June 1957). Plasma Losses by Fast Electrons in Thin Films. *Phys. Rev.*,106 (5): 874–881

[26] Heinz, R. (1988). *Surface Plasmons on Smooth and Rough Surfaces and on Gratings.* Springer Tracts in Modern Physics. New York: Springer-Verlag, pp,111

[27] Michael, C. G. (1989). *Introduction to Surface and Superlattice Excitations.* New York: Cambridge University Press, pp,85

[28] Crawford, M. H., Fischer, A. J., Koleske, D. D., et al. (2009) *Final LDRD Report: Nanoengineering for Solid-State Lighting*. Sandia National Laboratory

[29] Barnes, W. L., Dereux, A., & Ebbesen, T. W. (2003). Surface plasmon subwavelength optics. *Nature*, 424(6950): 824-830

[30] Eliseev, P. G., Perlin, P., Lee, J., & Osinski, M. (1997). "Blue" temperature-induced shift and band-tail emission in InGaN-based light sources. *Appl. Phys. Lett.*, 71(5): 569-571

[31] Lee, K. B., Parbrook, P. J., Wang, T., Ranalli, F., Martin, T., Balmer, R. S., & Wallis, D. J. (2007). Optical investigation of exciton localization in font face $Al_xGa_{1-x}N$. *J. Appl. Phys.* 101(5): 053513-053517

[32] Chichibu, S. F., Azuhata, T., Sugiyama, M., et al.(2001). Optical and structural studies in InGaN quantum well structure laser diodes. *J Vac Sci Technol B Microelectron Nanometer Struct Process Meas Phenom* , 19(6):2177-2183

[33] Gould, R. Gordon (1959). The LASER, Light Amplification by Stimulated Emission of Radiation . In Franken, P.A. and Sands, R.H. (Eds.). *The Ann Arbor Conference on Optical Pumping, the University of Michigan, 15 June through 18 June 1959*. pp. 128

[34] Li, K. H., Ma, Z., & Choi, H. W. (2011). High-Q whispering-gallery mode lasing from nanosphere-patterned GaN nanoring arrays. *Appl. Phys. Lett.*, 98(7): 071106-071108

[35] Rayleigh, L. (1910). CXII. The problem of the whispering gallery. *The London, Edinburgh, and Dublin Philosophical Magazine and Journal of Science*, 20(120): 1001-1004

[36] Mie, G. (1908). On optical characteristics of turbid media, with special reference to colloid metallic solutions. *Annals Phys.*, 25: 377-445

[37] Debye, P. (1909). Der lichtdruck auf kugeln von beliebigem material. *Annalen der physik*, 335(11): 57-136

[38] Urzhumov, Yaroslav A. (2005). Electric and magnetic properties of sub-wavelength plasmonic crystals. *J. Opt. A: Pure Appl.Opt.*,7 (2): S23-S28

[39] Gamba, J. M. (2012). *The role of transport phenomena in whispering gallery mode optical biosensor performance* . Doctoral dissertation, California Institute of Technology.

[40] Franchimon, E. (2010). Modelling circular optical microresonators using whispering gallery modes. Master thesis, University of Twente

[41] Englund, D., Fushman, I., & Vuckovic, J. (2005). General recipe for designing photonic crystal cavities. *Opt. Expr.*, 13(16): 5961-5975

[42]Gomilšek,M. (2011) Whisper gallery mode seminar report. Retrieved from: http://mafija.fmf.uni-lj.si/seminar/files/2011_2012/wgm.pdf

[43] Wen, B, Zhou, J.J, Jiang, R. L, & Zheng. Y.D. (2007). Theoretical calculation of conversion efficiency of InGaN solar cells. *Chin. J. Semicond.*, 28: 1392-1936

[44] AM 1.5 Solar spectrum. Retrieved from: http://rredc.nrel.gov/solar/spectra/am1.5/

[45] Nozawa, T., & Arakawa, Y. (2011). Detailed balance limit of the efficiency of multilevel intermediate band solar cells. *Appl. Phys. Lett*., 98(17):171108-171111.

[46] Dahal, R., Li, J., Aryal, K., Lin, J. Y., and Jiang, H. X. (2010). InGaN/GaN multiple quantum well concentrator solar cells. *Appl. Phys. Lett.*, 97(7): 073115 -073118

[47] Yamamoto, A., Islam, M. R., Kang, T. T., & Hashimoto, A. (2010). Recent advances in InN-based solar cells: status and challenges in InGaN and InAlN solar cells. *Phys. Status Solidi C*, 7(5): 1309-1316

[48] Luque, A., & Martí, A. (1997). Increasing the efficiency of ideal solar cells by photon induced transitions at intermediate levels. *Phys. Rev. Lett.*, 78(26): 5014-5016

[49] Martí, A., López, N., Antolin, E., Canovas, E., Stanley, C., Farmer, C., & Luque, A. (2006). Novel semiconductor solar cell structures: The quantum dot intermediate band solar cell. *Thin Solid Films*, 511:638-644

[50] Martí, A., Tablero, C., Antolín, E., Luque, A., Campion, R. P., Novikov, S. V., & Foxon, C. T. (2009). Potential of Mn doped $In_{1-x}Ga_xN$ for implementing intermediate band solar cells. *Solar Energy Mater. Solar Cells*, 93(5): 641-644

[51] Bremner, S. P., Corkish, R., & Honsberg, C. B. (1999). Detailed balance efficiency limits with quasi-Fermi level variations. *Electron Devices, IEEE Transactions on*, 46(10):1932-1939

[52] Heitz, R., Born, H., Guffarth, F., Stier, O., Schliwa, A., Hoffmann, A., & Bimberg, D. (2001). Existence of a phonon bottleneck for excitons in quantum

dots. *Phys. Rev. B*, 64(24):241305-241308

[53] Cuadra, L., Martí, A., López, N., & Luque, A. (2004, September). Phonon bottleneck effect and photon absorption in self-ordered quantum dot intermédiate band solar cells. *Proc. of the 19th European Photovoltaic Solar Energy Conference* , 250-254

[54] Li, X. Q., Nakayama, H., & Arakawa, Y. (1999). Phonon bottleneck in quantum dots: Role of lifetime of the confined optical phonons. *Phys. Rev. B*, 59(7): 5069-5072

[55] Luque, A., Martí, A., & Cuadra, L. (2001). Thermodynamic consistency of sub-bandgap absorbing solar cell proposals. *Electron Devices, IEEE Transactions on*, 48(9): 2118-2124

3. Study of optical properties for GaN/ InGaN nanorod structures

This chapter studies the experimental work on GaN/InGaN nanorod structures by means of temperature dependent photoluminescence measurements. The main contribution is to find out that the electron- longitudinal optical (LO) phonon coupling effect is prominently reduced in the nanorod structures comparing to the as-grown structures. Energy dissipation via phonon scattering has been regarded as an important step in the indirect Auger recombination process that contributes to the LED efficiency droop. It is hence suggested that the nanorod structure is beneficial for relieving the efficiency droop in nitride LEDs.

In Section 3.1, the emission energy and the emission spectrum linewidth are studied. Blue-shifted emission energies and the reduced values of full width half maximum (FWHM) are observed in the nanorod structures. The theoretical fitting parameters for FWHM suggest that the electron-LO phonon scattering is largely reduced by the nanorod structure. In Section 3.2, the analysis focuses on the phonon replica of the emission spectra as a function of temperature. The mechanism of electron-LO phonon coupling and the reasons for weaker electron-LO phonon coupling effect in nanorod structures have been studied.

3.1. Optical properties for GaN/InGaN nanorods

3.1.1 Optical characterization with Photoluminescence (PL)

Photoluminescence(PL) is a process for any object to give out light after absorbing a photon. The PL measurement is widely used for measuring the optical properties[1]. In the PL measurement, the laser generates photons to excite electrons to the higher

energy levels , and then the electrons recombine with the holes in the low energy levels and give out light. Besides, non-radiative processes exist in semiconductors. Impurities, defects and interfaces in semiconductors are the potential non-radiative recombination channels.

In the PL measurement system for this study, the excitation power source is a 375nm diode laser with a stated maximum power 20mW[2]. In current use the maximum power is around 18mW. The light from the laser are reflected by a few UV mirrors and focused by the optical lenses before radiating onto the sample on the sample stage. The light generated from the sample in the photoluminescence process is then focused by another set of optical lenses. The focused light beam from the sample comes into a 0.5m SPEX 500 monochromator and is then detected by a charge-coupled device (CCD). For temperature dependent photoluminescence measurements, the samples are placed into a helium closed-circuit cryostat with temperature variance from 10K to room temperature. The schematic diagram of the PL setup is provided in Figure 3.1.

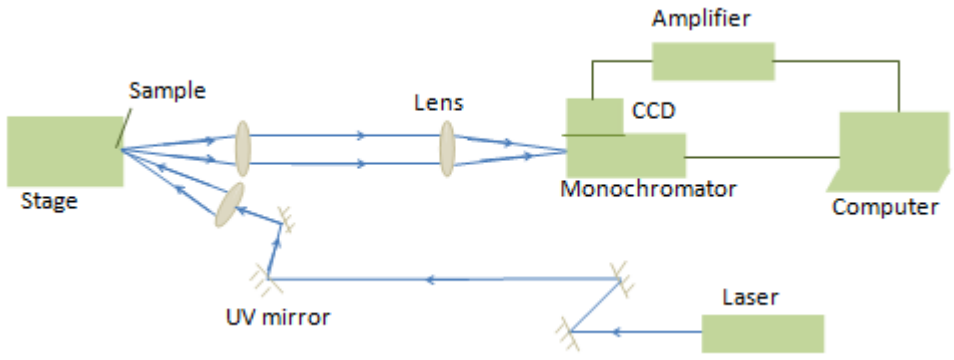

Figure 3.1 Schematic diagram of the photoluminescence setup

The working mechanism and specification for the devices are explained. The monochromator is used to separate the light of different colors spatially. The Horiba SPEX500 monochromator[3] in this laboratory is a typical Czerny-Turner monochromator, with a optical diagram illustrated in Figure 3.2. The monochromator is mainly composed of two collimator (curved mirror), M_1 and M_2,

and a grating (G_1). When the incident light is reflected onto the grating, it is diffracted and then collected by the collimator M_2. Even though M_2 makes the light collimated again, the light of different wavelengths is separated. At the exit slit, only the light in a small wavelength range can be located in the center of the exit slit and can hence pass the exit slit. By rotating the grating G_1, the dispersing element, all the light from the entrance slit can pass the exit slit gradually. In this way, the incident light is separated by its wavelength. For the SPEX 500 monochromator, the focal length is 0.5m, and the spectral range is between 0-1500nm.

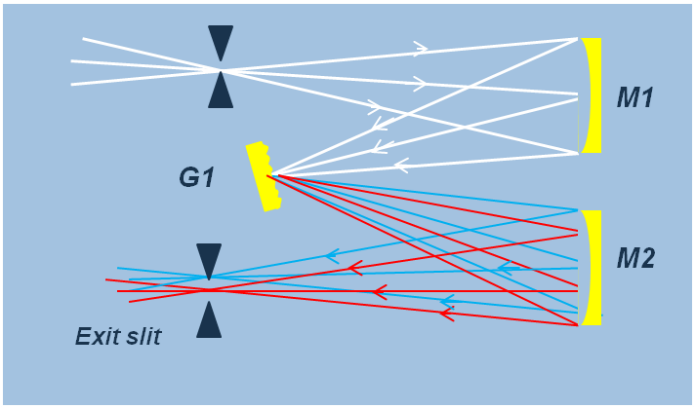

Figure 3.2 Schematic diagram of the SPEX 500 monochromator

CCD (Charge-coupled device): The CCD is connected to the monochromator and it transfers the dispersed light signal collected from the monochromator to the electric signal. The core component for the CCD is the photoactive region formed by the epitaxial layer of silicon[4].The photoactive region captures the charge which then transfers to the voltage. Such electric signals are then sent to the computer and processed to visualized images.

The cryostat is part of the cryogenics system that is used in the temperature dependent PL measurement or low-temperature PL measurement. The cryostat is connected to the Cryogenic CTI-8200-compressor[5]. The compressor uses high pressure liquid helium lines so that the temperature can go down to the boiling point of Helium at 4Kelvin. In the temperature dependent PL measurement, the

measurement temperature normally starts at 10K as indicated by the temperature meter. The sample is put in the stage inside the cryostat. The pump connected to the cryostat takes away the air inside the cryostat and makes it in a vacuum environment. It then takes around 30 minutes to lower down the temperature by the Helium bath inside the cryostat which exchanges heat with the compressor.

In this PL system, the vibration isolation system is passive, which is mainly formed by the pads and rubber. The passive vibration isolation system employs damping to reduce the amplification of the vibration. The vibration isolation table with the optical breadboard surface ensures the stability of the mounted optical components.

3.1.2 Study of the PL emission energy

The process of nanorod fabrication has been stated in Section 2.2.1. The samples in this experiment consist of two series of InGaN/GaN multiple quantum well (MQW) samples with different In composition in the QW. Each series consists of one as-grown sample and one nanorod sample based on the same wafer. The as-grown wafer structure is provided in Figure 3.3.a below. A 500nm-thick AlN nucleation layer is grown on top of the (0001) sapphire face, and a 1μm-thick GaN layer is grown followed by the InGaN/GaN QW structure (10 QWs). The InGaN QW is around 2.5nm thick and the GaN layer in between QW layers is around 8nm thick. A GaN capping layer of 10nm grows above the last InGaN QW layer. An SEM image of the nanorod structure is provided in Figure 3.3.b.

In this work, optical characterization setup has been described in Section 3.1.1 with the laser working at its full power. The PL measurement data were collected and plotted by Origin 7.5.

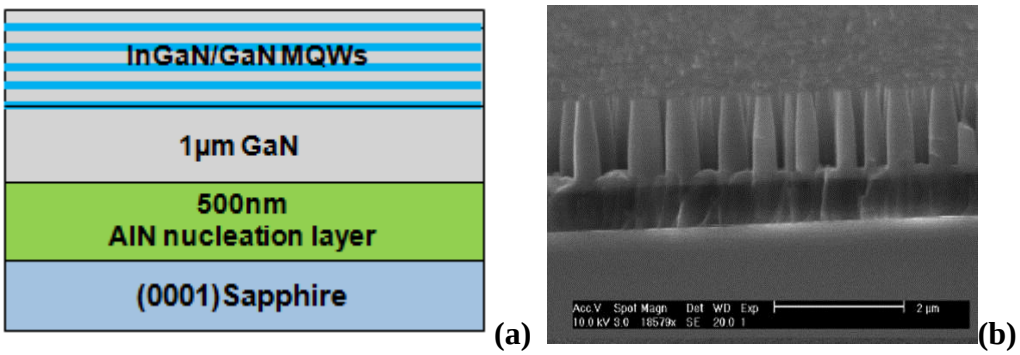

Figure 3.3 (a) Schematic diagram of the as-grown InGaN MQW wafer structure. (b) SEM image of the InGaN/GaN nanorod structure

Figure 3.4 below shows the normalized PL spectrum of two pairs (wafer number GN2217 and GN2068) of as-grown and nanorod samples for this study. The spectra are measured at 10K. The low energy shoulder in Figure 3.4 is due to the phonon replica of the main emission peak. For the as-grown and the nanorod sample with the same wafer number, they are expected to have the same growth condition and In composition (considerable In non-uniformity has been excluded before nanorod fabrication). However it's clearly noted that the emission energy for the nanorod is blue-shifted comparing to the as-grown sample for both wafers.

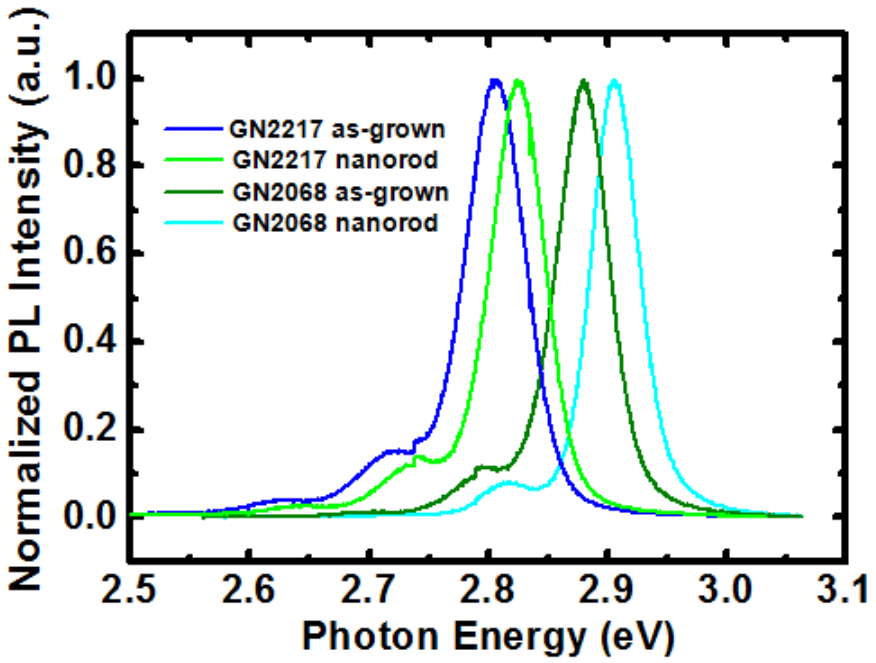

Figure 3.4 Normalized PL spectra of samples measured at 10K

Figure 3.5 below presents the reciprocal space map of the GN2068 as-grown sample and the nanorod sample. If the reciprocal lattice points (RLPs) of the QW satellite peaks fall on the fully strained line, as is in the case for the as-grown sample, it's suggested that the InGaN QWs are under full strain. If the reciprocal lattice points of the satellite peaks fall on the fully strain-relaxed line, the InGaN QWs are fully relaxed. In the reciprocal space map for nanorod structure, the satellite peaks are in a line in between the red and black dashed line, and very close to the former one. It's been calculated that the nanorod structure has released 80% of the strain in the QWs. Measurement was also taken on the other samples and similar results in the nanorod structures were presented. In all, the reciprocal space map demonstrates that the nanorod structure has partially released the strain in the InGaN/GaN MQWs.

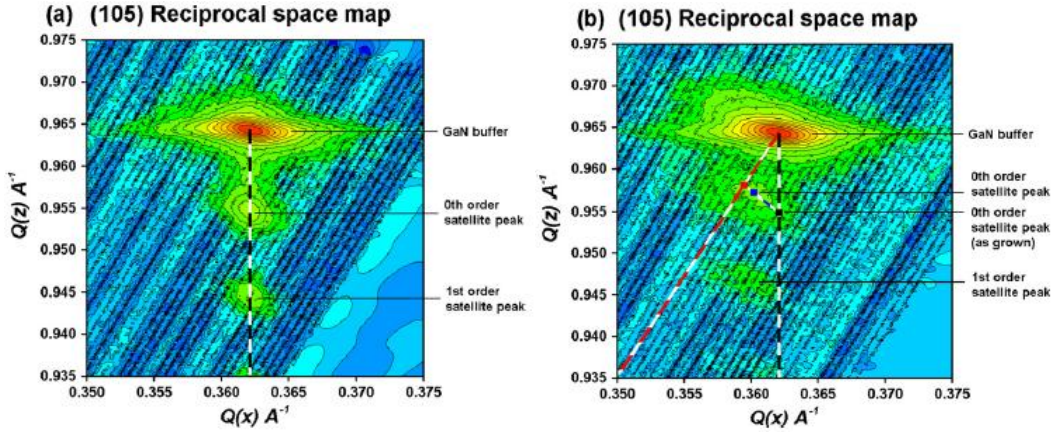

Figure 3.5 The reciprocal space map for (a) GN2068 as-grown sample and (b) GN2068 nanorod sample. The black dashed line and the red dashed line represent the fully strained line and the fully strain-relaxed line respectively

Temperature dependent PL has been conducted for further research on the four samples. Temperature varies from 10K to 300K and the procedure including the use of the cryostat has been explained in Section 3.1.1. The measurement results of the emission wavelength as a function of temperature are plotted in Figure 3.6. It demonstrates a prominent S-curve of the emission energy for all samples: at low temperature (normally smaller than 100K), an initial red shift is observed. During

the intermediate temperature range (from 100K to 200K), a blue shift appears. As temperature rises up (from 200K to the room temperature), the red shift of the emission energy once again occurs.

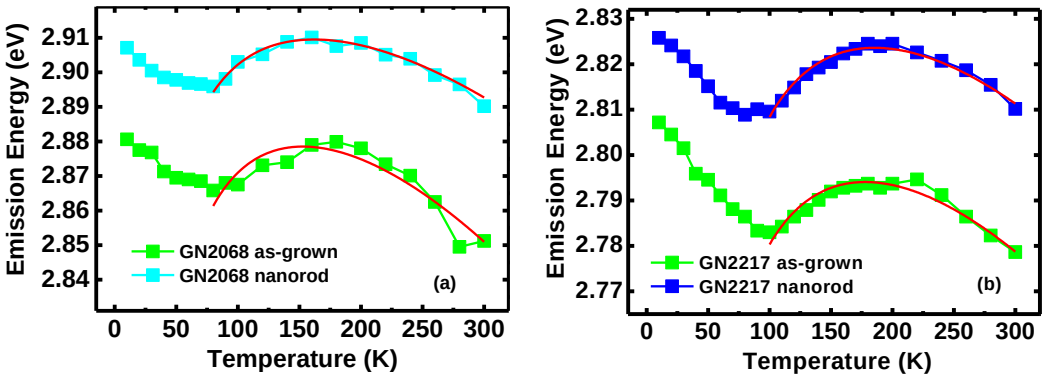

Figure. 3.6 The curve of emission energy as a function of temperature for all samples. The red lines are the fitting curves according to Equation (3.1)

The S-curve of emission energy indicates that there exists some other mechanism apart from thermal band-gap shrinkage [6]. A general interpretation is the exciton delocalization process. At a low temperature below 50K, excitons tend to be distributed in the deeply localized states through the hopping process. However, as temperature goes up, the thermalized excitons begin to occupy higher energy states, which induces a blue shift that goes against the thermally induced red shift. As temperature continues increasing, the delocalization process gets saturated, and hence the blue shift is not strong enough to compensate the thermal shrinkage. The overall trend appears to be red shift once again. This is how the S-curve is formed.

In order to theoretically understand the S-curve, the band-tail model[7] has been adopted to fit the emission energy as a function of temperature:

$$E(T) = E_0 - \frac{\alpha T^2}{T+\beta} - \frac{\sigma^2}{k_\beta T} \qquad (3.1)$$

Where α and β are both Varshni fitting parameters, σ is the parameter that's related with the blue shift of the emission energy, and E_0 is the emission energy at zero temperature. k_B is the Boltzmann constant. In the original Varshni model, only the

first two terms (E_0-$\alpha T^2/(T+\beta)$) are considered. The parameter α does not have a concrete physics meaning, but it describes the strength of thermal expansion when temperature increases. The parameter β is in the unit of the temperature. It is taken to be close to the Debye Temperature[8], which is the temperature limit that can be achieved from a single normal vibration[9].

The fitting curve based on Equation (3.1) has been plotted as the red curves in Figure 3.6. The fitting parameters including E_0, α, β and σ for these samples are listed in Table 3.1 below. The fitting results are consistent with the parameter values of GaN in literature[10].

Table 3.1 Fitting parameters of emission energy curves

	E_0 (eV)	α(meV·K^{-1})	β (K)	σ(meV)
GN2068 as-grown	2.927	0.68	732	20.3
GN2068 nanorod	2.949	0.50	730	18.7
GN2217 as-grown	2.843	0.52	738	22.2
GN2217 nanorod	2.871	0.46	741	22.3

Comparing the as-grown and the nanorod sample for both GN2068 and GN2217, the scale of the blue shift during the intermediate temperature range does not vary significantly between the as-grown and nanorod sample. The delocalization effect is an intrinsic property of the InGaN materials, and hence is not expected to be changed by the nanorod structure. This is also proved by the fitted value for σ, an indication for the strength of the localization effect. The value of σ for each as-grown and nanorod pair is very similar, and the small difference can be attributed to slight non-uniformity of the wafer.

However, the nanorod structure does make a difference in the emission energy curve which can be captured by the Varshni parameter α. For both GN2068 and GN2217,

the total scale of red shift is much stronger in the as-grown sample than in the nanorod sample. This is because, the nanorod structure facilitates heat dissipation. This relieves the thermal expansion and hence causes smaller red shift as temperature rises.

3.1.3 Study of the spectral linewidth

Another optical property studied is the emission spectral linewidth. The FWHM (Full Width Half Maximum) measures the spectrum linewidth at half of the height of the emission peak[11].

This study investigates the same samples used for the study of the emission energy . The FWHM for all samples at different temperatures is plotted in Figure 3.7. Comparing with the S-curve of the emission energy, an interesting W-curve of FWHM as a function of temperature can be observed. In the initial stage, the line width is almost a constant or even drops slightly as temperature increases. Above around 50K, a prompt increase is observed in linewidth. However this does not last long and from around 100K, the broadening rate of FWHM becomes much slower even though FWHM is still increasing. This temperature range (100K-180K) corresponds to a flat part of the W-curve. From around 180K to room temperature, the broadening rate becomes strong again. Therefore, two periods of sharp rise and two periods of flat parts form the shape of "W" in the curve.

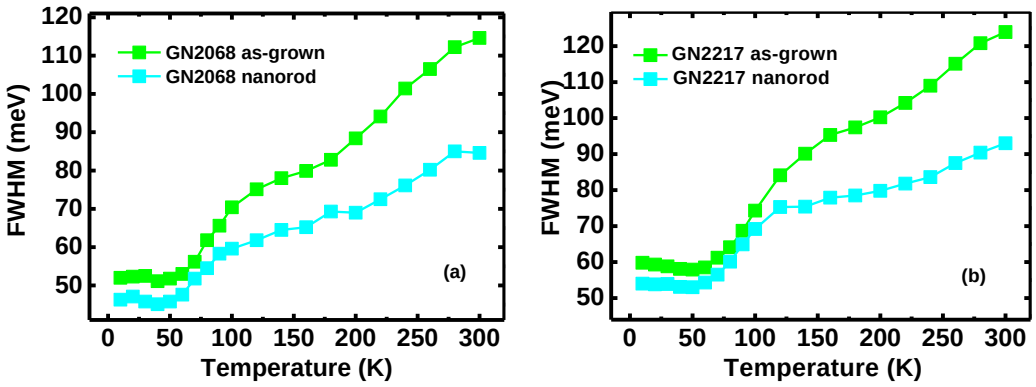

Figure 3.7 FWHM as a function of temperature for all samples

The formation of the W-curve of FWHM can be interpreted in the following way[12]: at very low temperature(below 50K), most excitons are not fully thermalized and they tend to be located in the deep-localized states via the hopping process [6]. Consequently, a slight red shift of FWHM appears because the distribution of excitons is concentrated in the deep-localized states. In the next stage (around 50K-100K), the thermalized excitons due to the higher temperature can be distributed at higher energy levels of the localized states. Excitons occupy a wide variety of energy levels, thus resulting in the sharp increase of FWHM [12]. As temperature further rises, starting from around 100K to 180K, the delocalization process is dominant. The thermalized excitons in the localized states become free and gain considerable momentum. Since an increasing number of the excitons get out from the trap of the localized states, the energy distribution becomes narrow again and the broadening rate of FWHM slows down. When temperature is above 180K, the effect of delocalization does not play an important role because most of excitons have become free. The rapid broadening of FWHM is then associated with the phonon scattering mechanisms.

Figure 3.8 presents the comparison of the emission energy (S-curve) and the FWHM (W-curve) for each sample in every figure. It is clearly noted that the flat part of the W-curve (at 120K-180k) matches the blue shift of the S-curve very well. Both have been interpreted as the effect of the exciton delocalization process during this temperature range. At above 180K, the stronger broadening rate of FWHM and the red shift of the emission energy are both attributed to saturation of the delocalization process.

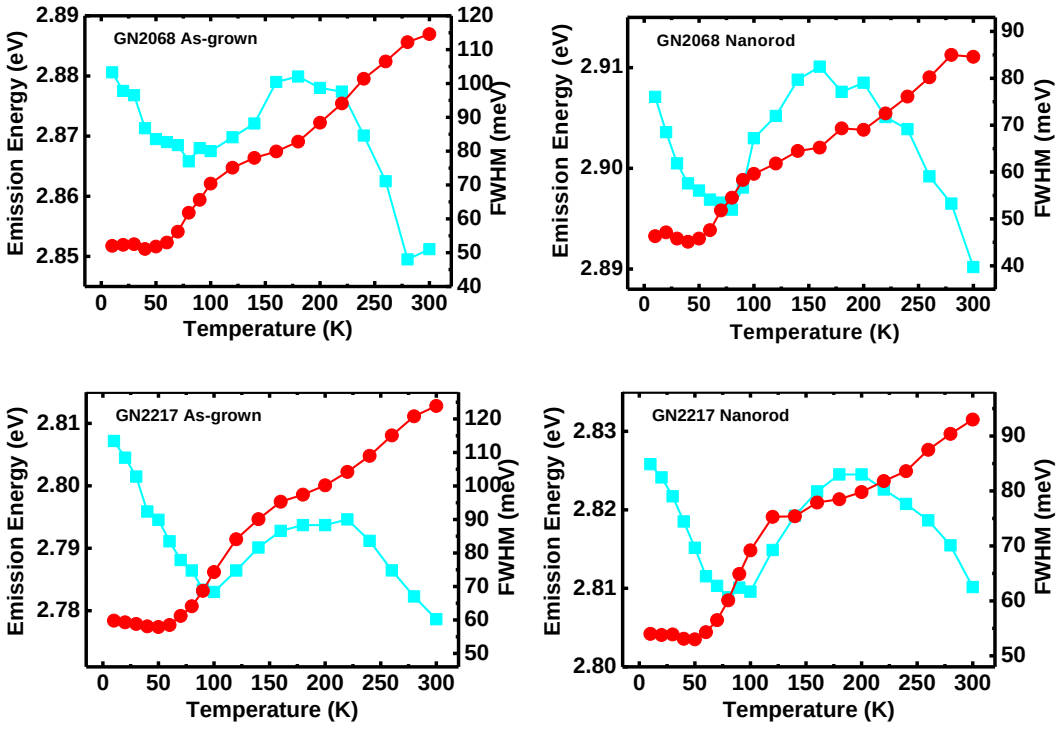

Figure. 3.8 The emission energy and FWHM as a function of temperature for each sample

When both effects of exciton localization and delocalization can be excluded at higher temperature (180K-300K for GN2068 and 200K-300K for GN2217), the FWHM broadening can be explained by the conventional carrier-phonon scattering mechanism as described in Equation(3.2)[13]:

$$\Gamma(T) = \Gamma_0 + \gamma_{ph} T + \frac{\Gamma_{LO}}{\exp(E_{LO} / k_B T) - 1} \qquad (3.2)$$

Where E_{LO} is the longitudinal optical (LO) phonon energy. The LO-phonon energy is around 91meV for GaN and 72meV for InN[14], so for InGaN with an Indium composition of around 10%-15%, a reasonable value of E_{LO} is around 89meV. Γ_0 is the parameter for linewidth at zero temperature. γ_{ph} here is the parameter for exciton-acoustic phonon interaction. Γ_{LO} is the parameter for exciton -LO phonon coupling strength. k_B is the Boltzmann Constant and T is the temperature.

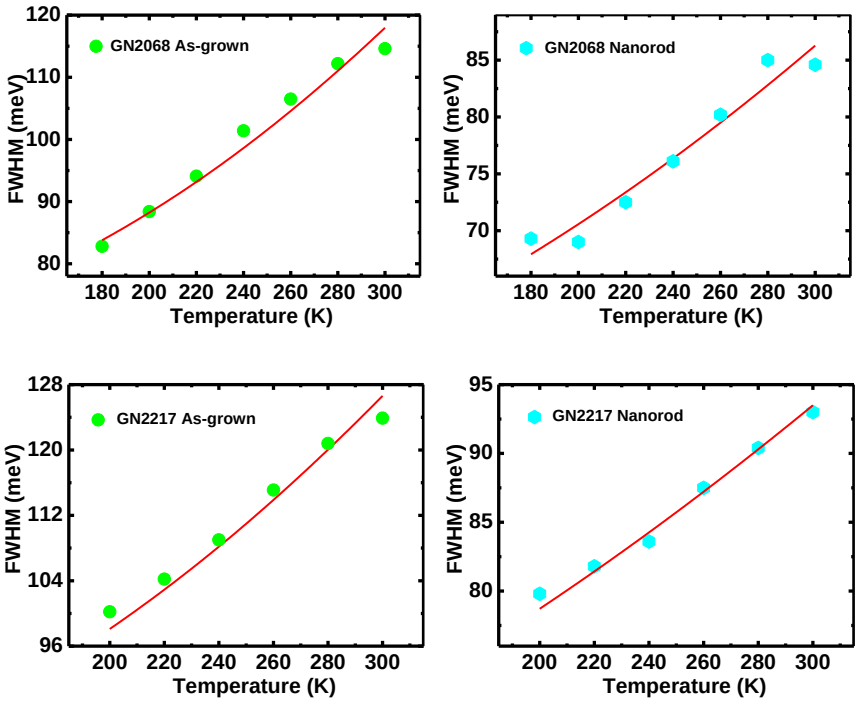

Figure 3.9 Fitting results of FWHM for all samples based on Equation (3.2). The red curves indicate the fitting curves

Figure 3.9 provides the fitting results for the four samples based on Equation (3.2) . The values of these fitting parameters are listed in Table 3.2.

Table 3.2 Fitting parameters for FWHM based on Equation (3.2)

	Γ_0(meV)	γ_{ph}(μeV·K^{-1})	Γ_{LO} (meV)
GN2068 as-grown	53.7	158	510.5
GN2068 nanorod	47.4	111	168.9
GN2217 as-grown	63.1	162	451.7
GN2217 nanorod	55.2	114	124.0

The values for the parameters are consistent with the results for other wide band-gap materials such as ZnO [13]. Note that for GN2217 as-grown sample (emission wavelength of 445nm at 10K), FWHM is always larger than that in GN2068 as-grown sample (emission wavelength of 431nm at 10K) at the same temperature. GN2217 of higher In composition is expected to have a lower quality (e.g. surface

scattering, impurity and dislocation) that induces a higher FWHM [11].

The parameter for the exciton-acoustic phonon coupling strength has been reduced in the nanorod structure for both GN2068 and GN2217. Acoustic phonon scattering mechanisms are mainly associated with the deformation potential scattering and the piezoelectric field scattering [15,16]. As strain is reduced by the nanorod structure, the acoustic phonon scattering is slightly impaired. Γ_0 is also slightly lower for the nanorod structure comparing with the as-grown samples. It can be related to the fact that the nanorod structure has taken away a portion of the InGaN/GaN materials and the total amount of dislocation is likely to be reduced.

On the other hand, a significant difference between the nanorod samples and the as-grown samples is found in Γ_{LO}, the parameter for the electron-LO-phonon scattering strength. The values of Γ_{LO} for the nanorod samples are only 20%-30% of those for the corresponding as-grown samples. The LO-phonons follow a polar scattering mechanism[17] with their center mass fixed. According to Equation (3.2), the LO-phonon scattering causes a nearly exponential increase of FWHM as a function of temperature ($\Gamma_{LO}/[\exp(E_{LO}/k_BT)-1]$), while the acoustic phonon cause a linear increase of FWHM ($\gamma_{ph}T$). Hence the LO-phonon scattering is a most decisive factor for FWHM at this temperature range (180K-300K). It's clear that the nanorod structure suppresses the LO-phonon broadening and effectively reduces the increase of FWHM. However, a detailed mechanism of the LO-phonon scattering and the influence of the nanorod structures have to be further investigated. A more systematic study focused on the electron-LO-phonon coupling mechanism in the nanorod structure is provided in Section 3.2.

3.2. Study of electron-longitudinal optical (LO) phonon coupling in GaN/InGaN nanorod structures

3.2.1. Electron- LO phonon coupling and the Huang- Rhys factor

Phonon is a quasi-particle and quantization of the elastic vibration in quantum mechanics. In the lattice with atoms connected, the displacement of one atom could cause a vibration wave. The connection between each pair of two atoms can be regarded as a spring. The dispersion relationship between the angular frequency ω_k and the wave number k can be calculated according to the kinetic energy theorem[18]. For a one-dimensional chain with two different kinds of atoms, with a mass of m_1 and m_2 respectively, the dispersion relationship between ω_k and k becomes:

$$\omega_{\pm}^2 = K(\frac{1}{m_1}+\frac{1}{m_2}) \pm K\sqrt{(\frac{1}{m_1}+\frac{1}{m_2})^2 - \frac{4\sin^2(ka/2)}{m_1 m_2}} \,. \qquad (3.3)$$

When there is a plus sign in the equation, the dispersion curve corresponds to the optical phonons, and when there is a minus sign, the dispersion curve corresponds to the acoustic phonons [15]. The schematic of dispersion curve of the optical mode and the acoustic mode is provided in Figure 3.10. In the optical phonon mode, the two adjacent atoms oscillate in the opposite direction so that the mass centre is fixed. It's named as the optical phonon because it can easily couple with the light due to a high angular frequency (up to $10^{13}s^{-1}$) corresponding to the Infrared region. In the acoustic phonon mode, the two adjacent atoms oscillate in the same direction. The acoustic wave has a lower angular frequency which can be comparable to the sound wave. This is why it's named as the acoustic phonon.

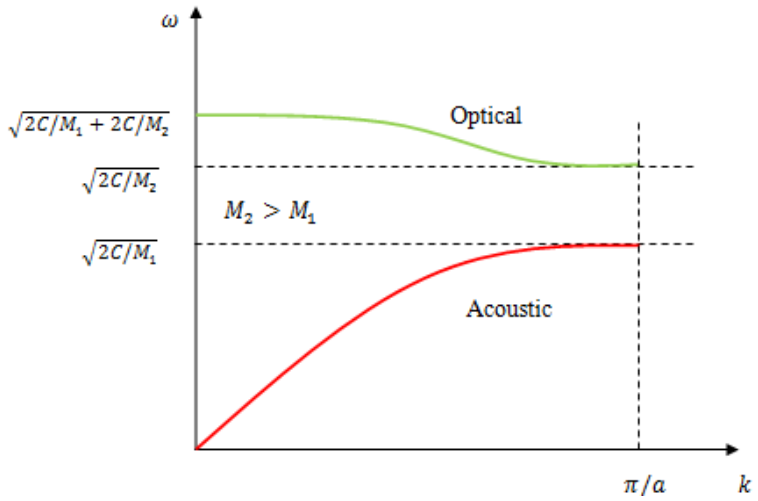

Figure 3.10 Schematic diagram of the dispersion curves for optical and acoustic phonons

For optical phonons and acoustic phonons, both the longitudinal mode and the transverse mode exist. The longitudinal optical mode, the transverse optical mode, the longitudinal acoustic mode and the transverse optical mode are abbreviated as LO, TO, LA and TA mode respectively[19]. The difference between the longitudinal mode and the transverse mode lies in that: in the longitudinal wave (e.g. the sound wave), lattice oscillation and wave propagation are in the same direction, while in the transverse wave (e.g. the light wave), the oscillation direction is vertical to the wave propagation direction.

The coupling between an electron and a phonon is essentially the scattering of electrons by the crystal lattice vibration. Generally the scattering process has to satisfy the quasi momentum balance and the conservation of kinetic energy. For optical phonons, the phonon energy is high (as illustrated in Figure 3.10) which causes a big change in the electron energy. Such process is called the inelastic scattering [17]. In the longitudinal optical phonons, two adjacent atoms oscillate in the opposite direction at a high frequency, which generates a localized polarization field[17].

Through the coupling of electrons and the longitudinal optical phonons, the electron loses certain amount of energy. Such energy is of a quantitized value, which is the

product of any integer and the LO phonon energy. Electron-LO phonon coupling is very common in II-VI and III-V semiconductor materials. The values of the LO-phonon energy for some II-VI and III-V semiconductor materials are: 91meV for GaN[20], 36meV for GaAs[21], 72meV for ZnO [22], 31meV for ZnSe [23]and 37meV for CdS [23].

The electron-LO phonon coupling can be easily observed in photoluminescence (PL) measurements. Normally, the emission spectrum can be fitted by a single Gaussian peak. When the electron-LO phonon coupling process occurs, there is at least one side peak on the lower energy side of the emission peak. The energy separation between the first side peak and the emission peak is around the LO phonon energy for this semiconductor. The second and third side peaks are also apart from the adjacent peak with an energy close to the LO phonon energy. These satellite peaks on the lower energy side of the emission peak are called the phonon replica .

The Huang-Rhys (H-R) factor [24] has been a common index in measuring the strength of the electron–LO phonon coupling. *S*, the H-R factor, is associated with the electron-LO phonon coupling matrix and sum it over the whole wave vector space[20]. In practice, the value of *S* is estimated using the PL intensity of different PL peaks:

$$S_n = (n+1)\, I_{n+1}/I_n \ .(n=0, 1, 2\ldots). \qquad (3.3)$$

Where *n* is the number of the PL peak, and *n* = 0 refers to the zero phonon peak, i.e. the main emission peak.

The features of H-R factors in electron-LO phonon coupling have been widely studied in the II-VI and III-V semiconductors, such as InAs quantum dots(QD) and InGaN/GaN quantum well (QW)[25,26,27,28]. Power dependent and temperature dependent PL measurements have been employed in probing the mechanism of the electron-LO phonon coupling. In literature of the electron-LO phonon coupling

mechanism for InGaN/GaN QWs, the H-R factor varies in samples of different In composition [26, 28]. Generally, the InGaN QW in the green spectrum range has a stronger electron-LO phonon coupling than the samples in the blue spectrum range because of the higher Indium content[26]. In the meantime, the number of QWs is found to have an influence on the electron-LO phonon coupling[29] which is attributed to the residual strain.

The electron-LO phonon coupling mechanism has recently been studied on InGaN QW nanorods[20]. This study is consistent with previous research on the Huang-Rhys factor, and yet did not point out the special features of the nanorod structures in the electron- LO phonon coupling process.

Currently, most research of the nanorod structure focus on the emission energy and the linewidth(FWHM). On the other hand, it would be meaningful to study the electron-LO phonon coupling properties for the nanorods in order to gain a more comprehensive understanding of InGaN QW nanorod structrues.

It has been pointed out that the indirect Auger recombination (IAR) process plays an significant role in reducing the emission efficiency[30]. The longitudinal optical (LO) phonon–electron coupling is one mechanism that assists the IAR process and hence the droop.

By measuring the H-R factor for a series of MQW samples (both as-grown samples and nanorod samples) with different emission wavelengths, the intensity of electron-LO phonon coupling could be estimated for each sample. It would be interesting to know how the coupling strength varies for samples of different indium content, and how nanorod structure could possibly change the coupling strength. This research renders useful information for further study of the indirect Auger recombination process and the issue of the efficiency droop.

3.2.2 Reduction of electron-LO phonon coupling strength in GaN/InGaN nanorod structure

Five pairs of InGaN/GaN multiple quantum well samples (Each pair includes one as-grown sample and one nanorod sample) with different Indium composition and emission energy, are included in this study. The structure of InGaN/GaN quantum wells and fabrication methods of nanorod structures are consistent with those in Section 3.1. The list of samples in this study with their emission wavelength measured at 10K is provided in Table 3.3.

Table 3.3 The emission wavelength for each sample measured at 10K

(Note: Ag2219 : GN2219 as-grown sample; Nr2219 : GN 2219 nanorod sample)

Name	Wavelength (nm)	Name	Wavelength (nm)
Ag2219	427.4	Nr 2219	424.3
Ag2217	449.0	Nr 2217	439.0
Ag2284	461.8	Nr 2284	458
Ag1719	501.8	Nr 1719	471.6
Ag1716	539.2	Nr 1716	498.4

PL measurement for all the samples here is excited by the 375nm diode laser, with an excitation power of 18mW. Note that the samples are loaded in a closed circuit helium cryostat for low temperature measurement, the real excitation power on top of the samples can be attenuated slightly. A heater is also connected in the setup, so that samples could be heated up to room temperature for normal PL measurement. The excitation power density is around 100W/cm^2 considering the laser spot radius as 125 μm.

The normalized PL spectrum from both nanorods and as-grown samples measured at 10K are plotted in Figure 3.11 in the logarithm scale. The linewidth (FWHM) is

broadening as the indium composition and the emission wavelength increases. One or two satellite peaks are observed along the right side of the main peak, and the satellite peaks get more prominent as sample's emission wavelength increases. In each pair of the as-grown and the nanorod sample, the emission wavelength of the nanorod is blue shifted compared with the as-grown sample, and as the emission wavelength of the as-grown sample rises, the difference in the emission energy becomes larger between the as-grown sample and the nanorod sample. For instance, the emission wavelength separation for pair of GN2219 samples is only 3nm, while the value for the pair of GN1719 samples is as large as 26nm. This is because, the nanorod structure reduces the strain, and the strain reduction effect is stronger for samples of high Indium composition in which a higher intrinsic strain is expected. In addition, the satellite peak for the nanorod is always smaller than that for the corresponding as-grown structure, indicating a weaker electron-LO phonon coupling in the former.

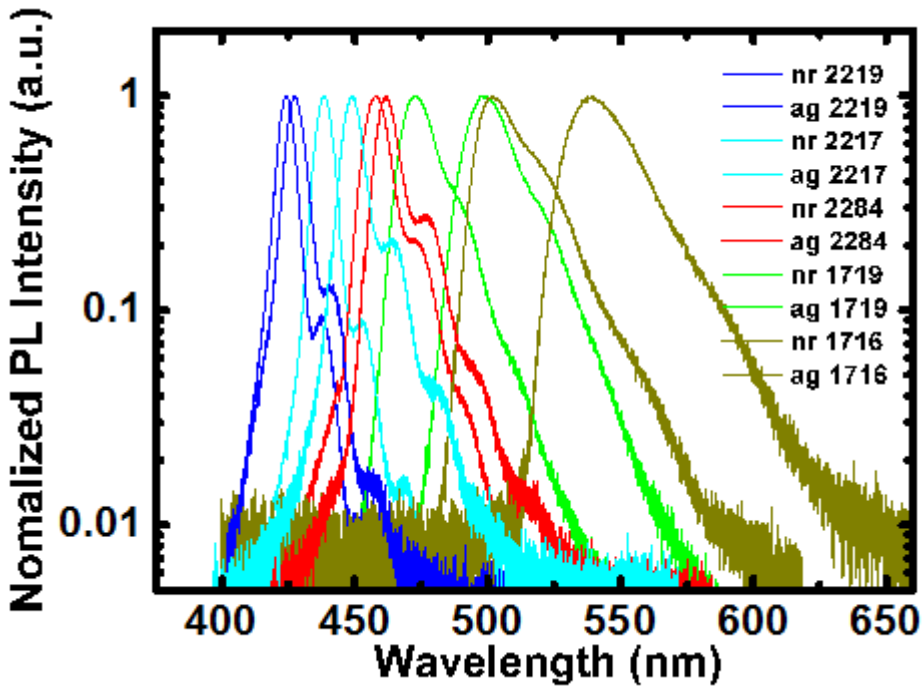

Figure 3.11 Normalized PL spectra for the samples measured at 10K. In each pair of samples of the same wafer number, the nanorod sample has a shorter emission wavelength comparing with the as-grown sample

The concept of the Huang-Rhys factor has been adopted here to describe the electron-LO phonon coupling effect. For each PL spectrum, it is normalized and the following fitting process is applied to the spectrum: The nonlinear curve fitting with multiple peaks (a built-in function of Origin) is adopted. For each peak, it follows the Gaussian distribution and owing to the feature of phonon "replica", the FWHM for each Gaussian peak is set identical during the fitting processes. Besides, the emission energy separation of two adjacent Gaussian peaks is fixed for each sample of certain Indium composition. Since the LO-phonon energy is 91meV for GaN and 72meV for InN, the LO-phonon energy for InGaN with Indium composition of 10%-20% is around 87-89meV through the linear interpolation method. The cumulative curve of these multiple Gaussian peaks is expected to coincide with the experimental PL spectrum. An example of the multiple-Gaussian-peaks fitting for GN2284 as-grown sample (measured at 10K) is provided in Figure 3.12.a.

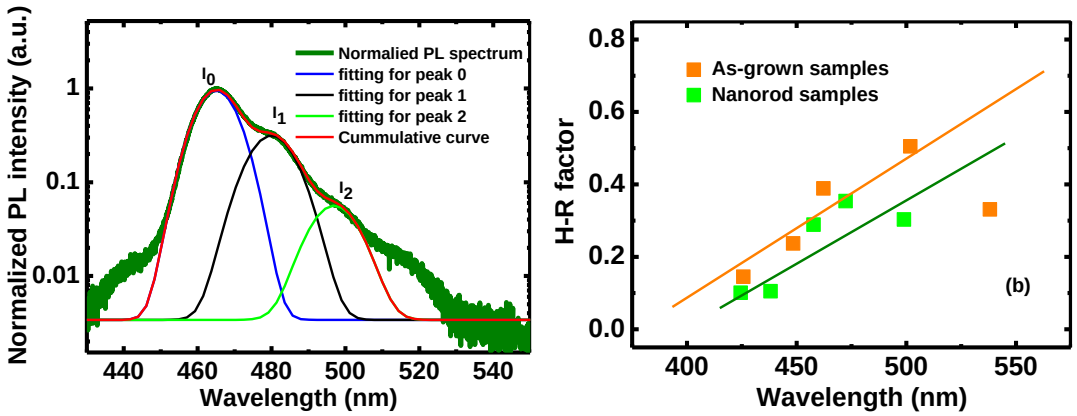

Figure 3.12 (a) An example of multi-Gaussian-peaks fitting for phonon satellite peaks. (b) The calculated H-R factors for nanorod samples and as-grown samples with different emission wavelengths measured at 10K. The red and the green lines indicate the trend of the H-R factors as a function of the wavelength for the as-grown and nanorod samples respectively

With getting the fitting curves for each sample, the area of the satellite peak and the main peak can be obtained. The H-R factor for each sample can then be calculated as the ratio of the area of the first satellite peak to that for the main peak [20], according to Equation (3.3): $S_n = (n+1)\ I_{n+1}/I_n$.(n=0, 1, 2…).Where n is the number of the PL peak, and n = 0 refers to the zero phonon peak, i.e. the main emission peak.

I_n refers to the area of the n^{th} peak.

The first satellite peak is concerned with the LO-phonon coupling with all recombining excitons. On the other hand, the higher order satellite peaks are only contributed by those deeply–confined excitons which are a small portion of excitons, and are not strongly explanative of the general LO-phonon coupling mechanism[20]. In the meantime, the higher order satellite peaks cannot be clearly observed in samples of a high emission energy (up to 500nm) because their linewidth becomes much broader. This makes it difficult to measure the higher order satellite peaks accurately. Therefore, higher order satellite peaks are not to be discussed. Only the first order H-R factor S_0 is concerned in this study.

Figure 3.12.b presents the H-R factor for the sample assemble measured at 10K. A clear increasing trend of the H-R factor is noted as the emission wavelength gets higher. More importantly, for the five pairs of samples, the nanorod sample always has a lower H-R factor than its corresponding as-grown sample. An average 20% reduction of the H-R factor is demonstrated in these nanorod samples at 10K, indicating a partial reduction of the electron-LO phonon coupling strength in the nanorod structures.

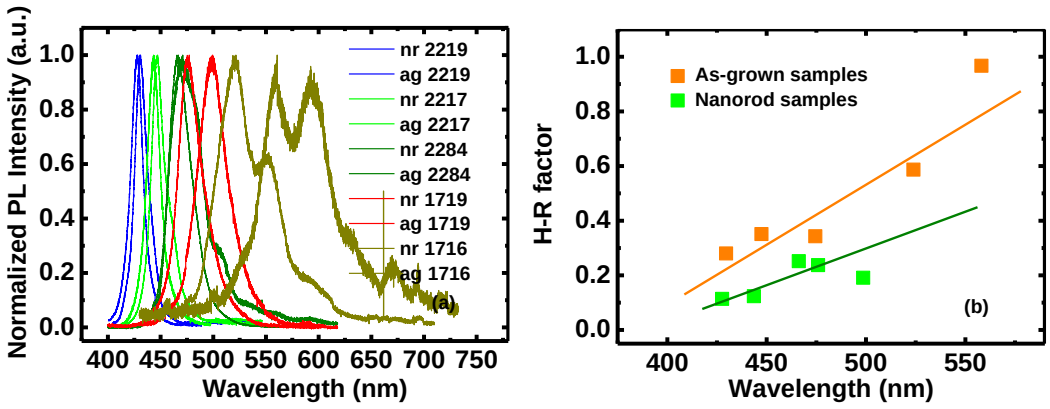

Figure 3.13 (a) Normalized PL spectra for samples measured at room temperature (b) The calculated H-R factors for as-grown samples and nanorod samples with different emission wavelengths. The red and the green lines indicate the trend of the H-R factors as a function of the wavelength for the as-grown and nanorod samples respectively

Besides, the H-R factor is calculated for these samples measured at room temperature. The PL spectra and the H-R factors are plotted in Figure 3.13.a and Figure 3.13.b. The trend that the nanorod structure reduces the H-R factor, as well as the positive correlation between the H-R factor and the emission wavelength, also exists at room temperature. Although an H-R factor as high as 0.9 is questionable and the large side peak for the sample in the deep green spectrum might be due to the high Indium non-uniformity, other samples clearly demonstrate the phonon satellite peaks and have a reasonable value of the H-R factor. In addition, H-R factors for all the as-grown samples at room temperature are much higher than those measured at 10K. On the other hand, the H-R factor for the nanorod structured does not change significantly. At room temperature, the nanorod structure demonstrates an 40%-50% reduction of the H-R factor on average, which indicates a stronger reduction of the electron-LO-phonon coupling. This could be related to the fact that, as the temperature is raised, the number of phonons increases, which leads to a stronger electron-LO-phonon coupling and hence the effect of the nanorod structure is more important.

The fact that the H-R factor rises with increasing the emission wavelength, has been observed in literature[26,28]. Larger In composition causes a lower quality of the InGaN QW with more defects, which contribute to the LO-phonon scattering. However, influences of the nanorod structure on the H-R factor have not been covered. The latter is studied with more theoretical support in Section 3.2.3.

3.2.3 Mechanism of the influence of the nanorod structure on electron -LO phonon coupling

This section gives an explanation why the nanorod structure reduces the H-R factor which is an indication of the electron-LO phonon coupling strength. For the wurtzite QW heterojunction structure, there exist several optical phonon modes, including the interface phonon mode and the propagating mode [31]. For the former, the phonon

wave vector perpendicular to the QW layer is imaginary and the corresponding field decays exponentially away from the interface. For the latter mode, the perpendicular phonon wave vector is real. It's been suggested that, for a 2-3nm thick wurtzite QW, the interface phonon mode is the primary mode in electron- LO phonon coupling[29,31,32].

Figure 3.14 illustrates the mechanism of the interface phonon mode and the electron-LO phonon coupling. The symmetric and asymmetric mode refer to the electron-LO phonon coupling function, $\Gamma(q, z)$, for wavevector q at position z(z axis is perpendicular to the layer interface). $\Gamma(q, z)$ is in the unit of $(\text{meV}\cdot\text{nm})^{1/2}$ and it has a higher absolute value at the layer interface, especially for the asymmetric mode. In the mean time, for a 2-3nm thick InGaN quantum well, the polarization field could reach to a magnitude of MV/cm[29]. The electron and hole wave functions are hence distributed close to the interface as a result of the large strain.

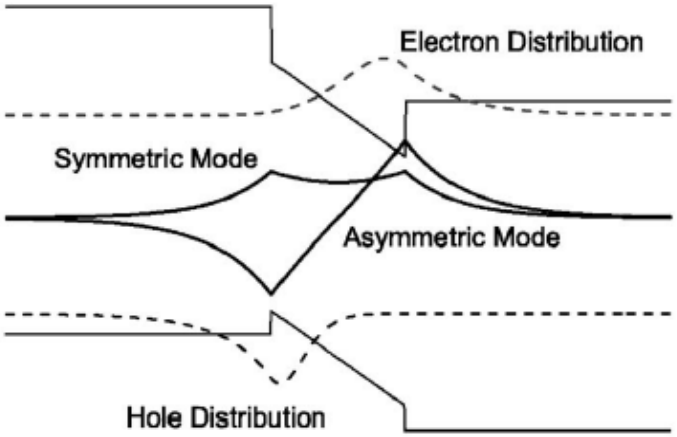

Figure 3.14 Schematic diagram of the band structure in the electron-LO-phonon coupling mechanism [29]

The electron-LO phonon coupling in the interface phonon mode can be further approached. The coupling strength S, or Huang-Rhys factor, follows a relationship described in Equation (3.5) [29]:

$$S \propto \sum_{q} \left\{ M_1 \int dz_e |\psi(z_e)|^2 \Gamma(q, z_e) - M_2 \int dz_h |\psi(z_h)|^2 \Gamma(q, z_h) \right\} \qquad (3.5)$$

where, M_1 and M_2 are related with m_e and m_h (the effective mass for electrons and holes respectively). $|\psi(z_e)|^2$ and $|\psi(z_h)|^2$ refer to the field strength of the electron and hole wave function respectively. From Equation (3.4), the coupling is in fact related to two aspects: both the electron-LO phonon coupling function, and the electron/hole wave function. The coupling strength S is then proportional to the convolution of the two functions mentioned above. Note that there is a minus sign in equation (3.4) and the coupling strength $\Gamma(q,z_h)$ with holes is also of a negative value for the asymmetric mode as depicted in Figure 3.14. Therefore, the total value of S is positively correlated with the absolute coupling strength $|\Gamma(q,z)|$.

The difference in the electron-LO phonon coupling between the as-grown samples and the nanorod samples is analyzed. The reciprocal space map in Figure 3.3 demonstrates that the nanorod structure has released much strain of the InGaN QWs while the as-grown sample is fully strained. Consequently, the Quantum Confined Stark Effect (QCSE) is partially relieved in nanorod. From Figure 3.14, for the nanorod structure, the energy band is less tilted, which means the separation of the electron wave function and the hole wave function is smaller, i.e., both wave functions gather towards the center of the quantum well. However, in the interface phonon mode, the electron-LO phonon coupling function would always segregate at the interface. For both symmetry and asymmetry modes as illustrated in Figure 3.14, the function's absolute value reaches their maximum at the interface. Therefore in the nanorod structure, the center of wave functions is further away from the interface, which makes the convolution smaller than that in the as-grown structure. Correspondingly, the H-R factor in the nanorod samples is reduced.

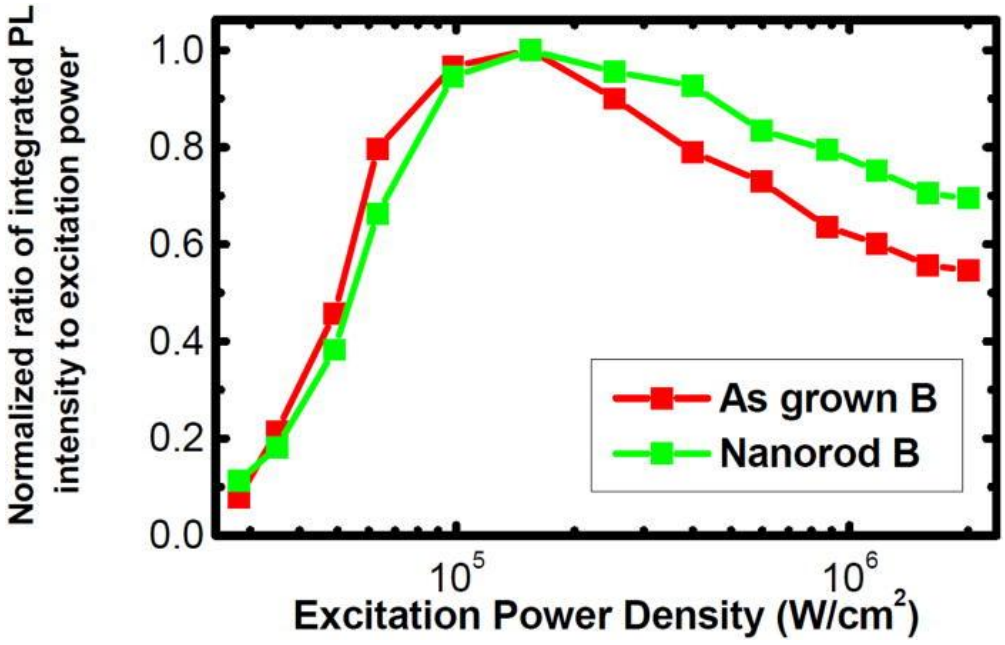

Figure 3.15 Normalized PL intensity of the as-grown sample and the corresponding nanorod sample measured by power dependent PL at room temperature in identical conditions [14]

Under the fact that InGaN/GaN nanorod structures could reduce the H-R factor and hence the electron-LO phonon coupling strength, the InGaN/GaN nanorod structure is supposed to relieve the LED device droop by reducing the indirect Auger recombination, according to the previous hypothesis. To prove this, colleagues in this group [14] carried out the power dependent PL measurement for a pair of one as-grown sample and one nanorod sample by a diode pumped Nd:YAG laser. The normalized PL intensity is shown in Figure 3.15. Note that the normalized PL intensity is not equivalent to the external quantum efficiency which is obtained by the EL measurement. However, a relative comparison of the intensity droop for the as-grown sample and the nanorod sample is still useful.

From Figure 3.15, it's found that, in the nanorod sample, the PL intensity drops 30% at a high excitation power density of 2×10^6 W/cm^2 comparing with the peak power density, while in the as-grown sample it drops 45% comparing with its peak power density. The peak PL intensity for the as-grown sample is 1.4 times higher than that for the nanorod sample, which is probably owing to the reduction of the material in the nanorod structure. However, the nanorod structure has still effectively reduced

the efficiency droop at a high power density compared with the as-grown structure. Note that this experiment is carried out on the LED wafers. Further research on the droop issue of the LED device that contains the nanorod structures is highly suggested.

3.3. Summary

Reduction of the strain has been a main function of the nanorod structures for the InGaN/GaN QWs. Because of the strain reduction and consequently the reduction of QCSE, InGaN/GaN nanorod samples always exhibit a blue shift of the emission energy comparing with the as-grown samples at different temperatures. Since InGaN nanorod structures impair the phonon-assisted broadening process, the FWHM in the InGaN nanorod samples is always smaller than that in the as-grown samples.

In order to further probe the mechanism of the nanorod structure in reducing the LO-phonon coupling effect, the phonon replica of the emission peak in the PL spectra are researched. The ratio of the phonon replica and the main peak, known as the Huang-Rhys Factor, reflects the strength of electron–LO phonon coupling. The InGaN/GaN nanorod structure partially releases the strain in the multiple quantum wells(QW) and consequently reduces the possibility of electron-LO phonon coupling at the interface of the QWs and GaN barriers. From the PL measurement, the nanorod sample exhibits a much lower satellite peak which suggests a much lower value of the H-R factor and a weaker electron-LO phonon coupling effect. Since the LO phonon scattering is one major channel for the indirect Auger recombination which is regarded a main cause of the LED efficiency droop, the reduction of electron-LO phonon coupling in the nanorod structure suggests a reduced efficiency droop. This has been proved by later research in this group [14]. The nanorod structures have promising applications in fabricating high-efficiency nitride LEDs.

Reference

[1] Kira, M. & Koch, S. W. (2011). *Semiconductor Quantum Optics.* Cambridge: Cambridge University Press, pp, 38

[2] Crystalaser. 375nm diode laser specification. Retrieved from: http://www. crystalaser. com/new/uv-laser.html

[3] Horiba. SPEX500 monochromator specification. Retrieved from : http://www. horiba. com/ fileadmin/uploads/Scientific/Documents/OSD/MSeries.pdf

[4] Boyle, W. S. & Smith, G. E. (1970). Charge Coupled Semiconductor Devices. *Bell Sys. Tech. J.* 49 (4): 587–593

[5] Cryogenic CTI-8200-compressor Retrieved from: http://www.brooks.com/ products/cryopumps-cryochillers/cryochillers/compressors

[6] Lee, K.B. (2009). *Fabrication and Characterisation of AlGaN based Ultraviolet Light Emitting Diodes, Chapter 4.* PhD thesis, University of Sheffield

[7] Eliseev, P. G., Perlin, P., Lee, J., & Osinski, M. (1997). "Blue" temperature -induced shift and band-tail emission in InGaN-based light sources. *Appl. Phys. Lett.,* 71(5): 569-571

[8] Vainshtein, I. A., Zatsepin, A. F., & Kortov, V. S. (1999). Applicability of the empirical Varshni relation for the temperature dependence of the width of the band gap. *Phys. Solid State*, 41(6): 905-908

[9] Hill, T. L. (1986). An Introduction to Statistical Thermodynamics. New York: Dover

[10] Vurgaftman, I., & Meyer, J. R. (2003). Band parameters for nitrogen-containing semiconductors. *J. Appl. Phys.*, 94(6): 3675-3696

[11] Borri, P., Langbein, W., Hvam, J. M., & Martelli, F. (1999). Well-width dependence of exciton-phonon scattering in $In_xGa_{1-x}As$/GaAs single quantum wells. *Phys. Rev. B*, 59(3): 2215-2222

[12] Wang, H., Ji, Z., Qu, S., Wang, G., Jiang, Y., Liu, B., et al. (2012). Influence of excitation power and temperature on photoluminescence in InGaN/GaN multiple quantum wells. *Opt. Expr.*, 20(4): 3932-3940

[13] Zhang, X. T., Liu, Y. C., Zhi, Z. Z., Zhang, J. Y., Lu, Y. M., Shen, D. Z., & Kong, X. G. (2002). Temperature dependence of excitonic luminescence from nano -crystalline ZnO films. *J. Lumin.*, 99(2):149-154

[14] Renwick, P., Tang, H., Bai, J., & Wang, T. (2011). Reduced longitudinal optical phonon-exciton interaction in InGaN/GaN nanorod structures. *Appl. Phys. Lett.*, 100(18): 182105-182108

[15] Misra, P.K. (2010). *Chapter 2. Phonons and lattice vibration. Physics of Condensed Matter.* Waltham: Academic Press. pp. 44

[16] Morkoc, H. (2013). *Nitride Semiconductor Devices: Fundamentals and Applications.* New Jersey: John Wiley & Sons, pp, 124

[17] Gelmont, B. L., Shur, M., & Stroscio, M. (1995). Polar optical-phonon scattering in three and two dimensional electron gases. *J. Appl. Phys.*, 77(2): 657-660

[18] Schwabel, F. (2008). *Advanced Quantum Mechanics, 4th ed.*. New York: Springer, pp, 253

[19] Mahan, G.D. (2010). *Condensed Matter in a Nutshell.* Princeton: Princeton University Press, pp, 181

[20] Park, Y. S., Holmes, M. J., Shon, Y., Yoon, I. T., Im, H., & Taylor, R. A. (2011).

GaN nanorods grown on Si (111) substrates and exciton localization. *Nano. Res. Lett.*, 6(1):81-94

[21] Swe, N. T. C., Suraprapapich, S., & Wissawinthanon, C. (2008). Low Temperature Micro-PL Measurements of InAs Binary Quantum Dots on GaAs Substrate. *ECTI-EEC* 6(2):50-54

[22] Shan, W., Walukiewicz, W., Ager, J. W., et al. (2005). Nature of room-temperature photoluminescence in ZnO. *Appl. Phys. Lett.*, 86(19): 191911-191913

[23] Kumano, H., Yoshida, H., Tawara, T., & Suemune, I. (2002). Longitudinal -optical-phonon-assisted energy relaxation in self-assembled CdS quantum dots embedded in ZnSe. *J. Appl. Phys.*, 92(7): 3573-3578

[24] Huang, K., & Rhys, A. (1950). Theory of light absorption and non-radiative transitions in F-centres. *Proc. Roy. Soc. London. Series A. Math. Phys. Sci.*, 204(1078): 406-423

[25] Heitz, R., Mukhametzhanov, I., Stier, O., Madhukar, A., & Bimberg, D. (1999). Enhanced polar exciton-LO-phonon interaction in quantum dots. *Phys. Rev. Lett.*, 83(22): 4654-4657

[26] Tan, L. T., Martin, R. W., O'Donnell, K. P., & Watson, I. M. (2006). Photoluminescence and phonon satellites of single InGaN⁄GaN quantum wells with varying GaN cap thickness. *Appl. Phys. Lett.*. 89:101910-101912

[27] Pecharromán-Gallego, R., Edwards, P. R., Martin, R. W., & Watson, I. M. (2002). Investigations of phonon sidebands in InGaN/GaN multi-quantum well luminescence. *Mater. Sci. & Eng. B*, 93(1-3): 94-97

[28] Lee, K. B., Parbrook, P. J., Wang, T., Ranalli, F., Martin, T., Balmer, R. S., & Wallis, D. J. (2007). Optical investigation of exciton localization in $Al_xGa_{1-x}N$. *J.*

Appl. Phys., 101(5):053513-053515

[29] Chen, D., Luo, Y., Wang, L., Li, H., Xi, G., Jiang, Y., & Han, Y. (2007). Enhancement of electron-longitudinal optical phonon coupling in highly strained InGaN/GaN quantum well structures. *J. Appl. Phys.*101(5): 053712-053716

[30] Kioupakis, E., Rinke, P., Delaney, K. T., & Van de Walle, C. G. (2011). Indirect Auger recombination as a cause of efficiency droop in nitride light-emitting diodes. *Appl. Phys. Lett.*, 98(16):161107-161109

[31] Shi, J. J. (2003). Interface optical-phonon modes and electron–interface-phonon interactions in wurtzite GaN/AlN quantum wells. *Phys. Rev. B*, 68(16): 165335-165344

[32] Li, L., Liu, D., & Shi, J. J. (2005). Electron quasi-confined-optical-phonon interactions in wurtzite GaN/AlN quantum wells. *Eur. Phys. J. B,* 44(4): 401-413

4. Study of surface plasmon on InGaN/ GaN quantum well structures

This chapter studies the influence of exciton delocalization on surface plasmon coupling effects in an InGaN/GaN quantum well structure by means of temperature dependent PL measurement. It has been found that the surface plasmon coupling effect becomes prominent during the temperature range of 100K-200K where the excitonic delocalization plays an important role. The internal quantum efficiency (IQE) of InGaN/GaN quantum wells also shows significant enhancement as a result of the surface plasmon coupling.

In Section 4.1, the exciton-surface plasmon coupling has been explained and the current study on surface plasmon coupling has been reviewed, enabling a good understanding of the complicated coupling mechanism. It hence suggests that it is necessary to investigate on the relationship between excitonic delocalization and surface plasmon coupling. In Section 4.2, the temperature dependent PL measurement results demonstrate stronger PL enhancement due to Ag coating in the temperature range where excitonic delocalization takes place. The has been investigated based on the dipole-dipole coupling model.

4.1. The exciton-surface plasmon coupling effect for InGaN QWs

4.1.1 Exciton-Surface plasmon coupling

The mechanism of exciton-surface plasmon (SP) polariton coupling lays the foundation of the surface plasmon LEDs[1]. This coupling effect essentially involves several systems, namely, excitons, surface plasmons and the light. An exciton[2] is an

electrically neutral quasiparticle that consists of a pair of electron and hole. In its own system, it could either recombine in a radiative way by giving out a photon, or in a non-radiative way by dissipating the energy via phonons, referred as the radiative and non-radiative recombination respectively.

When excitons couple to the surface plasmon mode, it is still nonradiative. However, a surface plasmon mode would further couple with a light mode, and coupling between surface plasmons and photons is named as surface plasmon polariton[3]. Only when converted to the light mode does the surface plasmon becomes radiative[4].

The principle of surface plasmon coupling could be investigated using the Fermi's Golden Rule[5]:

$$\lambda_{if} = \frac{2\pi}{\hbar}\left|M_{if}\right|^2 \rho_f \tag{4.1}$$

Where λ_{if} is the transition probability, $|M_{if}|$ is the matrix element for the interaction, and ρ_f is the density of final states. *i* and *f* refers to the initial and final state in the transition process, respectively. Fermi's Golden rule suggests the transition probability is proportional to the density of unoccupied final states. At the surface plasmon energy, the dispersion curve is almost flat indicating an extremely high density of states at the surface plasmon energy. Consequently, the transition probability to the surface plasmon mode can be quite high[6,7,8].

The effect on the emission efficiency through exciton-surface plasmon coupling can be further researched from another important concept, the Purcell effect. The Purcell factor is the ratio of the density of states (DOS) of light in the cavity to the DOS in the free space[9,10]. It describes the enhancement of spontaneous emission rate under the environment of a resonant cavity because the optical density of states is strongly enhanced as a result of the cavity. The Purcell factor F_p can be estimated by the decay time measured on the as-grown sample (τ_1) and the decay time for the

Ag-coated sample (τ_0) , and it satisfies: $F_p = 1 + \tau_0/\tau_1$.

Normally, without metal coating, the internal quantum efficiency (η_{IQE}) can be calculated by: $\eta_{IQE} = \frac{\beta_{rad}}{\beta_{rad} + \beta_{nrad}}$, where β_{rad} and β_{nrad} are the radiative recombination rate and non-radiative recombination rate respectively. When there is a surface plasmon polariton involved due to a metal coating on top of the capping layer, the equation for η_{IQE} becomes[11]:

$$\eta_{IQE} = \frac{F_P \beta_{rad}}{F_P \beta_{rad} + \beta_{nrad}} \tag{4.2}$$

It is important to note that the term of $F_p\beta_{rad}$ is the sum of surface plasmon modes which are non-radiative and the radiative part of excitons. Therefore, in many cases, even if the η_{IQE} is much enhanced due to the Purcell effect, the light emission is instead reduced because of the dissipation of surface plasmon modes from the smooth metal surface. If the surface plasmon mode cannot transfer to a light mode, then the external emission efficiency could be reduced. When the metal surface is made rough by various methods, there is a higher possibility for surface plasmon modes to transfer to light modes and become radiative. This then enhances the external efficiency of light emission.

In addition, it is useful to note that the Purcell factor can vary according to the thickness of the capping layer on top of the quantum well. When the distance between the metal layer and the quantum well gets larger than 80nm, the coupling effect can be impaired[5].

The mechanism of exciton-surface plasmon polariton coupling is illustrated in Figure 4.1, There are both radiative and non-radiative parts in the exciton mode, and the same goes for the surface plasmon mode. The surface plasmon mode is essentially nonradiative when dissipating through the metal in the form of heat, and it becomes radiative when it converts to the light mode.

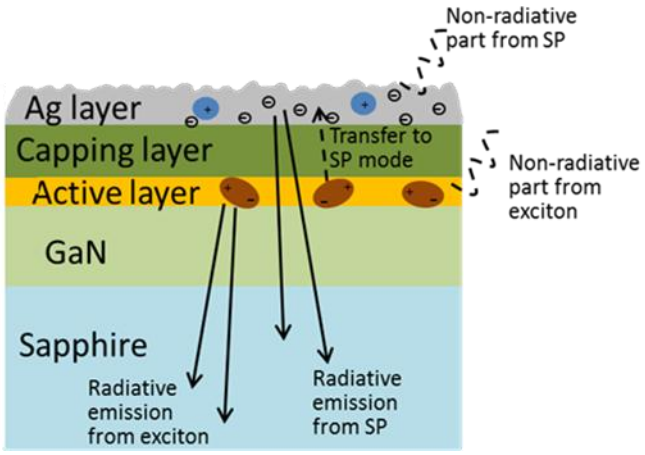

Figure 4.1 Schematic diagram of the Ag-coated InGaN/GaN Structure. Radiative and nonradiative emission in both exciton mode and surface plasmon mode have been noted.

4.1.2 Current status of surface plasmon enhanced InGaN LEDs

InGaN light-emitting-diodes (LEDs) have been researched and developed since the 1990s, and the internal quantum efficiency (IQE) has always been a concern for InGaN LEDs. The mechanism of exciton-surface plasmon coupling has been applied to InGaN LEDs in order for the surface plasmon mode to enhance the spontaneous emission rate inside the InGaN quantum structures. The issue of SP-enhanced InGaN LEDs is most commonly researched by time-resolved photoluminescence (TRPL) [5]. It is also analyzed by temperature dependent photoluminescence (PL)[12] and electroluminescence (EL)[13].

The SP coupling effect for different metasl has been widely researched. A film of Ag, Au or Al at thickness of 50nm has been deposited on the single InGaN QWs with a GaN spacer /capping layer of 10nm[14]. It was found that at the original emission peak of 460nm for InGaN QW, there is 14-fold enhancement in the Ag-coated sample and 6.8-fold enhancement in the Al-coated sample, while no significant enhancement can be observed in the Au-coated sample. The PL enhancement ratio corresponding to different wavelengths is most strong at 440nm, 420nm and 535nm for the Ag-coated sample, Pt-coated sample and Au-coated sample, respectively. These wavelengths correspond to the surface plasmon energy for each metal

obtained from its dispersion curve and this demonstrates the possibility of enhancing the emission in the ultraviolent region or the green regions by these metals[15,16,17]. It's difficult for a pure Au film to enhance the PL intensity, but a combination of Au(6nm)/ Ag(14nm) [15] or a good condition of Au annealing [16] has a good effect.

The factor of capping layer thickness affects the exciton-SP coupling. The PL enhancement ratio at the InGaN QW emission peak drops when the thickness of the GaN capping layer increases, because exciton-SP polariton coupling gets weaker when the distance between exciton and SP increases [5]. An impressive 25-fold enhancement of PL intensity has been observed on the InGaN single QW (SQW)[18]. This is because the original light emission of as-grown SQW is very weak, and the GaN capping layer above the QW is only 5nm thick. Besides, other factors such as the Ag film thickness, grating size or annealing condition have been reported to affect the SP enhancement effect [14,18].

Electroluminescence (EL) has been used to measure the SP-enhanced LED devices. This is a recent advancement, as it has been a problem for SP in the Ag film to couple to excitons in the QW with a thick *p*-GaN layer and the bonding. One innovation is to make a grid pattern on top of a 60nm-thick *p*-GaN layer, and deposit the Ag film inside the grid squares that are separated by the grid metal[13]. The I-V properties measured with electroluminescence suggests that the Ag-coated LED has 80% enhancement of EL intensity compared to the uncoated sample at the current of 200mA. Another feasible method is to fabricate metal protrusions into *p*-GaN[19].The *p*-GaN layer is made into the nano-hole pattern, with the diameter of each nano hole as 100nm. A schematic diagram is provided in Figure 4.2. Ag penetrates into the nano-holes of the p-GaN layer. The bottom of these nano-holes inside the p-GaN layer is less than 100nm apart from the QW, which still allows for the coupling between Ag and QW. The EL intensity is found to be 74% stronger in the SP LED than in the normal LED.

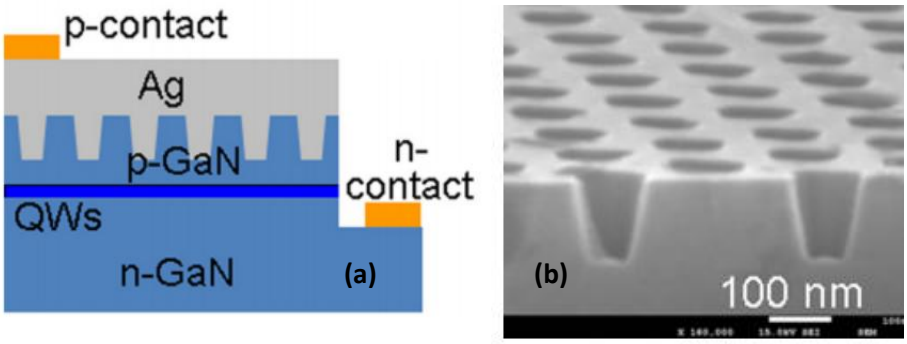

Figure 4.2 (a) Schematic diagram of the LED structure with Ag protrusions in the p-GaN layer. (b) An SEM image of the hole pattern [19]

While EL can be used for measuring the external quantum efficiency (EQE) from the I-V curve and the input power, PL measurements cannot measure EQE because CCD only captures the light radiation at one certain angle and cannot measure the light output power. However, the enhancement of PL intensity between the Ag-coated sample and the uncoated sample can be used to estimate the SP enhancement effect on EQE.

Generally, to estimate the internal quantum efficiency (IQE), a commonly used method is through temperature dependent PL measurements. At absolute zero temperature, IQE is assumed to be 100%, and as temperature rises, the PL intensity quickly decays. The ratio of PL intensity at room temperature to that at absolute zero temperature is regarded as IQE of the sample. The PL intensity of Ag-coated sample is found to decay more slowly with increasing temperature than an as grown sample. More than a 6-fold enhancement of IQE is observed for an Ag-coated single QW [12]. In that research, a 14-fold enhancement of PL intensity has been found for Ag-coated sample which roughly suggests a 14-fold enhancement of EQE. While 6-fold enhancement of PL intensity is owed to the enhancement by IQE, the remaining factor of 2 times of enhancement is owed to the light extraction, due to the rough surface of Ag facilitating light extraction from the surface plasmon mode.

The research of temperature dependent properties of SP coupling in InGaN QWs has been less studied. At low temperature, the uncoated and Ag-coated samples are

found to decay with power intensity at a similar rate, so the PL intensity enhancement ratio is not prominent. However, as temperature rises, the PL intensity in Ag-coated sample decays more slowly than that for the uncoated sample. Hence the enhancement effect is found to be stronger at higher temperature [12,20]. This phenomenon is believed to relate to the exciton delocalization effect inside the QW.

However, the relationship between exciton-SP coupling and the exciton delocalization process has only been mentioned and has not been studied in detail. More research is required to probe this relationship. This helps to gain a better understanding of the dynamic temperature dependent mechanism of exciton-SP polariton coupling in InGaN QW LEDs.

4.2. Study of the relationship between exciton-surface plasmon coupling and exciton delocalization in InGaN QWs

4.2.1 Influence of exciton delocalization on exciton-surface plasmon coupling

The study is performed on an InGaN/GaN quantum well sample and one sample with a 20nm-thick silver coating on the same wafer structure. The schematic diagram of the Ag coated sample is provided in Figure 4.2.a. The InGaN quantum well (QW) structure consists of two periods of InGaN/GaN QWs, where the InGaN well thickness is 2.5nm and the GaN barrier thickness is 8.7nm, and the In composition is around 18%. The InGaN/GaN QWs are grown on the GaN layer (1μm), which is above the 500nm AlN nucleation layer and the sapphire. Ag is then deposited onto the surface using a thermal evaporator. The thickness of the silver is controlled to be 20nm. The AFM images of the as-grown sample surface and the Ag-coated surface are provided in Figure 4.3.b and 4.3.c.

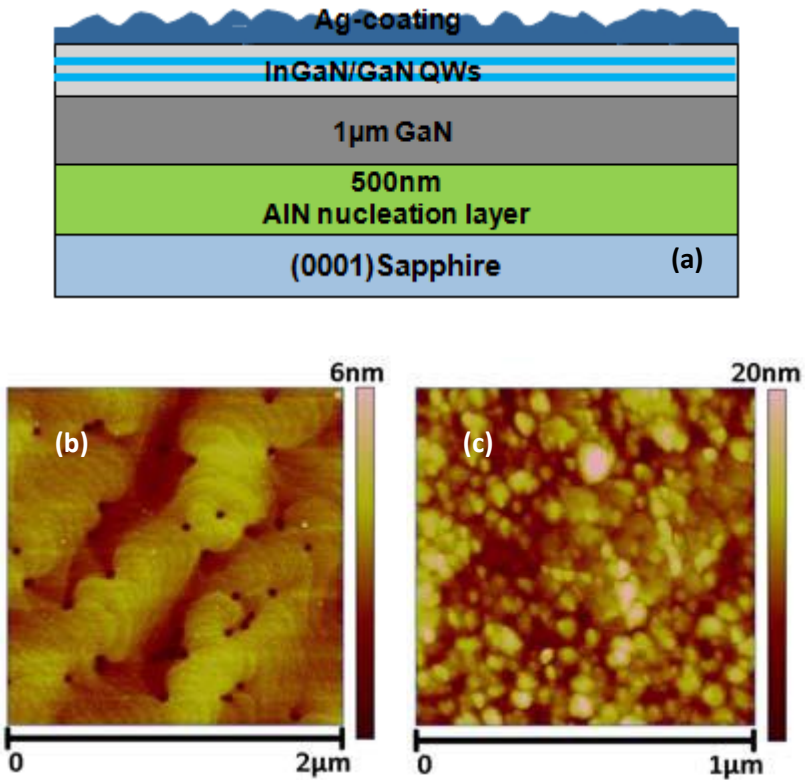

Figure 4.3 (a)Schematic diagram for the structure of Ag-coated InGaN/GaN QW sample; The AFM image of (a) the as-grown sample surface and (b) the surface of the Ag-coated sample

Temperature dependent photoluminescence (PL) has been carried out on the pair of samples. A 375nm diode laser was used with the laser power of 18mW as an excitation source. The laser beam size has been measured using a commercial beam profiler [18], which is around 125μm in radius. The PL spectrum is collected by a 0.5 m SPEX 500 monochromator and a CCD detector.

Figure 4.4.a and b show the spectra measured from 10K to 300K for the as-grown sample and the silver-coated sample respectively. Note that in the temperature range of between 10K and 100K, an interval of temperature is set as 10K; and between 100K and 300K, the interval is set as 20K. Both samples demonstrate the S-curve of the emission wavelength with increasing temperature, which indicates the existence of excitonic delocalization.

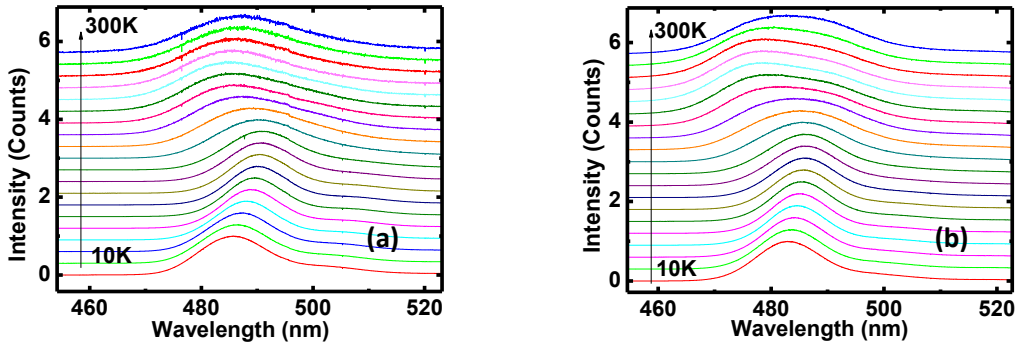

Figure 4.4 Temperature dependent PL measurements for (a) the as-grown sample and (b) the Ag-coated (20nm) sample

The emission energy as a function of temperature for both samples is then plotted in Figure 4.5.a. Figure 4.5.b plots the enhancement ratio of the integrated PL intensity between the Ag-coated sample and the as grown sample. Both samples are measured under identical conditions. As has been mentioned, the ratio of the integrated PL intensity at room temperature to that at absolute zero temperature is regarded as the IQE of the sample. The PL intensity enhancement ratio then suggests that the PL intensity in the Ag-coated sample decays more slowly with increasing temperature, and the enhancement ratio at room temperature is regarded as the enhancement of IQE in the Ag-coated sample comparing with the as-grown sample. Based on this method, the IQE is 5.1% for the as-grown sample and 28.0% for the Ag-coated sample. There is a 5.5-fold enhancement of the IQE due to the Ag coating.

From Figure 4.5.a, both samples demonstrate a clear S-shape of the emission peaks, indicating strong exciton localization. The blue shift for the Ag-coated sample is even more severe than in the as-grown sample. In Chapter 3, the parameter σ has been used as an index of the exciton delocalization effect and can be obtained by fitting the S-curve based on Equation (3.1)[21]. However, in existence of the Ag-coating, the S-curve cannot be fitted by the standard model described in Equation (3.1). A stronger blue-shift could be due to factors arising from surface plasmon coupling instead of a stronger delocalization effect in excitons. Considering

exciton delocalization is an intrinsic feature for InGaN materials, it should not be changed by Ag-coating. In fact, the surface plasmon wavelength for Ag is around 440nm [6] which is lower than the emission wavelength of the as-grown sample. Therefore, when there exists a strong surface-plasmon coupling effect, the emission spectrum is more strongly enhanced at the surface plasmon wavelength, and hence a blue shift of the emission wavelength is exhibited.

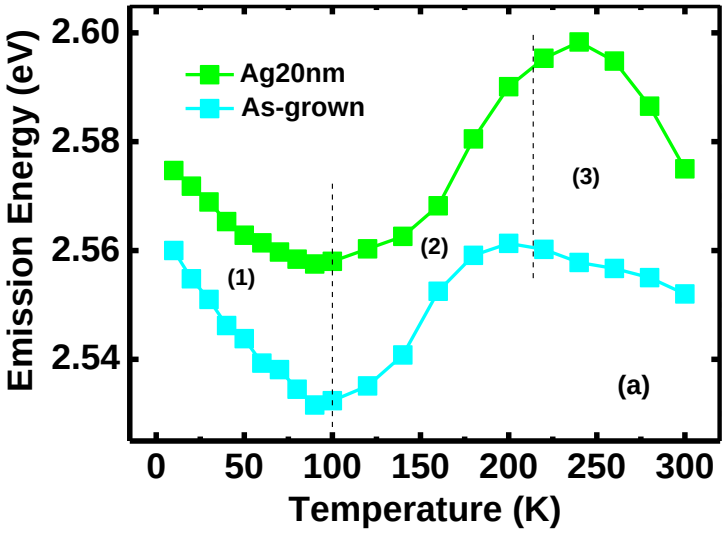

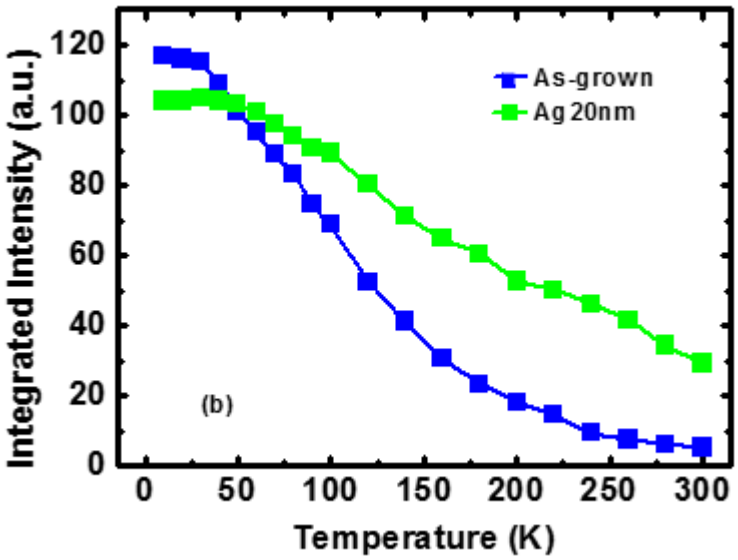

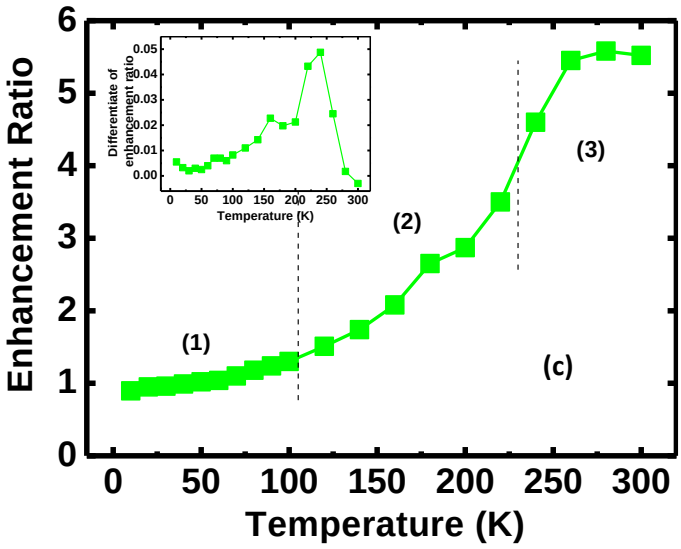

Figure 4.5 (a) Emission energy as a function of temperature for the as-grown sample and the Ag-coated sample. (b) The integrated PL emission power intensity for as-grown and Ag-coated sample as a function of temperature. (c) Enhancement ratio of the integrated PL intensity as a function of temperature. Inset of (b) shows the differential of the enhancement ratio

Since a number of emission mechanisms are involved for different temperatures, the whole temperature range could be divided into three ranges according to the shape of the S-curve, with range (1) from 10K to 90K, range (2) from 90K to 220K and range (3) from 220K to 300K. The temperature ranges have been marked in Figure 4.5.a and Figure 4.5.c.

In the temperature range (1), the red shift in both S-curves in Figure 4.5.a is attributed to the thermal expansion and carrier hopping[22]. Note that the enhancement ratio shown in Figure 4.5.c in this temperature range remains below 1.5. The PL intensity enhancement due to exciton-surface plasmon coupling is not significant during this temperature range.

When temperature goes up to 90K-100K, a clear blue-shift owing to the exciton delocalization effect starts to dominate[22]. The delocalization process generally starts to take place at 90-100K. Correspondingly, the enhancement ratio of the PL intensity dramatically increases, from 1.4 at 90K up to around 5.0 at 240K. Normally, as temperature rises, the PL intensity for the as-grown sample drops greatly as a

result of the enhancement of non-radiative recombination. The fast increasing rate of the PL enhancement ratio in Figure 4.5.c indicates that, the Ag coating effectively reduces the PL intensity drop rate through coupling the exciton to the surface plasmon mode. This suggests that, when excitons are localized at low temperatures, the exciton-SP coupling is not effective. It also shows that the exciton delocalization process leads to an enhancement in the exciton-SP coupling.

In temperature range (3), the delocalization process becomes saturated when all delocalized excitons have been actived. Therefore, the thermal expansion effect is dominant and the red-shift of emission energy appears. At this temperature range, the large number of free excitons gain momentum when temperature rises. Corresponding to the change in the emission energy, the PL intensity ratio enhances in a much slower rate.

In addition, the effect of Ag layer thickness on the performance of exciton delocalization is analyzed. Three samples were prepared with different Ag coating layer thickness: 20nm in sample A, 50nm in sample B and 100nm in sample C. The three samples as well as the as-grown sample are from the same wafer and have identical QW structures. Prior to Ag-coating, the PL of all the samples have been measured, demonstrating a good uniformity in the emission energy and the PL intensity. This excludes the factor of sample non-uniformity for later analysis of experiment results.

Similarly, the temperature dependent PL measurements have been conducted for the three Ag-coated samples and the as-grown sample. Figure 4.6 plots the emission energy and the PL intensity enhancement ratio as a function of temperature. The S-curves of the emission energy and the curves of the PL intensity enhancement ratio for the three Ag-coated samples all demonstrate a similar trend with the Ag-coated sample in the first experiment: the PL intensity enhancement ratio increases at a highest rate in the temperature range (2) where the exciton

delocalization process is strong.

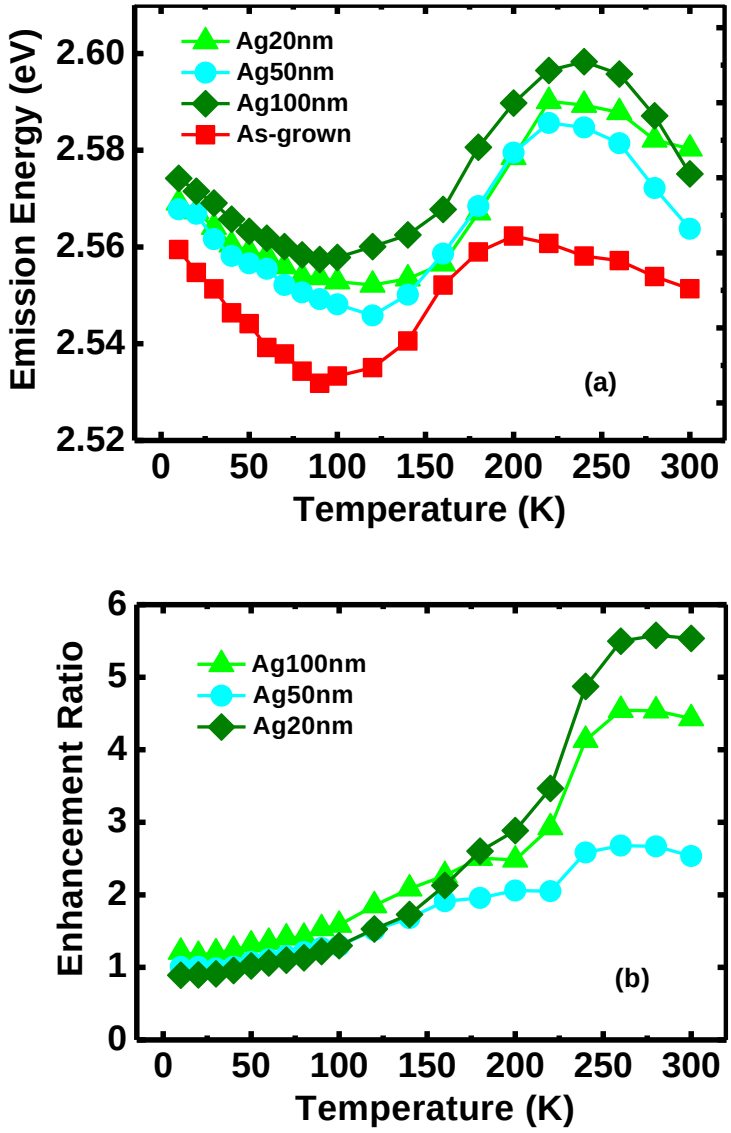

Figure. 4.6 (a)The emission energy and (b) the PL intensity enhancement ratio as a function of temperature for the as-grown sample and the three Ag-coated samples of different Ag layer thickness.

The three Ag-coated samples prove that the surface plasmon coupling effect is influenced by the exciton delocalization process, and the result is consistent with the first experiment. There might be other reasons for the shape of the PL intensity enhancement ratio as a function of temperature, and a most reasonable explanation is still the influence of the exciton delocalization effect on the exciton-SP coupling which then affects the light emission intensity.

4.2.2 Study of the influence of exciton delocalization on exciton-surface plasmon coupling

The exciton in the QW and the surface plasmon are essentially two systems of dipoles. A short distance between the QW layer and the Ag layer is required to ensure an effective dipole-dipole coupling process. For the dipoles in two planar (2D) films, the dipole-dipole coupling rate v obeys a following relationship that concerns the in-plane wave number k and the distance between the two films d [23], as provided in Equation (4.3):

$$v \propto k \exp(-kd) \tag{4.3}$$

Clearly the dipole-dipole coupling rate v exponentially decays with d, the distance between the two films, according to Equation (4.3). On the other hand, the coupling rate has a more complicated relationship with the in-plane wave number k, which indicates the momentum of dipoles. When $k \to 0$, $v \propto k$, i.e. the coupling rate proportionally increases with the in-plane wave number. When $k \to \infty$, the coupling rate exponentially decays as the in-plane wave number increases, $v \propto \exp(-k)$. Therefore, the coupling rate v is non-monotonic as a function of k and it has a maximum value v_{max}. Taking the first derivative of the function $v(k)$ over k, i.e., $dv(k)/dk = (1-kd)\exp(-kd)$, the maximum value of $v(k)$ can be obtained by making $dv(k)/dk$ equal to *zero*. Hence $kd = 1$ is a condition for the highest dipole-dipole coupling rate (v_{max}) between the two planar films. In the Ag-coated samples in this study, the GaN capping layer above the InGaN QW is 10nm, so the dipole-dipole planar distance d is regarded as 10nm. To make $kd=1$ when d =10nm, the optimized in-plane wave number k should have a value of 0.1 nm^{-1}.

Figure 4.7 plots the dipole-dipole coupling rate v as a function of k, when the distance d is fixed at 10nm. From Figure 4.7, the increasing rate of the coupling rate at a lower k is much stronger than the decreasing rate at a higher k. This suggests

that the coupling rate increases strongly with k and would maintain at a high rate. The range of the in-plane wave number corresponding to more than 60% of the highest dipole-dipole coupling rate (v_{max}) is between 0.03nm^{-1} and 0.23nm^{-1}. The coupling rate drops below 30% of v_{max} when k is 0.3nm^{-1}. It further drops below 20% of v_{max} when k is 0.34nm^{-1} and below 10% of v_{max} when k is above 0.4nm^{-1}. In SP-exciton coupling, the wave number of the excitons would match that of the surface plasmon in order to realize the coupling process. Figure 4.7 has suggested a certain range of the wave number for excitons and SP in which a high exciton-SP coupling rate could be realized.

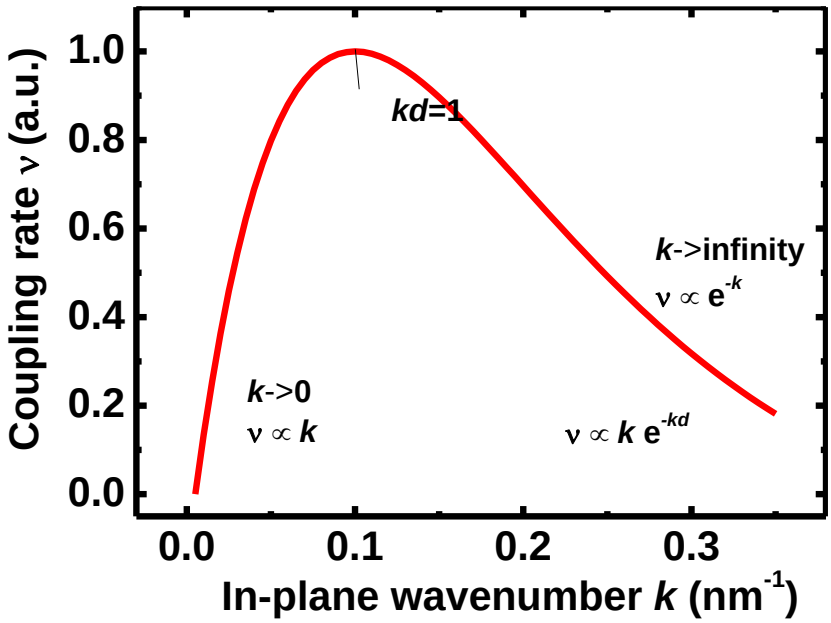

Figure 4.7 The dipole-dipole coupling rate *v* as a function of the in-plane wave number *k* when the dipole-dipole planar distance *d* is fixed at 10nm.

The wave number of a surface plasmon is now calculated. For the light at 480nm, considering the refractive index for InGaN as 2.4, the light wave number is around 0.031nm^{-1} ($k=2\pi n/\lambda$). A reasonable value for the wave number of the surface plasmon mode (k_{SP}) is 3-4 times (or higher) of the value for the light mode[20]. The value for k_{SP} is around 0.1nm^{-1}, which is also the wave number for a maximum coupling rate. Therefore, the wave number for the surface plasmon is very favorable for the exciton-SP coupling as suggested in Figure 4.7.

On the other hand, the localized excitons and delocalized (free) excitons have different performances in exciton-SP coupling due to their features of the wave function in k-space, as illustrated in Figure 4.8. The conditions of the localized excitons and the delocalized excitons on the potential surface in the real space has also been illustrated. The localized excitons are trapped in the potential surface minima and have zero momentum on average, while the delocalized excitons can easily gain the momentum which corresponds to the wave number in the k-space.

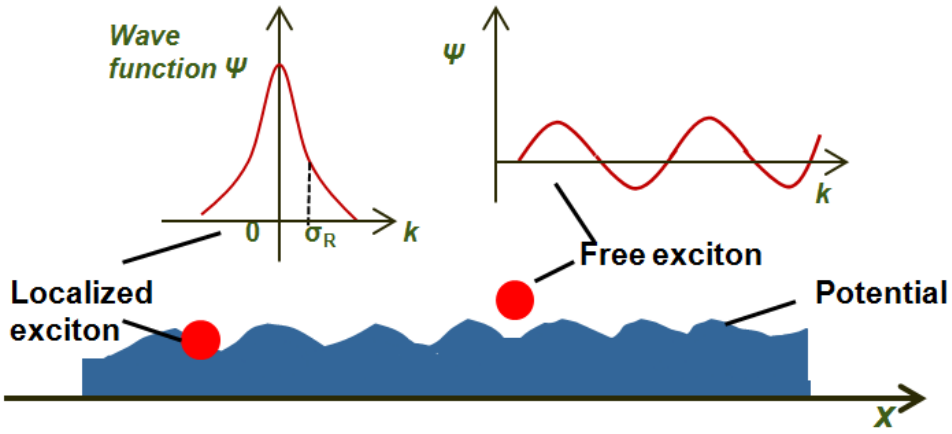

Figure 4.8 Schematic diagram of the k-space profile for localized excitons and free excitons

For the localized excitons in the InGaN QW with two periods of QWs and an indium composition of around 12%, the localization length for InGaN can be estimated as 2nm[24]. Assuming one electron or hole is trapped in the localized state of around 2nm in width, then its wave-function in real space is in the Gaussian distribution with the standard deviation of 1nm (2σ=2nm). The standard expression for the Gaussian distribution in the real space is: $U(x)=\frac{1}{\sigma\sqrt{2\pi}}e^{-\frac{x^2}{2\sigma^2}}$. The corresponding wave function in the reciprocal space (k-space) also follows a Gaussian distribution[20,25]. Through the standard Fourier transform process, there is:

$$F_x[e^{-\frac{1}{2\sigma^2}x^2}](k)=\int_{-\infty}^{\infty}e^{-\frac{1}{2\sigma^2}x^2}e^{-2\pi ikx}dx=\sqrt{2\pi\sigma^2}e^{-\pi^2 2\sigma^2 k^2}=\sqrt{2\pi\sigma^2}e^{-\frac{k^2}{2\sigma_R^2}}, \quad (4.4)$$

where σ_R is the standard deviation of the Gaussian distribution in the reciprocal space, and it is related to σ in the real space: $\sigma_R = (2\pi\sigma)^{-1}$. In this scenario, σ_R in k-space is around 0.16nm^{-1}. The mean value of distribution in k space is 0 nm^{-1}. σ_R has been marked in Figure 4.7. In normal distribution, the probability for the wave number to be larger than 0.1nm^{-1} ($0.63\sigma_R$) is only 26%[26]. Therefore, it is difficult for the localized excitons to reach the wave number for SP (0.1nm^{-1}) and hence the exciton-SP coupling rate is low at the low temperatures when most excitons are localized.

For the delocalized (free) excitons, they gain momentum ($\hbar k$) and the kinetic energy ($\hbar^2 k^2 / 2m$). The kinetic energy comes from the thermalization at a certain temperature. According to the equipartition theorem[27], the thermal energy in one dimension of freedom is $K_BT/2$, so the thermal energy for one free electron or hole in the 2-dimensional QW is K_BT, where K_B is the Boltzmann constant and T is the temperature. The equation for the kinetic energy of the electrons is:

$$K_B T = \hbar^2 k^2 / 2m_e^*, \tag{4.5}$$

Where m_e^* is the effective mass of the electron and k is the wave number. Since the InGaN QW in this study has an Indium composition of 0.15, its value for m_e is $0.182m_0$ (m_0=9.1*10^{-31}kg) obtained from the linear interpolation of the effective mass for GaN and InN[28].

Based on Equation (4.5), the wave number of the delocalized electrons and holes at any temperature can be calculated. For instance, when exciton delocalization starts to takes place at 90K (T=90K), the wave number k for the electron is around 0.18nm^{-1} and k for the holes is even higher, suggesting that the delocalized excitons can easily gain adequate momentum. At this temperature, the dipole-dipole coupling rate v is more than 70% of the maximum coupling rate (v_{max}), as plotted in Figure 4.7 or calculated based on Equation (4.3). Therefore, when the delocalization

initially occurs at around 90K, the dipole-dipole coupling rate is considerably high. In the meantime, the number of free excitons is small. As temperature rises, even though the dipole-dipole coupling rate is dropping slightly, it is compensated by the significantly enhanced quantity of delocalized excitons and the overall effect of exciton-SP coupling is improving.

A turning point occurs at a temperature of around 240K. The delocalization process gets complete, and a drop of the dipole-dipole coupling rate cannot be compensated by further increase of the number of free excitons. During the temperature range of 240K-280K, the wave number k is around 0.3-0.35nm^{-1}, which corresponds to a dipole-dipole coupling rate at only 20% of its maximum value (v_{max}). Consequently, at a high temperature range 240K, the exciton-SP coupling effect cannot further improve and the PL enhancement ratio does not rise strongly as temperature further increases.

4.3. Summary

In summary, exciton-surface plasmon polariton coupling is a complicated process that involves the metal, photon and semiconductor which has abundant excitons. Knowing all the relevant concepts helps to understand the essence of dipole-dipole coupling between the surface plasmon system and the exciton system. By extensively reviewing the previous research on SP-exciton coupling on semiconductors, especially GaN based materials, it is found that the influence of exciton delocalization on exciton-SP coupling has not been deeply studied.

This research suggests stronger PL enhancement at the intermediate temperature range (100K-200K) where the exciton delocalization process is prominent. It is found that exciton delocalization enables the free excitons to find the momentum which easily matches the momentum in SP mode, thus increasing the extent of surface plasmon coupling. However, when temperature continues to rise, the free

excitons gain far more momentum which corresponds to a much higher wavenumber than $0.1nm^{-1}$. In this scenario, the coupling rate drops to a value as low as 20% of its maximum value when the wave number further increases. This explains why the PL intensity enhancement ratio has a much slower rate of increase at high temperature. In a SP coupled system, exciton delocalization is a positive factor for IQE by promoting the stronger exciton-SP coupling effect.

Reference

[1] Kwon, M. K., Kim, J. Y., Kim, B. H., Park, I. K., Cho, C. Y., Byeon, C. C., & Park, S. J. (2008). Surface-Plasmon-Enhanced Light-Emitting Diodes. *Adv. Mater.*, 20(7): 1253-1257

[2] Liang, W Y (1970). Excitons. *Physics Education.* 5 (4): 226-231

[3] Barnes, W. L., Dereux, A., & Ebbesen, T. W. (2003). Surface plasmon sub-wavelength optics. *Nature*, 424(6950): 824-830

[4] Heinz, R. (1988). *Surface Plasmons on Smooth and Rough Surfaces and on Gratings*. Springer Tracts in Modern Physics **111**. New York: Springer-Verlag.

[5] Neogi, A., Lee, C. W., Everitt, H. O., Kuroda, T., Tackeuchi, A., & Yablonovitch, E. (2002). Enhancement of spontaneous recombination rate in a quantum well by resonant surface plasmon coupling. *Phys. Rev. B.*, 66(15):153305-153308

[6] Crawford, M. H., Fischer, A. J., Koleske, D. D., et al. (2009) Final LDRD Report: Nanoengineering for Solid-State Lighting

[7] Bittencourt, J. A. (2004). *Fundamentals of Plasma Physics*. Springer.

[8] Ritchie, R. H. (June 1957). Plasma Losses by Fast Electrons in Thin Films. *Phys.*

Rev.,106 (5): 874–881

[9] Purcell, E. M. (1946). Spontaneous emission probabilities at radio frequencies. *Phys. Rev*., 69: 681-681

[10] Haroche, S. & Kleppner, D. (1989). Cavity Quantum Dynamics. *Physics Today*. 1:24–30

[11] Wiesmann, C., Linder, N., & Schwarz, U. T. (2008, May). Efficiency of InGaN LEDs Incorporating Surface Plasmon Polaritons. In *Lasers and Electro-Optics, 2008 and 2008 Conference on Quantum Electronics and Laser Science. CLEO/QELS 2008. Conference on* (pp. 1-2). IET.

[12] Okamoto, K., Niki, I., Scherer, A., Narukawa, Y., Mukai, T., & Kawakami, Y. (2005). Surface plasmon enhanced spontaneous emission rate of InGaN⁄ GaN quantum wells probed by time-resolved photoluminescence spectroscopy. *Appl. Phys. Lett.*, 87(07): 071102-071104

[13] Lu, C. F., Liao, C. H., Chen, C. Y., Hsieh, C., Kiang, Y. W., & Yang, C. C. (2010). Reduction in the efficiency droop effect of a light-emitting diode through surface plasmon coupling. *Appl. Phys. Lett.*, 96(26): 261104-261106

[14] Okamoto, K., Niki, I., Shvartser, A., Narukawa, Y., Mukai, T., & Scherer, A. (2004). Surface-plasmon-enhanced light emitters based on InGaN quantum wells. *Nat. Mater.*, 3(9): 601-605

[15] Cho, C. Y., Lee, S. J., Song, J. H., Hong, S. H., Lee, S. M., Cho, Y. H., & Park, S. J. (2011). Enhanced optical output power of green light-emitting diodes by surface plasmon of gold nanoparticles. *Appl. Phys. Lett.*, 98(5): 051106-051108

[16] Zhao, H., Zhang, J., Liu, G., & Tansu, N. (2011). Surface plasmon dispersion

engineering via double-metallic Au/Ag layers for III-nitride based light-emitting diodes. *Appl. Phys. Lett.*, 98(15): 151115-151117

[17] Oh, T. S., Jeong, H., Lee, Y. S., Kim, J. D., Seo, T. H., Kim, H., ... & Suh, E. K. (2009). Coupling of InGaN/GaN multiquantum-wells photoluminescence to surface plasmons in platinum nanocluster. *Appl. Phys. Lett*., 95(11): 111112-111114

[18] Renwick, P., Tang, H., Wang, Q., Smith, R., & Wang, T. (2011). Enhanced internal quantum efficiency of an InGaN/GaN quantum well as a function of silver thickness due to surface plasmon coupling. *physica status solidi (c)*, *8*(7-8): 2176-2178

[19] Chen, H. S., Chen, C. F., Kuo, Y., Chou, W. H., Shen, C. H., Jung, Y. L & Yang, C. C. (2013). Surface plasmon coupled light-emitting diode with metal protrusions into p-GaN. *Appl. Phys. Lett.*, 102(4): 041108-041110

[20] Lu, Y. C., Chen, C. Y., Yeh, D. M., Huang, C. F., Tang, T. Y., Huang, J. J., & Yang, C. C. (2007). Temperature dependence of the surface plasmon coupling with an InGaN/GaN quantum well. *Appl. Phys. Let*.,90(19):193103-193105

[21] Eliseev, P. G., Perlin, P., Lee, J., & Osinski, M. (1997). "Blue" temperature -induced shift and band-tail emission in InGaN-based light sources. *Appl. Phys. Lett.*, 71(5): 569-571

[22] Lee, K.B. (2009). *Fabrication and Characterisation of AlGaN based Ultraviolet Light Emitting Diodes.* PhD thesis, University of Sheffield

[23] Rindermann, J. J., Pozina, G., Monemar, B., Hultman, L., Amano, H., & Lagoudakis, P. G. (2011). Dependence of resonance energy transfer on exciton dimensionality. *Phys. Rev. Lett.*, 107(23): 236805-236809

[24] Graham, D. M., Vala, A. S., Dawson, P., Godfrey, M. J., Kappers, M. J., Smeeton, T. M., & Thrush, E. J. (2003). Exciton localization in InGaN/GaN single quantum well structures. *Phys. Status Solidi B*, 240(2): 344-347

[25] Bracewell, R. (1999). *The Fourier Transform and Its Applications, 3rd ed.* New York: McGraw-Hill, pp. 98-101

[26] Normal distribution Z table. Retrieved from: http://ramsey1.chem.uic.edu/tak/chem52411/notes11/notes11_11.pdf, since July, 2013

[27] Huang, K (1987). *Statistical Mechanics (2nd ed.).*New York: John Wiley and Sons. pp. 136–138

[28] Vurgaftman, I., & Meyer, J. R. (2003). Band parameters for nitrogen-containing semiconductors. *J. Appl. Phys.*, 94(6): 3675-3696

5. Theoretical study of InGaN-based whispering gallery mode (WGM) ring cavities

This chapter studies InGaN-based whispering gallery mode ring cavities in order to obtain high quality factors in the visible spectrum. The whole simulation work is carried out using the Finite Difference Time Domain (FDTD) software MEEP under the Linux system. The mode splitting effect is analyzed which suggests that a proper design using a pair of identical rings can generate a Q-factor which is 2-3 times higher than using a single ring cavity. The investigation also indicates that a slight alternation in size generates a mode anticrossing effect, leading to the degradation in quality factors.

In Section 5.1, the principles of the FDTD approach and the MEEP software are briefly introduced. This section also presents the calculated results on a single ring cavity. Section 5.2 shows the study of the mode splitting effect, which includes two parts, namely, how the mode splitting (separation) energy varies in different scenarios and how the quality factor is affected due to mode splitting. The effect on Q-factor for identical rings and rings of different sizes has been analyzed.

5.1. Study of a single whispering gallery mode cavity

5.1.1 The Finite Difference Time Domain (FDTD) approach

The FDTD method is to solve the Maxwell's equations numerically. The time-dependent Maxwell's equations are discretized to the space and time partial derivatives, and are then solved in the following manner: the electric field components in some space grid are solved in one time slot, and then the magnetic

field components in the space grid are solved in the other time slot[1]. The process repeats until all the space grids in the calculation region have been calculated. Within one simulation run, the FDTD approach could work out the resonance spectrum over a wide range of frequency. The FDTD solution has a wide application in simulating the electromagnetic field distribution [2,3].

The Yee Lattice[4] has been used to discrete the electromagnetic fields and provide numerical solutions for the Maxwell equations. The schematic diagram of the Yee Lattice is provided in Figure 5.1. The electric field *E* component is usually stored at the edge of the cube (in the case of 3D) or square (in the case of 2D), and the magnetic field *H* component is stored inside the face of the cube or square.

Under the Cartesian coordinate system, Maxwell equations in Equation (2.7) can be expressed as:

$$-\mu \frac{\partial Hx}{\partial t} = \frac{\partial Ez}{\partial y} - \frac{\partial Ey}{\partial z} \qquad (5.1.a)$$

$$\varepsilon \frac{\partial Ex}{\partial t} = \frac{\partial Hz}{\partial y} - \frac{\partial Hy}{\partial z} \qquad (5.1.b)$$

where μ and ε refer to the permeability and the permittivity respectively. The value for $\frac{\partial Hy}{\partial t}$, $\frac{\partial Hz}{\partial t}$, $\frac{\partial Ey}{\partial t}$ and $\frac{\partial Ez}{\partial t}$ can be obtained in a similar way. Then there is: $F(i\Delta x, j\Delta y, k\Delta z, n\Delta t) = F^n(i, j, k)$. The grids are used to discrete every variable of the functions. For instance, Equation (5.1.a) can be approached in the following way in Equation (5.2):

$$\mu \frac{H_x^{n+\frac{1}{2}}(i,j+\frac{1}{2},k+\frac{1}{2}) - H_x^{n-\frac{1}{2}}(i,j+\frac{1}{2},k+\frac{1}{2})}{\Delta t} = \frac{E_y^n(i,j+\frac{1}{2},k+1) - E_y^n(i,j+\frac{1}{2},k)}{\Delta z} - \frac{E_z^n(i,j+1,k+\frac{1}{2}) - E_z^n(i,j,k+\frac{1}{2})}{\Delta y} \qquad (5.2)$$

In addition, the grid size must satisfy: $\sqrt{(\Delta x)^2 + (\Delta y)^2 + (\Delta z)^2} > c\Delta t = \sqrt{1/\varepsilon\mu}\,\Delta t$. By satisfying this the change in electromagnetic field over one increment of the grid would not be significant, so the field within one lattice can be regarded as a constant which makes the calculation possible . The FDTD approach can also be applied to

the 2D scenarios, e.g. the TE(transverse electric) and TM (transverse magnetic) wave. For the TM mode, the fields satisfy: $E_x = E_y = 0$, $H_z = 0$; For the TE mode, the fields satisfy: $H_x = H_y = 0$, $E_z = 0$. Substituting these values into the scalar functions, the electromagnetic fields for TM and TE modes can be obtained.

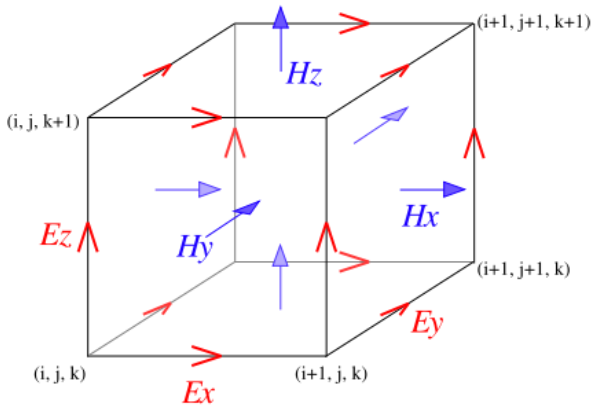

Figure 5.1 The Yee Lattice for discretizing the Maxwell's equations in the FDTD method[4]

The FDTD method is an effective method in electromagnetism but it is worth pointing out that there are also other solutions, typically the finite element method (FEM)[5] and pure analytical method. FEM is often compared with FDTD, but the fundamental difference between the two is that the former computes in the frequency domain and the latter in the time domain as the name suggests. Since it is more common to express the Maxwell equations in the time domain, FDTD is more convenient. In addition, the time domain approach has the advantage of covering a wide range of frequency in one simulation process of the discrete Fourier transform. The analytical method tends to solve the Maxwell equations analytically and only some functions of complex variables have analytical solutions. In the case of whispering gallery mode(WGM), the Bessel function can be applied to solve the eigenfrequencies under cylindrical coordinates. Consistent results have been found by comparing the eigenfrequencies of WGMs obtained from the FDTD approach and from solving the Bessel function analytically[6].

In this thesis, the open-source FDTD software MEEP, developed in MIT (http://ab-initio.mit.edu/) , is adopted to model WGMs of InGaN-based ring cavities. MEEP is implemented under Ubuntu 10, an Linux operation system. In MEEP, the perfectly matched layer (PML)[7] is defined to simulate open boundary conditions. Without the PML, the boundaries tend to reflect back all incident waves and interfere the incident waves. PML is essentially a non-physical material. The function of PML lies that it is as if absorbs all the incident light so that all incident light disappear and won't cause any reflection at the interface.

5.1.2 A review of current study on whispering gallery mode in GaN-based cavities

In the research on GaN-based whispering gallery mode cavities, the Q-factor has been reported in a value between 30 and 4000 for these GaN-based disks and rings on micrometer or nanometer scales. The microdisks of GaN or InGaN QW can be made by photoelectrochemically etching undercut[8,9,10]. The Q-factor obtained experimentally has been improved to a scale of 10^3 . The low value of quality factor in other groups could be attributed to a number of factors, the inclined sidewall surface being one of them [10]. The general performance of GaN/InGaN microdisks is especially remarkable in Everlyn Hu's group, with a high quality factor [8,9,11] and a relatively low threshold for a lasing reported[8]. The tuning of WGMs can be obtained by irradiating onto the disk using a pulsed laser[11]. The shift of the WGM mode is believed to be related to the photo-oxidation due to the strong power irradiation. Photo-generated holes promote GaN oxidation, and then the oxide can be easily dissolved. This is equivalent to reducing the size of the disk, which directly affects the cavity mode.

The comparison of performances of the microdisks and the microrings has also been studied[12]. For many experimental studies in nitride-based microdisks, both the whispering gallery modes (WGM) and the transverse modes have been

observed[12,13,14]. Such two different modes in the cross-section of the hexagonal GaN nanowire are illustrated in Figure 5.3 [12]. Comparing to the microdisks, in the microring structure, only WGM exists while the transverse mode does not exist. A comparative study of nitride microrings and microdisks can be found [14].

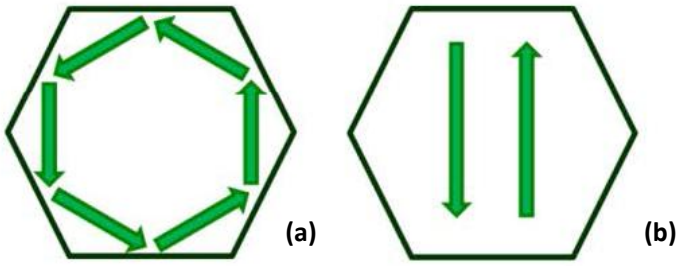

Figure 5.2 Schematic diagram of (a) whispering gallery mode and (b) transverse modes in the Hexagonal GaN microwires [12]

Standard electron-beam lithography has been adopted for the fabrication of nano/micro cavities. Such a point-by-point technique is less efficient comparing to the nanosphere lithography (NSL) technique. Currently, some good result of GaN cavities has been reported using the NSL technique[15].

The present research has suggested that the ring structure is more favourable than the disks since there can be pure WGMs in the former structure. Besides, in recent years, the size of cavities is moving towards to a few micrometers. It is important to obtain an optimal size of a ring cavity in terms of the Q-factor. Some theoretical work is provided in this chapter, which would be helpful for the experimental work on nitride cavities in the group.

5.1.3 Theoretical study of single InGaN-based nanoring cavity

The calculation of InGaN whispering gallery mode cavitiy is performed by using an open-source software MEEP. The commands used for the whole calculation process in this chapter are provided in Apendix I.

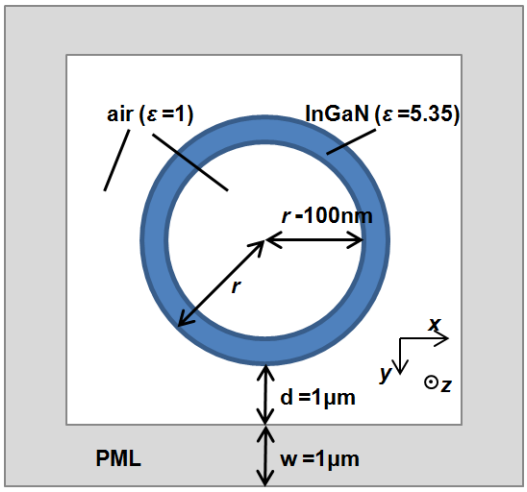

Figure 5.3 Schematic diagram of the ring structure and relative parameters for calculation

This chapter is targeing to design an InGaN nano WGM ring structure. Figure 5.3 shows a schematic diagram of the ring cavity structure used for the calculation. The external ring radius *r* has various values, while the thickness of the ring is fixed as 100nm. In following context, the *ring radius* refers to the external ring radius *r*. Since the wavelength range between 400nm and 500nm is the most concerned, the InGaN cavity has a low In composition of around 5%-20%. The dielectric constant ε for InGaN is assumed to be that for GaN and has a value of 5.35[16]. The distance between the ring edge and the edge of PML (perfect matched layer) is 1 μm, and the thickness of the PML layer is also 1 μm. As has been discussed, the PML layer is set to allow for adequate absorption of the light at the boundary, so that there won't be the reflected light to cause interference in the calculation. A Gaussian source is put in an arbitrary position inside the InGaN ring cavity. The electric field in the *z* direction is studied. The resolution in MEEP is set as 50, which means that there are 50 pixels in one unit (1 μm). By setting this each pixel is less than 1/20 of the resonance wavelength that ensures accuracy[15]. In order to gain a better understanding of the fundamental physics for WGM in InGaN ring cavities, these nanorings are researched in 2 dimensions (2D). A side profile of the 2D structure is not available.

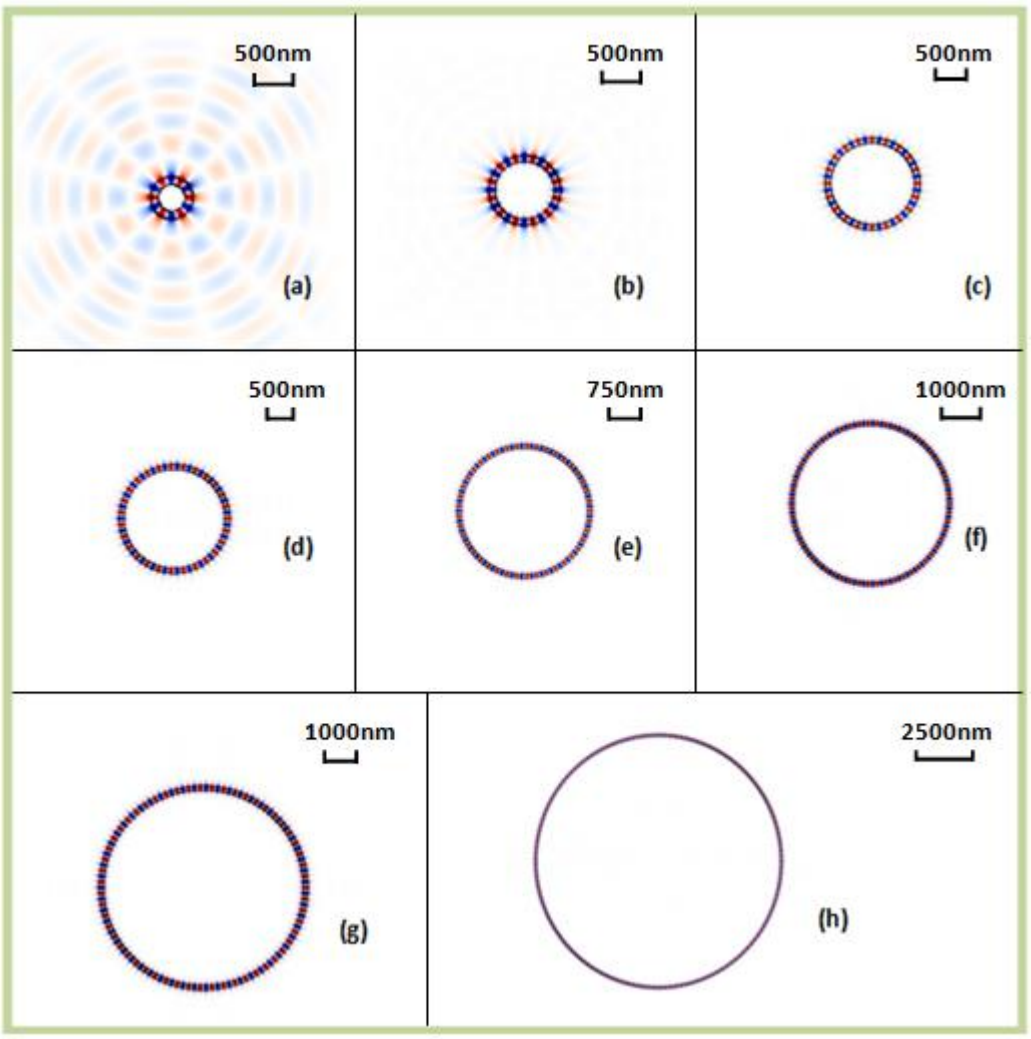

Figure 5.4 The calculated electric field distribution for the rings of different radius in whispering gallery mode at the resonance wavelength of around 430nm. Red and blue dots represents the peak and lowest point of the electric field strength. (a) *r* = 250nm,mode number *m* = 6; (b) *r* = 500nm, *m* = 13; (c) *r* = 750nm, *m* = 20; (d) *r* = 1000nm, *m* = 27; (e) *r* = 1500nm, *m* = 41; (f) *r* = 2000nm, *m* = 55; (g) *r* = 3000nm, *m* = 84; (h) *r* = 5000nm, *m* = 141

Figure 5.4 presents the calculated electric field strength for the rings of different sizes in the whispering gallery mode at a *resonant wavelength* (λ_R) of around 430nm. Note that the light source is placed at an arbitrary position inside the ring in all cases in Figure 5.4 and the accurate position of the light source inside the ring has been found not to make a difference in the calculated field. The ring radius *r* and the mode number *m* have been given for each figure. The red and blue colours represent the peak and low point of the electric field intensity. The clear alternating between blue and red on the ring indicates the whispering gallery mode. In Figure 5.4, the

rings of different sizes can be differed by the number of blue and red dots. This number of blue dots or red dots is equivalent to the mode number of the cavity at this resonance wavelength. For instance, the mode number for the first ring in Figure 5.4 is 6 as can be easily counted. For rings with a bigger radius, the corresponding mode number is larger at the same resonance wavelength.

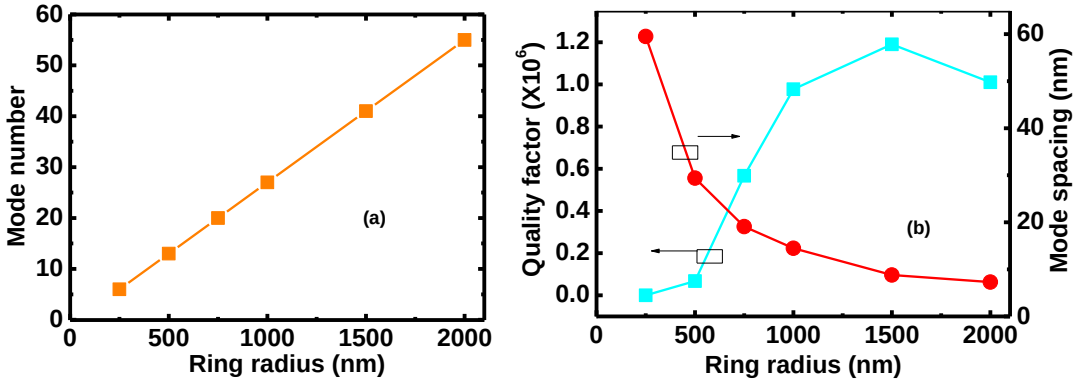

Figure 5.5 The calculated mode number, mode spacing and Q-factor for rings of various radius at the resonance wavelength of around 430nm

Figure 5.5 illustrates the calculated mode number, mode spacing and Q-factor as a function of radius. The quality factor in this study is obtained using the built-in Harminv function in MEEP. The principle is: $Q = \frac{\beta}{|\alpha|} = \frac{\mathrm{Re}(\omega)}{2|\mathrm{Im}(\omega)|}$ (Equation (2.9)). The calculated data is provided in Appendix I. Theoretically, the Q-factor has been found to increase exponentially with increasing the ring radius [17,18].In Figure 5.5, Q increases exponentially with increasing the ring radius (for rings with a small radius up to around 1500nm). As ring size increases, the mode spacing is getting much smaller and the Q-factors calculated for bigger rings are therefore not so accurate. In reality, even a high quality factor can be gained by the big microdisk, this is compensated by the difficulty in identification of each single peak, since the adjacent peaks might merge together. Therefore, for InGaN nanorings, the optimal radius is around 1000nm-1500nm in terms of the Q-factor.

5.2. Mode splitting in InGaN-based nanoring cavities

5.2.1 Principles of the mode splitting effect in whispering gallery modes

Mode splitting for whispering gallery mode refers to the phenomenon of the split of the original single mode. In the resonance spectrum, at least two modes appear: one mode blue shifts and the other red shifts comparing to the original mode resonance frequency. The mode splitting effect has been researched in a single WGM cavity that is surrounded by scattering sources (e.g. quantum dots on the edge) [19], as well as in the coupled WGM cavities[20,21].The magnitude of mode splitting has been used to test the quality and nature of the materials such as the size and the refractive index, which has applications in biosensors [22] and detectors[23]. Due to the mode splitting effect, the coupled WGM cavities are also referred as "Photonic Molecules", because of the similarities between light-matter coupling and the chemical bonds.

Before the concept of "Photonic Molecules" was first raised[24], the coupling between cavities has been explained from a view of electronic circuits[25]. Let A and ω be the amplitude and the resonant frequency. For two separate cavities: $dA_1/dt = j\omega_1 A_1$ and $dA_2/dt = j\omega_2 A_2$.When they approach, an extra perturbation term has to be concerned: $dA_1/dt = j\omega_1 A_1 + j\kappa_{12} A_2$ and $dA_2/dt = j\omega_2 A_2 + j\kappa_{21} A_1$, where the perturbation parameter satisfies: $|\kappa_{12}| << \omega_1$, $|\kappa_{21}| << \omega_2$. Due to the conservation of energy, $\left(d|A_1|^2 + d|A_2|^2\right)/dt = 0$ which gives $|\kappa_{12}| = |\kappa_{21}|$ and the final solution for the new resonant frequency: $\omega = \frac{(\omega_1+\omega_2)}{2} \pm \sqrt{\left(\frac{\omega_1-\omega_2}{2}\right)^2 + |\kappa_{12}|^2}$ = $\omega_r \pm |\kappa_{12}|$ when $\omega_1 = \omega_2 = \omega_r$. The mode splitting hence is associated with the perturbation term $|\kappa_{12}|$ and can be further analysed considering $\omega = 1/\sqrt{LC}$ for normal resonators.

The term "Photonic Molecules" originates from an analogy to the chemical molecule

bonds. Based on numerical calculation method, the electric field distribution (Figure 5.6 a-f)[24] for six lowest confined optical modes was calculated for the photonic molecules as demonstrated in Figure 5.6.g. The electric field in Figure 5.6.a and 5.6.b resemble the bonding and antibonding molecules of the σ-like orbitals of *s* atom states. They are very common in the classical model for the formation of H_2 molecule (as illustrated in Figure 5.6.h), where the bonding and antibonding states are formed when two H atoms approach[26]. The rest four fields resemble the bonding and antibonding σ-like and π-like molecule orbitals formed by *p* atoms. The first two electric fields correspond to the two lowest confined optical modes, which are the basic modes in mode splitting effects and can be easily observed in experiments. Therefore, only the first two modes, σ-like orbitals of *s* atoms, are considered in this study.

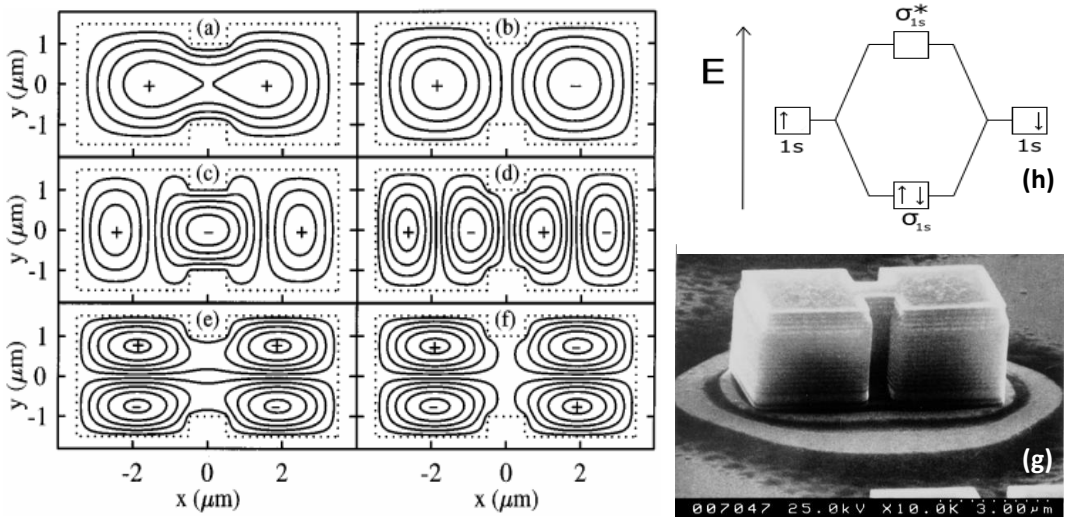

Figure 5.6 (a-f) Calculated electric field for six lowest confined optical modes[24]. (g) Scanning electron micrograph of the photonic molecules[24] (h) Schematic diagram of the formation of H_2 molecule[26].

Figure 5.7 presents the theoretical work on the mode splitting effect in this study. The simulation process has been consistent with that in Section 5.1.3. A pair of two identical rings are considered and the distance between the rings varies as demonstrated in Figure 5.7.a. The calculated electric fields of bonding and antibonding modes are provided in Figure 5.7.b and 5.7.c. The red points and blue

points refer to the peak and the bottom of the electric field intensity respectively. When the red points in one cavity correspond to the red points in the other cavity, it forms the bonding mode; otherwise, it's the antibonding mode.

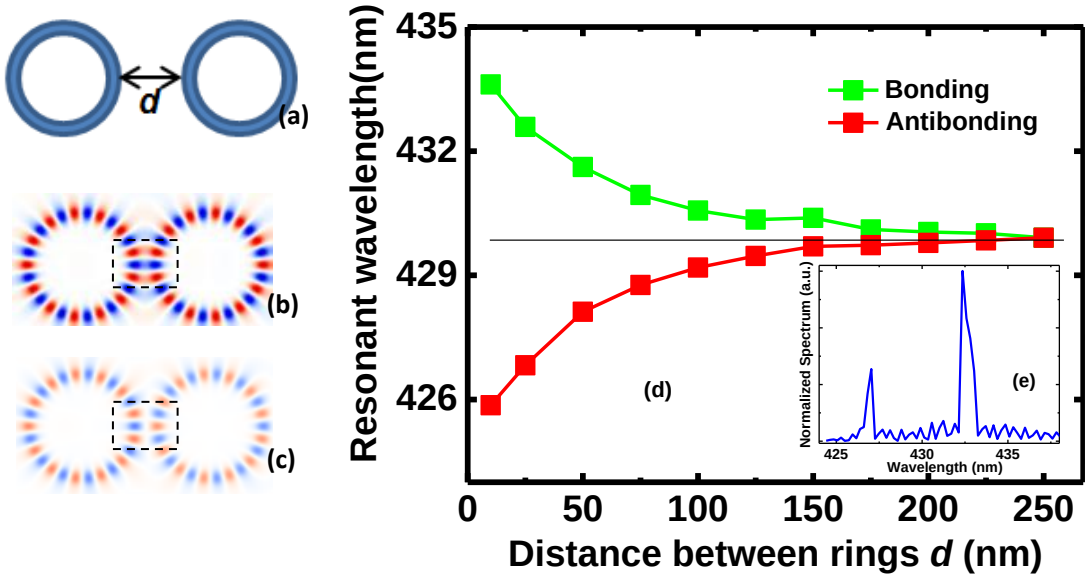

Figure 5.7 Schematic diagram of (a) the pair of ring cavities with certain distance *d* , (b) the bonding mode and (c) the antibonding mode in a pair of ring cavities. The rectangle in dash lines highlights the difference between (b) and (c). (d) The resonance wavelength for bonding and antibonding modes as a function of the ring distance *d* (radius *r* = 500nm). (e) Resonance spectrum for the pair of rings (*r* = 500nm, *d* =25nm).

Figure 5.7.d presents the calculated resonance wavelength for the bonding and antibonding modes as a function of the distance between two rings. The distance between edges of two adjacent rings is defined as *ring distance* in the following context. The resonance spectrum obtained from the FDTD simulation is provided in Figure 5.7.e for the scenario where the ring distance for the two 500nm-in-radius rings is 25nm and the mode is at the resonance wavelength of around 430nm. The original mode has split into two modes at 427nm and 432.5nm respectively. The bonding modes correspond to the red-shifted branch while the antibonding modes are blue-shifted. This is similar with the chemical molecules, where an antibonding molecule requires a stronger energy to form.

Figure 5.7.d demonstrates a clear trend of enhancement of the mode splitting effect

when the ring distance gets smaller, which has also been observed in literatures[20,21]. In this study, the *threshold ring distance* refers to the smallest ring distance for the mode splitting effect to get disappeared. In Figure 5.7.d, the *threshold ring distance* is around 250nm.

5.2.2 Resonant mode splitting for rings in different sizes

In order to further probe the effect of resonant mode splitting and relevant physics, the ring cavities in different sizes are quantitatively analyzed. Prior to that, it has been tested that an increasing number of rings would strengthen the mode splitting effect. Figure 5.8.a-d provides the schematic diagram of the arrays of different number of identical rings and Figure 5.8.b shows the increase of the *mode split energy* (the difference in the resonance energy between the most red-shifted mode and the most blue-shifted bond) with an increasing number of rings, owing to stronger interference with a larger number of rings.

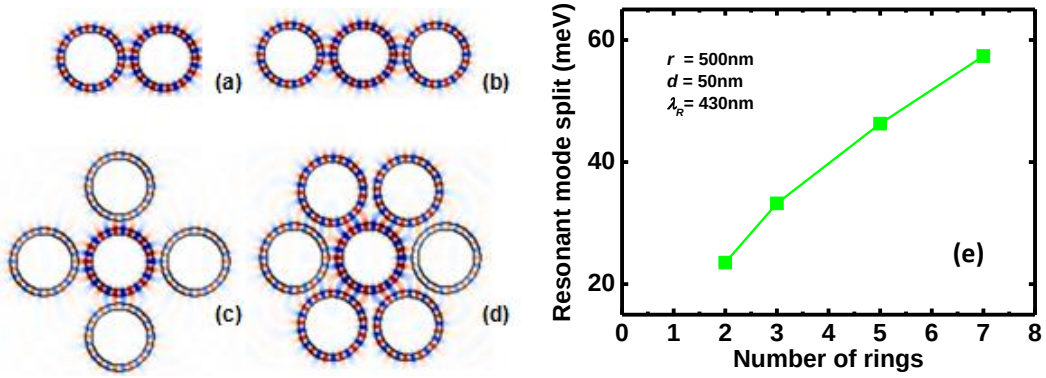

Figure 5.8 Schematic diagram of the ring arrays with (a) 2 rings, (b)3 rings, (c) 5 rings and (d)7 rings. (e) Calculated resonant mode split (meV) for the arrays with different number of rings (radius *r*=500nm, ring distance *d* =50nm), when λ_R≈430nm

In later study, the hexagonal array structure which corresponds to Figure 5.8.d is researched. The hexagonal array is suitable for the wurtzite InGaN structure. The parameter for each ring and the simulation conditions are consistent with what has been explained in Section 5.1.3. The hexagonal ring array structure (as illustrated in Figure 5.8.d) is then applied to InGaN-based ring cavities. Four groups of the

structure were analyzed, and the ring radius for each group is 500nm, 750nm, 1000nm and 1500nm, respectively. The ring distance *d* between any two adjacent rings in one group is also identical. The mode splitting effect is observed for all the four groups with varying the ring distance *d*.

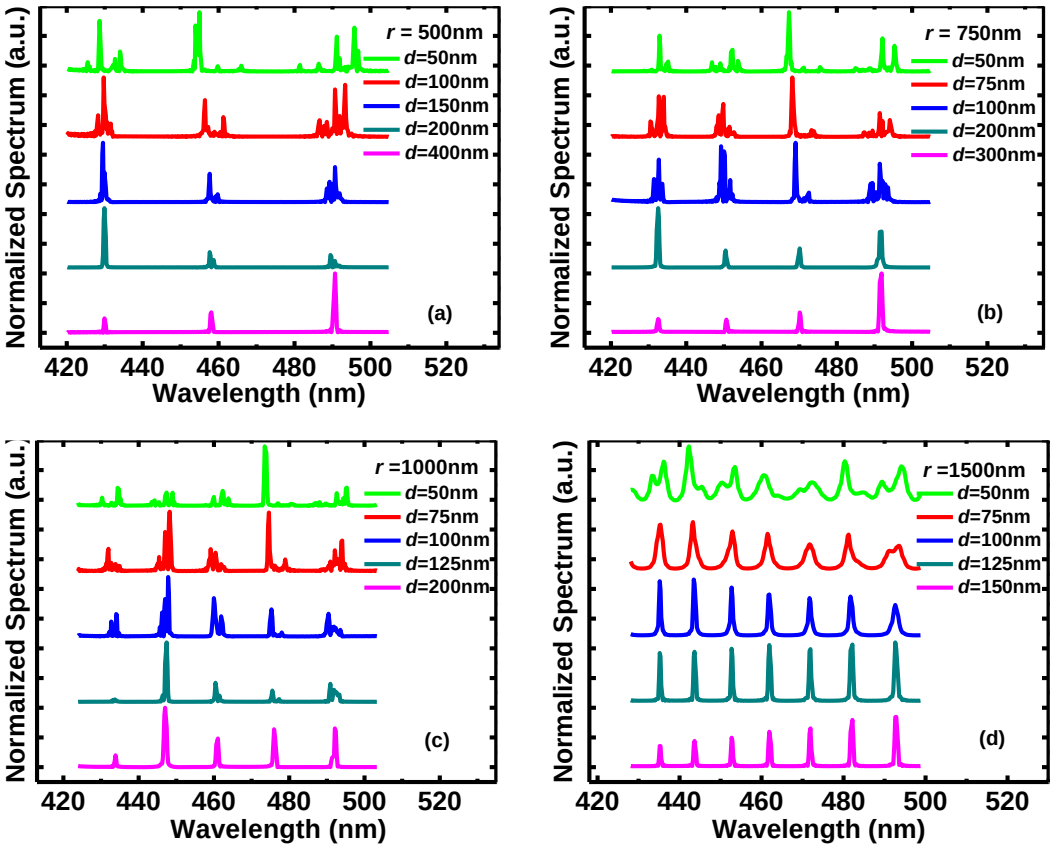

Figure 5.9 The normalized resonance spectrum for hexagonal ring arrays. The ring radius is (a) 500nm (b) 750nm (c)1000nm and (d)1500nm and the ring distance *d* varies as displayed.

Figure 5.9.a-d plot the effect of mode splitting when varying the ring distance for the hexagonal ring arrays (as illustrated in Figure 5.8.d) with a ring radius of 500nm, 750nm, 1000nm and 1500nm, respectively. Comparing the mode splitting effect for rings of different sizes, it is found that the ring array formed by smaller rings has a larger *threshold ring distance*. For instance, while a strong mode splitting effect can be observed at a ring distance of 150nm for the 500nm-in-radius ring array, there is no splitting effect at the same ring distance for the 1500nm-in-radius ring array. It should be noted that for each ring array, modes at lower resonance wavelengths (i.e.

modes with higher mode numbers) always have a smaller mode split energy than modes at higher resonance wavelengths. For instance, at a ring distance of 100nm for the 1500nm-in-radius ring array, the mode splitting effect can hardly be recognized in the mode at 426nm, but it is still prominent in the mode at 505nm.

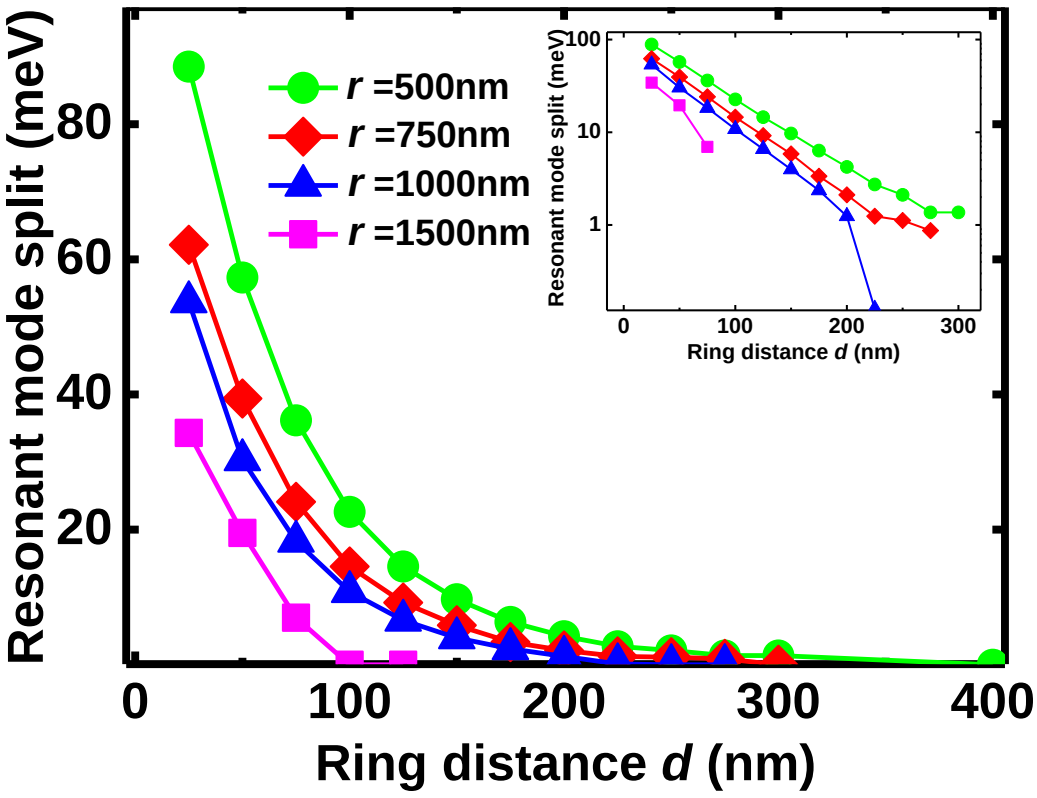

Figure 5.10 The resonant mode split energy (meV) as a function of the ring distance (λ_R≈430nm), for ring arrays formed by rings in radius of 500nm, 750nm, 1000nm and 1500nm. Inset is the mode split energy (meV) in the logarithm scale.

Figure 5.10 plots the mode split energy(meV) as a function of the ring distance for rings of different sizes, in order to better understand the influence of the ring size on the mode splitting effect. The inset shows the mode split energy(meV) in the logarithm scale. The mode split energy indicates the strength of the mode splitting effect. Figure 5.10 clearly demonstrates that, at all ring distances, the ring array formed by smaller rings always have a larger mode split energy than that formed by larger rings. In the logarithm scale, the decay lines of the mode split energy are impressively straight, indicating the essence of an exponential decay for the mode

split energy as a function of the ring distance.

In order to deeply understand why the mode slit energy declines with the ring distance, the evanescent wave coupling is involved for the mode splitting phenomenon. Evanescent wave exists at the interface of two materials with different dielectric constants. Under the total internal reflection, there still exists the evanescent wave going out from the high-dielectric-constant material to the low-dielectric-constant material (normally air), and the evanescent wave is propagating along the surface.

Figure 5.11.a below illustrates the evanescent wave (*Ev*) in the total internal reflection:

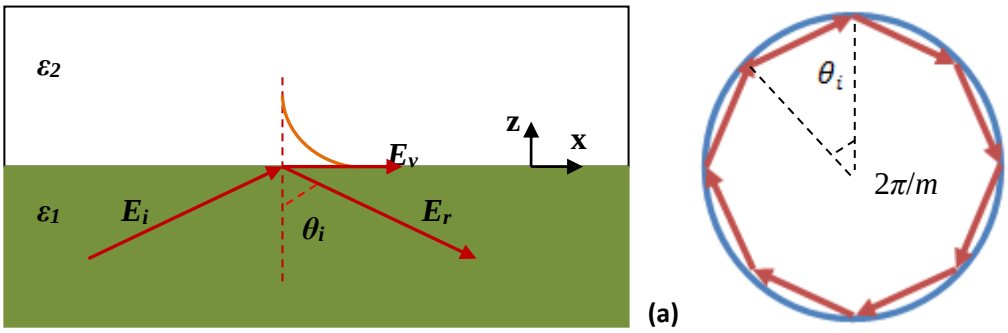

Figure 5.11 (a) Schematic diagram of the evanescent wave (E_v) in total internal reflection.(b) Schematic diagram of the relationship between the incident angle ϑ_i and the mode number *m*

In order to derive the evanescent wave E_v, first of all, transmitted wave-number is: $k_T = k_T \sin(\theta_T)\hat{x} + k_T \cos(\theta_T)\hat{z} = k_{Tx}\hat{x} + k_T \cos(\theta_T)\hat{z}$. The Snell's law requires: $\sin(\theta_T) = \frac{n_1}{n_2}\sin(\theta_i)$. At the critical incident angle, $\sin(\theta_T)$=1. Under total internal reflection, θ_i continues to increase, and in order to stick to the Snell's law, there will be $\sin(\theta_T)$>1. Hence, $\cos(\theta_T) = \sqrt{1-\sin^2(\theta_T)} = i\sqrt{\sin^2(\theta_T)-1}$.

Therefore: the electric field of the transmitted wave becomes[27]:

$$E_T = E_0 e^{i(xk_{Tx}+zk_T i\sqrt{\sin^2(\theta_T)-1})} = E_0 e^{-\alpha z} e^{ik_{Tx}x} \qquad (5.3)$$

Where: E_0 is the amplitude of the transmission field, and it relates to the amplitude of the incident field. α is named as the attenuation constant, which is an important parameter for the evanescent wave. Using the Snell's law and the factor that the permeability in non-magnetic materials follows: $\mu_1 \approx \mu_2 \approx \mu_0$, there is : $\sin^2(\theta_T) = \frac{\varepsilon_1}{\varepsilon_2}\sin^2(\theta_i)$. Besides, k_T satisfies: $k_T = 2\pi/\lambda$. After little algebra, the expression for the attenuation constant α is found:

$$\alpha = \frac{2\pi}{\lambda}\sqrt{\frac{\varepsilon 1}{\varepsilon 2}\sin^2(\theta_i) - 1} \qquad (5.4)$$

From Equation (5.3), it can be clearly seen that the evanescent field is decaying exponentially in the *z* direction, which is the depth into the low-dielectric-constant material. This explains why the mode splitting energy drops exponentially with the ring distance.

In Equation (5.4) of the expression of the attenuation constant, $\varepsilon_1/\varepsilon_2$ is fixed for certain cavities, and the resonance wavelength λ_R is almost a constant, e.g. 490nm. However, θ_i changes for rings of different sizes. Since $2\pi nr \approx m\lambda_R$, at the same resonance wavelength λ_R, the mode number is m is higher for rings of larger radius r. For higher m, the incident angle θ_i is larger according to $\theta_i = (\pi - 2\pi/m)/2$, as illustrated in Figure 5.10.b. Consequently, a larger θ_i for the larger ring leads to a higher value of α, indicating a faster decay of the evanescent field into the low-dielectric-constant material. This results in a weaker mode splitting effect and a smaller mode split energy in rings of larger size.

In each ring array, modes at higher resonance wavelengths normally have smaller mode split energies. This can also be explained by Equation (5.4). In Figure 5.8.a (radius r = 500nm), the mode around 490nm (mode number m = 11) exhibits a larger mode split energy comparing with the other two (λ_R = 460nm, m = 12; λ_R = 430nm, m = 13). In this scenario, the resonance wavelength λ_R is the major reason, since it is inversely proportional to the attenuation constant α according to Equation (5.4).

Mode number *m* is also a factor in Equation(5.4), but the difference between 11 and 13 is not prominent. λ_R influences the attenuation constant and the mode split energy for modes at different resonance wavelengths in each ring array.

5.2.3 Mode splitting and the Q-factors for WGM cavities

For InGaN-based cavity applications, the Q-factor is an important factor for the quality of the cavities. While the mode split energy is a main concern in applications of biological sensors and detectors, the influence of mode splitting on Q-factors is more emphasized in applications such as resonators and laser diodes. This section studies the Q-factors for a pair of rings with a small ring distance where the mode splitting effect exists. The simulation parameters are consistent with the description in Section 5.1.3. The schematic diagram of the pair of rings has been provided in Figure 5.8.a.

Figure 5.12 below presents the Q-factors for the bonding and antibonding modes of the ring pair (1000nm-in-radius for each ring). The three figures refer to the modes at the resonant wavelength around 430nm, 460nm and 490nm, respectively. The Q-factors are calculated by the built-in Harminv function[28] which basically follows the method: $Q = \frac{\beta}{|\alpha|} = \frac{\mathrm{Re}(\omega)}{2|\mathrm{Im}(\omega)|}$ (Equation (2.9)). It can be found that at a small ring distance up to around 100nm, the Q factor for either the bonding mode or the antibonding mode can sometimes exceed the value for a single ring (marked as the dashed line in each figure). As the ring distance increases, the Q-factor for both modes decreases to 1/20 of the single ring Q-factor. Normally there is just one branch (bonding or antibonding) with a high Q value and the Q-factor in the other branch is suppressed. From the calculated results, it is suggested that if two rings are 25-50nm apart, the Q-factor from one branch of the split modes can be 2-3 times higher than the Q-factor for a single ring. This throws light upon the design of high-Q InGaN-based cavities.

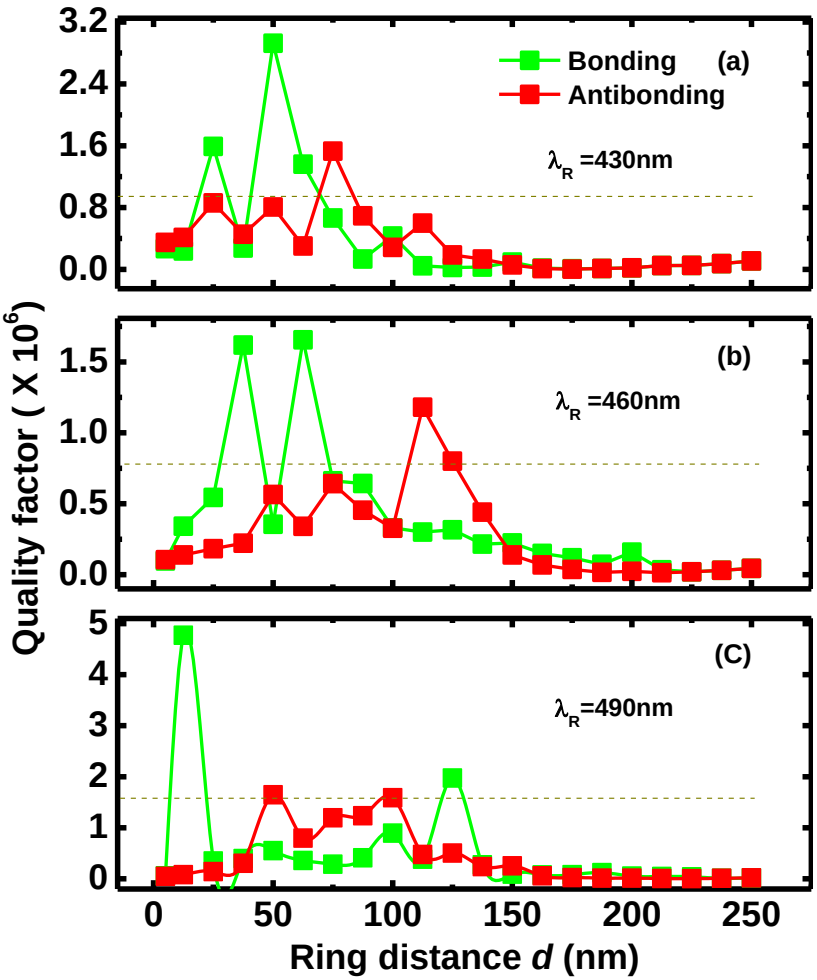

Figure 5.12 Quality factors for bonding and antibonding modes when varying the ring distance for modes at resonance wavelength around (a) 430nm, (b) 460nm and (c) 490nm. The ring radius is 1000nm.

The scenario of size mismatched rings is also studied. Figure 5.13.a illustrates the ratio of radius for two ring r_2/r_1. In calculation, r_1 is kept as 1000nm and the ring distance is 50nm. r_2/r_1 varies from 0.8 to 1.0. Figure 5.13.b plots the resonant wavelength for one mode (mode number m = 24) when the ring radius r_2/r_1 varies.

From Figure 5.13.b, as r_2 reduces, the resonant energy for a certain mode is blue-shifted. This is reasonable considering $2\pi nr \approx m\lambda_R$ for a single ring. A prominent anticrossing phenomenon can be observed for the bonding and anti-bonding mode. Note that at the anticrossing points (r_2/r_1 = 0.915 and 0.84), the two modes approach but repel without crossing each other, because the bonding mode energy has always to be lower than the antibonding mode. If r_2/r_1 continues to

decrease, more anticrossing points can be observed.

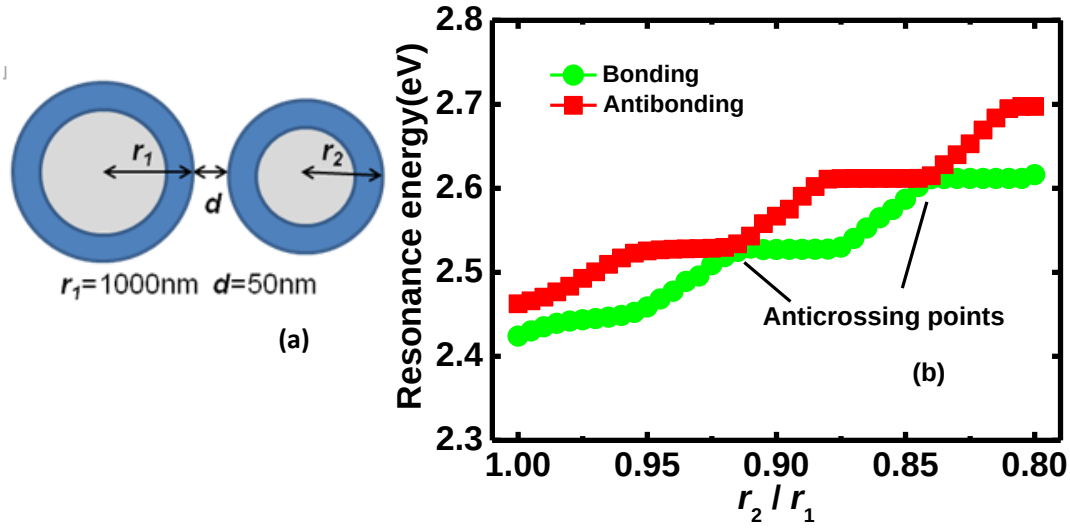

Figure 5.13 (a) Schematic diagram of the pair of size-mismatched ring cavities. (b) The resonance energy for the bonding and antibonding modes when the radius ratio r_2/r_1 varies. Two anticrossing points are marked in (b).

Anticrossing is a common phenomenon in quantum chemistry and solid state physics. It occurs when the curves of two eigenvalues as a function of a parameter *P* (here it is the ratio of ring radius, r_2/r_1) are about to cross, but they repel each other and avoid the crossing. The energy values for the two eigenvalues in the existence of strong mutual repelling can be obtained by considering the extra perturbation terms in the Hamiltonian expression [29].

Figure 5.14 presents the quality factor at the anticrossing points for the bonding and antibonding modes. At the anticrossing points, the phenomena of switching energies and Q-factors between two modes have been discovered both theoretically[30] and experimentally[31]. In Figure 5.14, before the anticrossing points, the antibonding mode is of a high Q-factor, while the bonding mode is of a low Q-factor. After the anticrossing points, the Q-factor in the antibonding mode quickly drops and the bonding mode gains a high Q-factor which is almost comparable to the previous value for the antibonding mode. This suggests a clear switch of the high Q-factor between the two modes. Since a cavity of a high Q-factor always has a better

capability of confining the energy, the switch of the Q-factor also indicates the switch of energy for the two modes in this pair of InGaN-based WGM ring cavities.

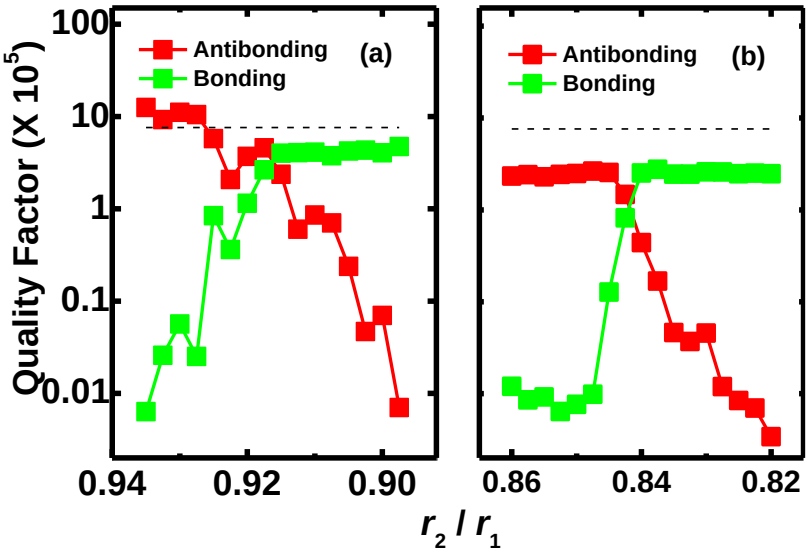

Figure 5.14 (a) and (b) Quality factors at two anticrossing points for the bonding and antibonding modes as a function of the radius ratio r_2/r_1. The dashed line shows the Q-factor for this mode in a sing ring

In addition, at the anticrossing points, the Q-factor for both modes drops. Especially, for more severe size mismatch in Figure 5.14.b comparing with Figure 5.14.a, the loss of Q-factor is more prominent and Q-factor keeps at a lower value than that for a single ring cavity. Mode splitting has been found to improve the quality factor in the pair of identical rings of a small ring distance, which is regarded as one significance of the mode splitting effect. However, in this pair of severely size-mismatched rings, the Q-factor is degraded due to mode splitting. The mode splitting effect shall be employed properly to generate high Q-factor ring cavities.

5.3.Summary

In summary, the whispering gallery mode (WGM) from the ring cavity structure has been studied on the InGaN system. A high quality factor can be achieved in the WGM because of a good confinement of light in a cylindrical structure. The ring structure is even more favourable than the disk structure because the former can

have pure WGMs and exclude the formation of transverse modes.

For a single ring cavity, there exists a “trade-off” between the quality factor and the mode spacing. According to calculations, the Q-factor increases significantly when the ring size increases. However, for rings with a radius larger than 5000nm, the separation between two adjacent modes becomes so small that the two adjacent modes are not recognizable. The optimal radius for InGaN rings is suggested to be 1000nm-1500nm in terms of the Q-factor. At the resonance wavelength of 400nm-500nm, the Q-factor for these optimal rings can reach up to 10^6.

The mode splitting is a common phenomenon when ring distance becomes small. The bonding and antibonding branches of the optical modes are observed with the bonding mode of a lower-energy, which is similar to the chemical molecule bonds. When the ring distance is 25-50nm, there can be one mode from either the bonding or antibonding branch with a Q-factor 2-3 times higher than that for a single ring cavity. In addition, if the two ring cavities are of the identical size, the modes will be blue-shifted when reducing the size of one ring. There exists the anticrossing points and a switch of energy between the bonding and anti-bonding modes when varying the radius ratio of the two rings. The Q-factor is likely to degrade in size-mismatched ring pairs. The mode splitting technique can be employed properly for designing high Q-factor ring cavities and laser diodes.

Reference

[1] Kunz, K. S., & Luebbers, R. J. (1993). *The finite difference time domain methods for electromagnetics*. Florida: CRC press

[2] Taflove, A. (2005). *Computational Electromagnetics: The Finite-Difference Time- Domain Method.* Boston: Artech House

[3] Sullivan, D. M. (2000). *Electromagnetic simulation using the FDTD method.*

New York: IEEE Press Series

[4] Yee, K. (1966). Numerical solution of initial boundary value problems involving Maxwell's equations in isotropic media. *Antennas and Propagation, IEEE Transactions on*, 14(3): 302-307

[5] Dhatt, G., & Touzot, G. (2012). *Finite Element Method*. NY: John Wiley & Sons

[6] Franchimon, E. (2010). *Modelling circular optical micro resonators using whispering gallery modes.* Master thesis for University of Twente

[7] Berenger, J. P. (1994). A perfectly matched layer for the absorption of electro-magnetic waves. *J. Comp. Phys.*, *114*(2):185-200

[8] Tamboli, A. C., Haberer, E. D., Sharma, R., Lee, K. H., Nakamura, S., & Hu, E. L. (2006). Room-temperature continuous-wave lasing in GaN/InGaN microdisks. *Nature photonics*, 1(1): 61-64

[9] Tamboli, A. C., Schmidt, M. C., Hirai, A., DenBaars, S. P., & Hu, E. L. (2009). Observation of whispering gallery modes in nonpolar m-plane GaN microdisks. *Appl. Phys. Lett.*, 94(25): 251116-251118

[10] Choi, H. W., Hui, K. N., Lai, P. T., Chen, P., Zhang, X. H., Tripathy, S., & Chua, S. J. (2006). Lasing in GaN microdisks pivoted on Si. *Appl. Phys. Lett.*, *89*(21):211101-211104

[11] Aharonovich, I., Niu, N., Rol, F., Russell, K. J., Woolf, A., El-Ella, H. A., & Hu, E. L. (2011). Controlled tuning of whispering gallery modes of GaN/InGaN microdisk cavities. *Appl. Phys. Lett.*, 99(11): 111111-111113

[12] Coulon, P. M., Hugues, M., Alloing, B., Beraudo, E., Leroux, M., & Zuniga -Perez, J. (2012). GaN microwires as optical microcavities: whispering gallery modes Vs Fabry-Perot modes. *Opt. Express*, 20(17): 18707-18716

[13] Mair, R. A., Zeng, K. C., Lin, J. Y., Jiang, H. X., Zhang, B., Dai, L., ... & Khan, M. A. (1998). Optical modes within III-nitride multiple quantum well microdisk cavities. *Appl. Phys. Lett.*, 72(13): 1530-1532

[14] Zeng, K. C., Dai, L., Lin, J. Y., & Jiang, H. X. (1999). Optical resonance modes in InGaN/GaN multiple-quantum-well microring cavities. *Appl. Phys. Lett.*,75(17): 2563-2565

[15] Li, K. H., Ma, Z., & Choi, H. W. (2011). High-Q whispering-gallery mode lasing from nanosphere-patterned GaN nanoring arrays. *Appl. Phys. Lett.*, 98(7): 071106-071108

[16] Dielectric constant for GaN, retrieved from: http://www.ioffe.rssi.ru /SVA/NSM/ Semicond/GaN/optic.html

[17] Prkna, L., Čtyroký, J., & Hubálek, M. (2004). Ring microresonator as a photonic structure with complex eigenfrequency. *Optical and Quantum Electronics*, 36(1-3): 259-269

[18] Gorodetsky, M. L., Savchenkov, A. A., & Ilchenko, V. S. (1996). Ultimate Q of optical microsphere resonators. *Opt. Letters*, 21(7): 453-455

[19] Özdemir, Ş. K., Zhu, J., He, L., & Yang, L. (2011). Estimation of Purcell factor from mode-splitting spectra in an optical microcavity. *Phys. Rev. A*, 83(3): 033817-033820

[20] Boriskina, S. V. (2010). Photonic molecules and spectral engineering. In *Photonic microresonator research and applications*. NY: Springer. pp, 393-421

[21] Preu, S., Schwefel, H. G. L., Malzer, S., Döhler, G. H., Wang, L. J., Hanson, M., & ossard, A. C. (2008). Coupled whispering gallery mode resonators in the Terahertz frequency range. *Opt. Express*, 16(10): 7336-7343

[22] Gamba, J. M. (2012). *The role of transport phenomena in whispering gallery mode optical biosensor performance*. PhD thesis, California Institute of Technology.

[23] Kim, W., Ozdemir, S. K., Zhu, J., He, L., & Yang, L. (2010). Demonstration of mode splitting in an optical microcavity in aqueous environment. *Appl. Phys. Lett.*, 97(7): 071111-071113

[24] Bayer, M., Gutbrod, T., Reithmaier, J. P., Forchel, A., Reinecke, T. L., Knipp, P. A., et al. (1998). A Molecule of Light. *Phys. Rev. Lett*, 81: 2582-2584

[25] Haus, H. A. (1984). *Waves and fields in optoelectronics (Vol. 1, No. 1)*. Englewood Cliffs, NJ: Prentice-Hall. pp, 211

[26] Reger, D. L., Goode, S. R., & Ball, D. W. (2009). *Chemistry, Principles and Practice*. Connecticut: Cengage Learning, pp, 406

[27] Derivation of the evanescent wave, retrieved from: http://dtl.unimelb.edu.au //exlibris/dtl/d3_1/apache_media/L2V4bGlicmlzL2R0bC9kM18xL2FwYWNoZV9t ZWRpYS8xMTIxODg=.pdf, since July 2013

[28] Introduction of the built-in Harminv function in MEEP. Retrieved from: http://ab-initio.mit.edu/wiki/index.php/Harminv

[29] Wiersig, J. (2006). Formation of long-lived, scarlike modes near avoided resonance crossings in optical microcavities. *Phys. Rev. Lett.* 97:253901-253904

[30] Boriskina, S. V. (2007). Coupling of whispering-gallery modes in size-mismatched microdisk photonic molecules. *Opt. Lett.*, 32(11):1557-1559

[31] Witzany, M., Liu, T. L., Shim, J. B., Hargart, F., Koroknay, E., Schulz, W. M et al. (2013) Strong mode coupling in InP quantum dot-based GaInP microdisk cavity dimers. *New J. Phys.*, 15(1): 013060-013064

6. Theoretical study of InGaN quantum dot intermediate band solar cells

This chapter presents theoretical work on modeling an InGaN quantum dot solar cell, which is one type of the intermediate band solar cells (IBSC) and also employs the advantage of the prominent piezoelectric field in the wurtzite structure. The main contribution of this work is proposing the optimized InGaN quantum dot (QD) IBSC (QD-IBSC) structure, which generates intersubband transitions with the intermediate band energy close to predicted optimal values and considers the piezoelectric potential in the quantum structure, reaching a highest conversion efficiency of 55.4%. The combination of the single junction IBSC structure and the piezoelectric effect paves the way for the fabrication of InGaN based single-junction solar cells with an ultra-high energy efficiency.

In Section 6.1, the principle of IBSCs and the rationale for QD-IBSCs is briefly analyzed. The $k{\cdot}p$ method has been adopted to calculate the optimal band structure for the InGaN QD solar cell. In Section 6.2, the mechanism of the piezoelectric field in the heterostructure p-n junction is studied. The enhancement of the built-in potential leads to a reduction of the reverse saturation current density and an increase of the open circuit voltage. In Section 6.3, the solar cell conversion efficiency is calculated on the optimized band structure with considering the effect on the open circuit voltage due to the piezoelectric field.

6.1. Theoretical modelling of the optimized band structure for InGaN QD-IBSCs

6.1.1 Mechanisms for InGaN QD IBSCs

Theoretically, the concept of intermediate-band solar cells (IBSCs) provides an alternative option for high efficiency solar cells based on a single junction. Luque and Martí predicted a thermodynamic upper limit efficiency of up to 63.1% for an IBSC with a single intermediate band (IB) under full concentration, i.e., 46000 suns[1]. The eigenstate of the conduction band in the quantum dot (QD) is regarded as the intermediate band (IB) that lies between the conduction band (CB) and the valence band (VB) of the barrier. The barrier absorbs the photons with the energy above the band gap of the barrier, while QDs absorb photons with an energy larger than the energy separation between IB and VB, and smaller than the band gap of the barrier. Under such a mechanism, two levels of photon absorption can be realized that increases the photon generated current density.

Due to the so-called bottleneck effect as a result of the discontinuous wave number in the QD structures[2,3], the QD system can sustain the intermediate band which is essential for the IBSC structure. Otherwise, when the density of states is continuous in at least one direction, electrons could quickly relax from CB to IB, as in the case of the QW system. Even though the phonon bottleneck effect causes problems for QD lasers due to difficulties in carrier relaxation and radiative recombination, it is a favourable effect for the QD-IBSC and leads to the feasibility of forming a three-band structure for the IBSCs.

III-nitride based QD-IBSC would potentially exhibit superior performance compared with InAs based QD-IBSC in terms of the solar cell conversion efficiency. This owes to its strong piezoelectric fields as a result of the large lattice-mismatch between InN and GaN. So far, the lattice-mismatch induced piezoelectric fields have

been widely studied for InGaN based light emitting diodes or laser diodes. However, they have never been considered in designing IBSCs. It is well-known that the performance of solar cells depends on several factors such as the open-circuit voltage and the short-circuit current density, etc. The piezoelectric fields has been suggested to increase the open-circuit voltage and hence improve the performance of solar cells[4,5].

Therefore, in theory, InGaN QD-IBSCs are supposed to combine the major advantages from the IBSC structure and the major benefits due to the strong piezoelectric effect, which would be more attractive compared with any other QD-IBSC system.

In this study, an InGaN based QD-IBSC structure is firstly proposed, where $In_xGa_{1-x}N/In_yGa_{1-y}N$ multiple QD layers as an absorption region are sandwiched between p-GaN and n-GaN. With a proper design in terms of indium composition of both the barrier and the QDs and size of the QDs, the optimized matrix bandgap and the IB energy can be obtained. Subsequently, a conversion efficiency, open-circuit voltage and short-circuit current have been calculated.

6.1.2 Methods of band structure calculation using the *k·p* theories

In this section, the methods of band structure calculation for InGaN QD-IBSCs are studied. According to the prediction for a single IB, $In_xGa_{1-x}N$ with its bandgap of 1.95eV as a barrier and the intersubband transition energy as 1.26eV are desired [1]. With a proper design in terms of indium composition of both the barrier and the quantum dot, and shape and size of the quantum dot, the optimized matrix bandgap and the IB energy can be obtained.

In the calculation method, the Poisson equation is to be solved that considers the polarization charges. The 6 band $k \cdot p$ method is employed[6]. The built-in software Nextnano3 is adopted for the calculation[7].

Poisson equation

The Poisson equation is used to solve the electrostatic profile across the electric device. It derives from the Gauss' law, and uses the Laplace operator for the electrostatic potential and is given in Equation (6.1).

$$\nabla^2\varphi = -\frac{\rho}{\varepsilon_S}, \text{ or } \quad \nabla\cdot[\varepsilon_S(x)\nabla\varphi(x)] = -\rho(x) \quad , \qquad (6.1.a)$$

$$-\rho(x) = e[-n(x) + p(x) + N_D(x) - N_A(x) + \rho_{piezo}(x)] \qquad (6.1.b)$$

where the $\varphi(x)$ is the electrostatic potential, $\mathcal{E}_S$ is the dielectric constant and $\rho(x)$ is the charge density distribution. $\rho(x)$ consists of electron density $n(x)$, hole density $p(x)$, ionized donor density $N_D(x)$, and ionized acceptor density $N_A(x)$. In addition, an extra charge density due to the piezoelectric polarization has been added, labelled as $\rho_{piezo}(x)$. The bulk Poisson equation is adapted to the strained structures by adding such extra charge density.

The Neumann boundary [7] is the second category of boundary condition for the Poisson function and is adopted in this study. Under the Neumann boundary condition, the gradient of the electrostatic potential is zero: $d\varphi/dx = 0$. The Neumann boundary condition is suitable for equilibrium simulations.

6 band *k·p* method

The *k·p* perturbation theory is widely adopted for band structure calculation in solid state physics. *k* is the three dimensional wave vector in a unit of inverse length, and *p* is a vector of operators. $k\cdot p = k_X(-i\hbar\frac{\partial}{\partial x}) + k_Y(-i\hbar\frac{\partial}{\partial y}) + k_Z(-i\hbar\frac{\partial}{\partial z})$. The theory can be expressed in Equation (6.2)[8]:

$$H_n\Psi_{n,k} = (H_0 + H_k^{'})\Psi_{n,k} = (\frac{p^2}{2m} + V + \frac{\hbar^2k^2}{2m} + \frac{\hbar k\cdot p}{2m})\Psi_{n,k} = E_n\Psi_{n,k} \qquad (6.2)$$

Where, $H_0 = \frac{p^2}{2m} + V$ is the unperturbed Hamiltonian, and $H_k^{'} = \frac{\hbar^2k^2}{2m} + \frac{\hbar k\cdot p}{2m}$ is the

Hamiltonian for the perturbation. In addition, an extra Hamiltonian term of the spin-orbit is usually taken into consideration.

Early research of the $k \cdot p$ method dates back to the 1950th [8,9] and the $k \cdot p$ method for wurtzite structure was later studied [6]. In the 6 band $k \cdot p$ model, the 6 bands refer to the three valence bands and two-fold for each due to the spin. In short summary, the following parameters are required for the band structure calculation[6,7]:

• the energy parameters: band gap energy E_{gap} at the Γ point (k = 0), Δ_{cr} (the energy gap between the *hh* band and *lh* band at the Γ point) and Δ_{so} (and the energy between the *lh* band and the *so* band at the Γ point);

• the conduction band mass including the longitudinal and transverse mass.

• the Luttinger parameters κ (A_1-A_6).

• the band deformation potential D_1- D_4, and the absolute deformation potential a_{cz}, a_{ct}. D_5 and D_6 can be derived from D_1- D_4.

• the elastic constant C_{13} and C_{33} that are used in the calculation of strain tensors.

• the spontaneous polarization $P_{sp.}$

The values for all the parameters in the calculation are provided below in Table 6.1. They are summarized from literature[10]. In addition, a band offset (ΔE_C: ΔE_V ~ 0.7: 0.3) is used to calculate the intersubband transition energy level (E_i)[11], and the bandgap bowing parameter of the InGaN alloy is set as 1.43[12]. Apart from the band energy, other parameters for the InGaN alloy all follow a linear interpolation relationship. The commands on Nextnano using this method and the following parameters are provided in Appendix II.

Table 6.1. Parameters used in the *k·p* calculation of the QD band structure

	GaN	*InN*
E_g (eV)	3.42	0.77
Δ_{cr}(eV)	0.010	0.040
Δ_{so}(eV)	0.017	0.005
Electron mass (m_e^*/m_0)	m_t^*=0.20 m_l^*=0.20	m_t^*=0.07 m_l^*=0.07
Hole mass (m_h^*/m_0)	m_{hht}= 1.60 m_{hhl} = 1.10	m_{hht} = 1.63 m_{hhl} = 1.63
a(Å)	3.189	3.545
c(Å)	5.185	5.703
A_1	-7.21	-8.21
A_2	-0.44	-0.68
A_3	6.68	7.57
A_4	-3.46	-5.23
A_5	-3.40	-5.11
A_6	-4.90	-5.96
a_{cz}(eV)	-7.1	-4.2
a_{ct}(eV)	-9.9	-4.2
D_1(eV)	-3.6	-3.6
D_2(eV)	1.7	1.7
D_3(eV)	5.2	5.2
D_4(eV)	-2.7	-2.7
C_{13}(GPa)	106	92
C_{33}(GPa)	398	224
P_{sp}(C/m^2)	-0.034	-0.042

6.1.3 Band structure for the optimized InGaN/GaN QD-IBSC

Through calculation, the optimal structure is found that produces the matrix bandgap

energy and the IB energy in a value most closed to the required energies [1]: the indium composition is obtained as 0.4 for the barrier and 0.8 for the quantum dot, respectively. The schematic diagram of one InGaN quantum dot is plotted in Figure 6.1.a. It's in a shape of the hexagonal pyramid with a flat top. The height of the QD is 3nm. The width for each side of the hexagon in the bottom is 8nm, and the width for the hexagon in the top surface is fixed as one fourth of the value for the bottom hexagon, as illustrated in Figure 6.1.a. The wetting layer is of the identical Indium composition with the quantum dot and with a thickness of 0.5nm. In the whole process, only three parameters, the Indium composition for the barrier and QD, and the width of the bottom hexagon, are regarded as the variables, while the other parameters are fixed. The matrix bandgap and IB energy for Barrier $In_{0.4}Ga_{0.6}N$/ QD $In_{0.8}Ga_{0.2}N$ structure is 1.987eV and 1.329eV, which are close to the values in previous prediction. The later theoretical calculations in this study, other structures have also been calculated and show a lower conversion efficiency. This proves the structure proposed here is the optimized structure for InGaN QD IBSC.

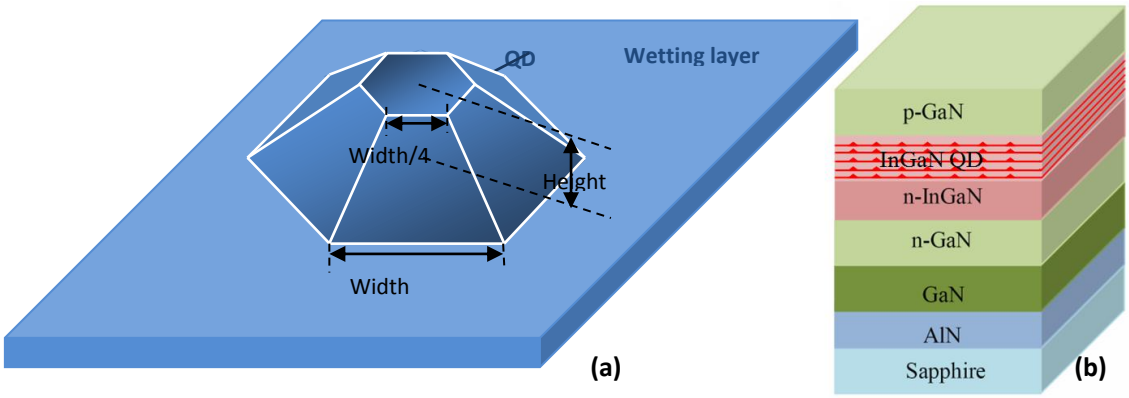

Figure 6.1 Schematic diagram for (a) the structure of each quantum dot and (b) the designed InGaN QD based intermediate band solar cell

The schematic diagram of the $In_{0.4}Ga_{0.6}N$ (Barrier)/ $In_{0.8}Ga_{0.2}N$ (QD) structure for InGaN QD-IBSCs is given in Fig 6.1.b. Following an initial standard undoped GaN buffer and then an *n*-GaN layer on the sapphire, an $In_{0.4}Ga_{0.6}N$ strain-balanced layer

is grown before the $In_{0.4}Ga_{0.6}N$/ $In_{0.8}Ga_{0.2}N$ MQDs. In each pair of the barrier and the QD layer, the thicknesses of the barrier is 7nm. Finally, a *p*-GaN layer is capping the structure. It is worth highlighting that such a structure is achievable under current growth techniques using metalorganic chemical vapor deposition (MOCVD), although it's a great challenge to obtain a high In content with device performance.

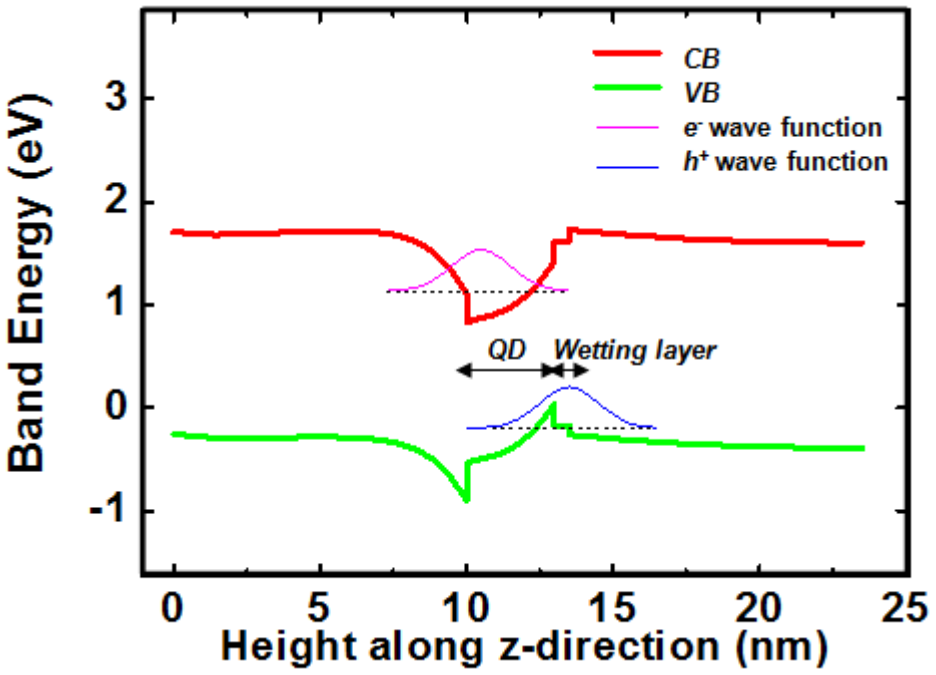

Figure 6.2 The calculated quantum dot band structure. The electron wave function and the hole wave function inside the quantum dot are displayed. The dotted lines indicate the first eigenstate of electrons and holes in the quantum dot.

Figure 6.2 provides the calculated QD band structure considering the piezoelectric strain along the growth direction. The absolute value in the x-axis in Figure 6.2 does not have a concrete meaning, but it indicates the height of the wetting layer (0.5nm) and the QD (3nm). The wetting layer and the $In_{0.8}Ga_{0.2}N$ QD have been marked in the figure and the rest is the $In_{0.4}Ga_{0.6}N$ barrier. The electron and hole wave functions have also been marked in the band structure. It is found that the holes are accumulated at the bottom of the quantum dot and are close to the wetting layer, while the electrons are close to the top of the quantum dot, which is consistent with previous research [13].

6.2. Theories of the piezoelectric effect on quantum dot solar cells

6.2.1 Influences of piezoelectric charges on the built-in potential

Wurtzite GaN is the typical piezoelectric semiconductor material. The piezoelectric potential is formed at the interface of the $In_xGa_{1-x}N/In_yGa_{1-y}N$ alloys, x and y representing different Indium composition. The piezoelectric effect has long been discussed in growth and fabrication of nitride materials and devices. However, only recently, the concept of the so-called piezo-photontronics effect has been raised by Wang Z.L.'s group in Georgia Institute of Technology[4,5,14], Note that the solar cell performance depends on several factors including the photon generated current density, the open-circuit voltage and the filling factor. The piezo-phototronic effect has recently been suggested to improve the open-circuit voltage and hence the solar cell performance. Such an effect is essentially employing the piezoelectric field in tuning the carrier separation, transport and recombination process at either the p-n junction or the metal-semiconductor contact. It is well known that wurtzite GaN is a typical piezoelectric material with a strong piezoelectric field at the interfaces. It is hence suggested that the InGaN QD based solar cell structure could potentially employ the advantages of both the IBSC structure and the piezoelectric field.

The theories of the piezoelectric potential originates from the Poisson equations which has been given in Equation (6.1): $\nabla^2\varphi = -\frac{\rho}{\varepsilon_s}$ and the charge density distribution $\rho(x)$ satisfies: $-\rho(x) = e[-n(x) + p(x) + N_D(x) - N_A(x) + \rho_{piezo}(x)]$. The extra charge density due to the piezoelectric polarization labelled as $\rho_{piezo}(x)$ has been taken into consideration in calculating the band structure in Section 6.1.2. On the other hand, the influence of $\rho_{piezo}(x)$ on the built-in potential and the open-circuit voltage will be studied in this section.

Figure 6.3.a illustrates a common p-n junction with the piezoelectric field arising from the compressive strain. The strain across the QDs leads to the piezoelectric fields along the same direction as the built-in electric field of the p-n junction for the *n*-type semiconductor[4]. This is also proved by the theoretical calculation results which have suggested that the holes are accumulated at the bottom of the quantum dot and are close to the wetting layer, while the electrons are close to the top of the QD[13]. Figure 6.3.b illustrates the charge distribution across the junction. The extra piezoelectric charge is distributed on the *n*-type depletion layer. Figure 6.3.c plots the enhancement of the built-in potential due to the piezoelectric field. Figure 6.3.c illustrates a stronger built-in potential due to the piezoelectric field.

The mechanism of the influence of the piezoelectric field on the built-in potential is studied. The electric field is the integration of the electric charges described in Figure 6.3.b. and the potential distribution is the integration of the electric field. As a consequence, the potential distribution $\varphi_i(z)$ double integrates the charges along z direction according to Equation (6.1) and the built-in potential φ_{bi} refers to the potential across the whole junction.

The potential distribution $\varphi_i(z)$ is analyzed differently in the three regions, as plotted in Figure 6.3.b of the charge distribution. The three regions are: $0 \le z \le l_{Dp}$, $l_{Dp} \le z \le l_{Dp} + W_{piezo}$ and $l_{Dp} + W_{piezo} \le z \le l_{Dp} + l_{Dn}$. In the following derivations: l_{Dp} and l_{Dn} are the length of the depletion region on the *p*-type and *n*-type side respectively. W_{piezo} is the width of charges region induced by the piezoelectric field induced at the interface of a p–n junction. In practical calculation, it is reasonable to regard W_{piezo} as the QD layer thickness or the height of the QDs.

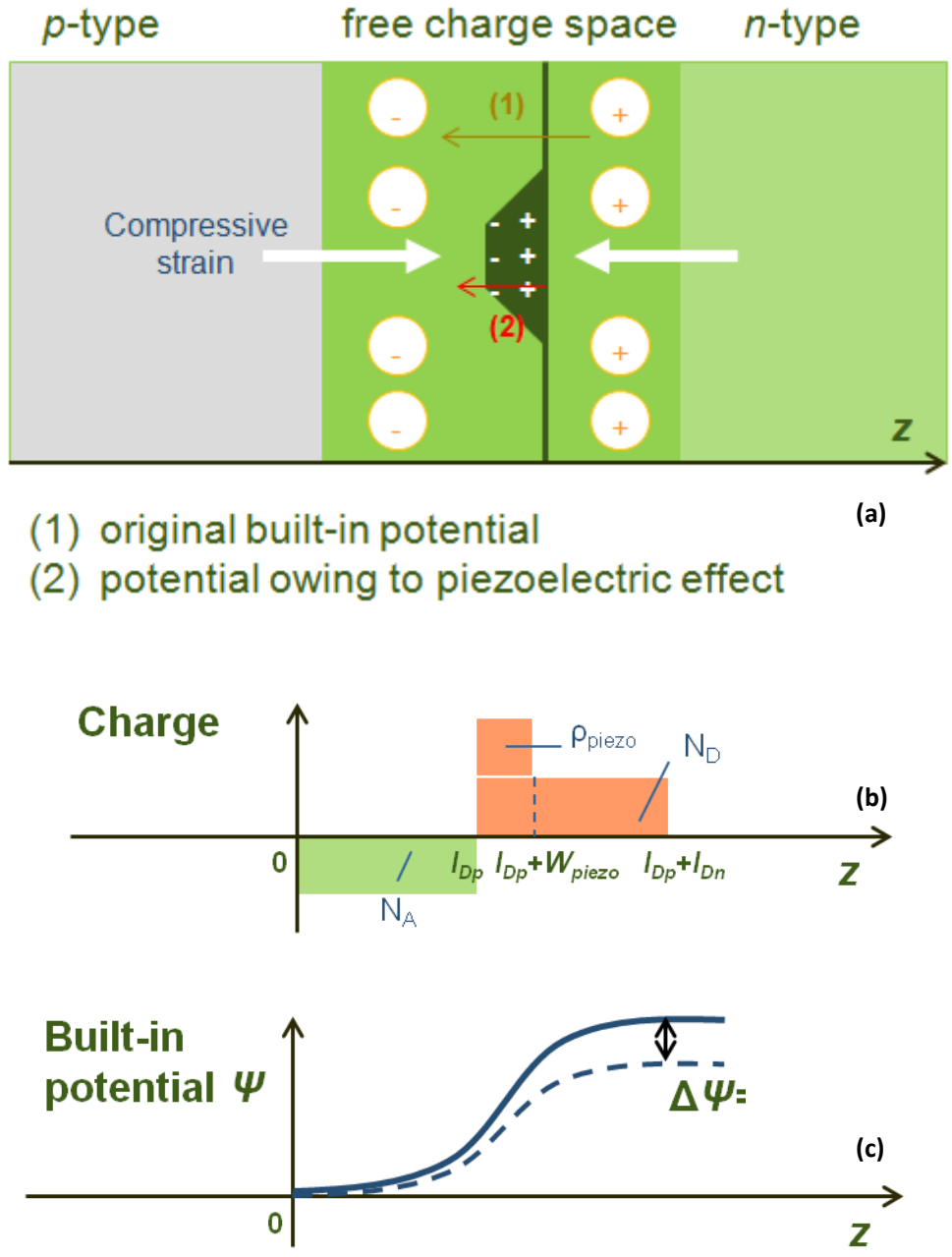

Figure 6.3 Schematic diagram of (a) the electric fields (b) the charges and (c) the built-in potential across the p-n junction of the solar cell. In (c), the solid line corresponds to the situation when the piezoelectric fields are considered, while the dashed line corresponds to the situation where the piezoelectric fields are not considered.

(a) when $0 \le z \le l_{Dp}$, there only exists N_A :

$$\varphi_i(z) = \frac{qN_A z^2}{2\varepsilon_S} \quad (6.3.a)$$

(b) When $l_{Dp} \le z \le l_{Dp} + W_{piezo}$, there exists both N_D and piezoelectric charges ρ_{piezo} :

$$\varphi_i(z) = \varphi_i(l_{Dp}) + \frac{qN_D}{\varepsilon_S}[l_{Dn}(z - l_{Dp}) - \frac{(z-l_{Dp})^2}{2}] + \frac{q\rho_{piezo}}{\varepsilon_S}[W_{piezo}(z - l_{Dp}) - \frac{(z-l_{Dp})^2}{2}] \quad (6.3.b)$$

(c) When $l_{Dp} + W_{piezo} \le z \le l_{Dp} + l_{Dn}$, there only exists N_D :

$$\varphi_i(z) = \varphi_i(l_{Dp} + W_{piezo}) - \frac{qN_D}{\varepsilon_S}[l_{Dn}W_{piezo} - \frac{W_{piezo}^2}{2}] + \frac{qN_D}{\varepsilon_S}[l_{Dn}(z - l_{Dp}) - \frac{(z-l_{Dp})^2}{2}] \quad (6.3.c)$$

Therefore, when z= $l_{Dp} + l_{Dn}$, $\varphi_i(z) = \varphi_{bi}$. The built-in potential with and without the piezoelectric fields satisfies Equations (6.4.a) and (6.4.b) respectively:

$$\varphi_{bi} = -\frac{q}{2\varepsilon_S}(N_D l_{Dn}^2 + N_A l_{Dp}^2) \quad (6.4.a)$$

$$\varphi_{bi} = -\frac{q}{2\varepsilon_S}(N_D l_{Dn}^2 + \rho_{piezo} W_{piezo}^2 + N_A l_{Dp}^2) \quad (6.4.b)$$

Therefore there is an extra term in the built-in potential owing to the piezoelectric field [4]. Even though the change of the built-in potential is not directly linked to the solar cell performance, it causes the change the open-circuit voltage of the solar cells.

6.2.2 Influences of piezoelectric charges on the open circuit voltage

The increased built-in potential lowers down the Fermi level and affects the reverse saturation current density. Consequently, the open circuit voltage V_{oc} is enhanced in the presence of the piezoelectric field.

From the basics mechanism of solar cells, the conversion efficiency of solar cells, η, is defined as the ratio of output solar power P_{out} and the input solar cell power P_i, and P_{out} is the product of the fill factor FF, the open-circuit voltage V_{oc} and the

short-circuit current density J_{sc}. The current density J satisfies: $J = J_{sc} - J_0(e^{V/K_BT} - 1)$. V_{oc} is the voltage solved when $J = 0$.

Here, J_0, the reverse saturation current density in solar cell current-voltage functions can be expressed by Equation (6.5) [15] :

$$J_0 = qN_C N_V \left(\frac{D_n}{N_A L_n} + \frac{D_p}{N_D L_p}\right) \exp\left(-\frac{E_g}{K_B T}\right) \tag{6.5.a}$$

$$\text{Or} \quad J_0 = \frac{qn_i^2 D_n}{N_A L_n} + \frac{qn_i^2 D_p}{N_D L_p} = \frac{qD_n n_{p0}}{L_n} + \frac{qD_p p_{n0}}{L_p} \tag{6.5.b}$$

Where N_c and N_v are the effective density of states in conduction band and valence band, respectively; N_A and N_D are the doping level for p-layer and n-layer, respectively; D_n and D_p are the diffusion coefficients of electrons and holes, respectively; and L_n and L_p are the diffusion length of electrons and holes, respectively. n_{p0} and p_{n0} are the thermal equilibrium electron concentration in the *p*-type semiconductor and the thermal equilibrium hole concentration in the *p*-type semiconductor respectively. Since the diffusion coefficient *Dn* is much larger than *Dp*, while other parameters in *n*-type and *p*-type semiconductors are comparable, $\frac{qD_n n_{p0}}{L_n}$ is normally 2-3 magnitudes larger than $\frac{qD_p p_{n0}}{L_p}$ according to the numerical calculation. The expression for J_0 can be approximated as:

$$J_0 \approx \frac{qD_n n_{p0}}{L_n} = \frac{qD_n n_i}{L_n} \exp\left(-\frac{E_i - E_F}{K_B T}\right) \tag{6.6}$$

where *Ei* is the intrinsic Fermi level which follows: $E_i = E_c - E_g/2$, and E_F is the Fermi level under the doping conditions. Due to the piezoelectric fields, the built-in potential has been increased by $\frac{q\rho_{piezo} W_{piezo}^2}{2\varepsilon_0 \varepsilon_r K_B T}$, lowering the Fermi level down by the same value. Consequently, the new Fermi level considering the piezoelectric fields becomes:

$$E_F^{'} = E_F - \frac{q\ \rho_{piezo} W_{piezo}^2}{2\varepsilon_s} \tag{6.7}$$

Combining Equation (6.6), the reverse saturation current density $J_0^{'}$ which considers the effect of piezoelectric field becomes:

$$J_0^{'} = \frac{qD_n n_i}{L_n} \exp(-\frac{E_i - E_F^{'}}{K_B T}) = J_0 \exp(-\frac{q^2 \rho_{piezo} W_{piezo}^2}{2\varepsilon_s K_B T}) \quad (6.8)$$

Substituting J_0' by J_0, the open circuit voltageV_{oc}' which considers the piezoelectric fields can then be described by Equation (6.9) [4]:

$$V_{oc}^{'} \approx \frac{K_B T}{q} \ln(\frac{J_{SC}}{J_0^{'}}) = \frac{K_B T}{q} \{\ln(\frac{J_{SC}}{J_o}) + \frac{q^2 \rho_{piezo} W_{piezo}^2}{2\varepsilon_s K_B T})\} \quad (6.9)$$

Comparing to the original $V_{oc,}$ namely, the open-circuit voltage in the absence of the piezoelectric field, V'_{oc} has an extra term caused by the piezoelectric field with its value by $\frac{q\rho_{piezo} W_{piezo}^2}{2\varepsilon_s}$. ρ_{piezo}, the piezoelectric charge density, satisfies: $\rho_{pizeo} = \frac{|P_{pz}|}{W_{pizeo}}$. This is obtained by manipulating $\rho_{piezo} = -\nabla p_{pz} = -\frac{\partial p_{pz}}{\partial Z}$, where p_{pz} is the value for the piezoelectric polarization which can be calculated using Equation (2.3). For the $In_{0.8}Ga_{0.2}N$ (QD)/ $In_{0.4}Ga_{0.6}N$ (Barrier) structure with the height of the QD (W_{piezo}) as 3nm, the value of $\frac{q\rho_{piezo} W_{piezo}^2}{2\varepsilon_s}$ is calculated as 0.274eV. This indicates that the piezoelectric field has caused an increase of 0.274eV of the open-circuit voltage for this optimized InGaN QD IBSC structure.

6.3. Theoretical modelling of solar cell conversion efficiencies for InGaN QD-IBSCs

6.3.1 Current-voltage functions for InGaN QD-IBSCs

This section shows the method for calculating the short-circuit current density J_{sc} from the solar spectrum, and the method of calculating the open-circuit voltage V_{oc} and the solar cell conversion efficiency from the current-voltage function for a p-n junction. Note that that V_{oc} is firstly calculated without considering the piezoelectric

field, and then the additional value caused by the piezoelectric field as calculated in Section 6.2 is added to V_{oc} and the real open-circuit voltage is worked out for the InGaN QD-IBSC.

For intermediate band solar cell (IBSC) devices, it follows the current-voltage equations for conventional solar cells[16] and it has an enhanced short-circuit current density, i.e., the photon-generated current density, due to the multiple level absorption of photons within a single junction.

For the intermediate band (IB), it is in a dynamic process of the carrier generation and recombination. Since no carrier is taken out from any of the IBs, the photon fluxes of G_{IV} (generation rate) and R_{IV} (recombination rate) satisfies: $(G_{IV} - R_{IV}) - (G_{IC} - R_{IC}) = 0$. G_{IV} refers to the generation rate between *VB* and *IB*, while G_{IC} refers to the generation rate between *IB* and *CB*. J_{sc}, the photon-generated current density which is usually regarded as the short-circuit current density, is obtained from: $J_{sc}/q = G_{CV} + (G_{IV} - R_{IV}) = G_{CV} + (G_{IC} - R_{IC})$.

Based on the detailed balanced limit model[1], it has been found that the net photon flux from the intermediate band, $G_{IV} - R_{IV}$, almost equals to the smaller of G_{IV} and G_{IC}, e.g. $\min(G_{IV}, G_{IC})$. If G_{IV} is smaller than G_{IC}, then R_{IV} is adjusted to be as small as possible (up to 6-7 magnitudes smaller than G_{IV}), while R_{IC} equals to the remainder of G_{IC} and G_{IV}; vise versa. This is realized by self-adjustment of the quasi-Fermi level for the intermediate band. The expression for J_{sc} then becomes:

$$J_{sc}/q = G_{CV} + \min(G_{IV}, G_{IC}) \tag{6.10}$$

In addition, the Beer–Lambert law requires the absorption coefficient α to be incorporated into the function of the generation rate: $G = \int Q(E)[1 - \exp(-\alpha(E)d)]dE$.[15]

where d is the thickness of the absorption layer and Q(E) is the quantity of photons at this energy level which is retrieved from the AM 1.5 database by American Society for Testing and Materials (ASTM)[17]. Under the category “Direct+

circumsolar" of ASTM G173-03 Reference Spectra, the incident power density is 1000 W*m^{-2}. The absorption coefficient for quantum dots can be estimated by the value for the bulk material[18,19] during the calculation process. The Matlab commands for calculating J_{sc} are provided in Appendix II.

When J_{sc} is known, V_{oc} without considering the piezoelectric field can be obtained from the current-voltage equations for a typical p-n junction:

$$J = J_{sc} - J_0(e^{V/K_BT} - 1) \tag{6.11}$$

V_{oc} is the value of V when J=0 in Equation (6.11). J_0 is the reverse saturation current density. J_0 without considering the influence of the piezoelectric field has been given in Equation(6.5.a): $J_0 = qN_C N_V (\frac{D_n}{N_A L_n} + \frac{D_p}{N_D L_p}) \exp(-\frac{E_g}{K_B T})$. The values for these parameters are calculated as following[15]:

N_c(/10^{19}cm^{-3}) = 2.3-1.4x; N_v(/10^{19}cm^{-3})= 1.8+3.5x; D_n (cm^2/s) =39+41x; D_p(cm^2/s) =0.75+0.25x; L_n(/10^{-4}cm) =0.866+0.134x; L_p(/10^{-4}cm) = 6.24+2.7x

where x is the Indium composition. In addition, the donor and acceptor doping levels in *n*-layer and *p*-layer, labelled N_A and N_D, are assumed to be 10^{18} cm^{-3} and 10^{17} cm^{-3}, respectively.

In order to obtain V_m, the voltage leading to the maximum output power, there is: $dP/dV = d(JV)/dV = 0$. Combining this and Equation (6.11), V_m is the numerical solution of the following equation: $\exp(\frac{V_{oc}}{V_c}) = (\frac{V+V_c}{V_c}) \exp(\frac{V}{V_c})$ [15], where V_c = K_BT. When V_m is known, J_m, the current density leading to the maximum output power, is obtained by solving Equation (6.11). The filling factor *FF* can be solved based on the definition of the solar cell conversion efficiency. When there is the piezoelectric field, the values for $V_{m,}$, J_m and *FF* changes slightly owing to the difference in J_0 (Equation (6.8)). More importantly, V_{oc} is increased by the value calculated in Section 6.2.

6.3.2 Conversion efficiency for InGaN QD-IBSCs

As has been calculated in Section 6.2.2, the open-circuit voltage for the optimized $In_{0.8}Ga_{0.2}N$ (QD)/$In_{0.4}Ga_{0.6}N$(Barrier) structure is enhanced by 0.274eV when the piezoelectric field exists. The detailed calculation results on the optimized QD IBSC structure (which is not self-organized but formed in the designed size as suggested in Section 6.2.2) consisting of 10 periods of QD layers are provided in Table 6.2.

Table 6.2 The calculated short-circuit current density J_{sc}, open-circuit voltage V_{oc}, maximum current density J_m and voltage V_m, filling factor FF, and solar cell conversion efficiency η on the IBSC structure with 10 periods of QD layers

Photon-generated current density from barrier $J_{sc\text{-}barrier}$ (A/m^2)	121.8
Photon-generated current density from QD $J_{sc\text{-}QD}$ (A/m^2)	149.4
Short-circuit current density J_{sc} (A/m^2)	271.2
Saturation current density J_0 (A/m^2)	1.08×10^{-26}
Open circuit voltage V_{oc} (V) in the absence of ρ_{piezo}	1.426
Open circuit voltage V_{oc}'(V) considering ρ_{piezo}	1.700
Max power corresponded voltage V_m (V)	1.593
Corresponded current density J_m (A/m^2)	266.8
Filling factor FF (%)	91.2
Conversion Efficiency η (%)	42.5

Table 6.2 shows that a conversion efficiency of 42.5% can be obtained for the IBSC with 10 periods of QDs. The conversion efficiency is attributed to the extra photon-generated current density from the QD and the enhanced open circuit voltage of 0.274V. Without considering the piezoelectric effect the efficiency is 35.2%, about 20% lower.

The conversion efficiency is then calculated as a function of the number of periods

of the $In_{0.8}Ga_{0.2}N$ (QD)/$In_{0.4}Ga_{0.6}N$(Barrier) structure, which is given in Figure 6.4. The conversion efficiency tends to be saturated when the number of periods is above 50, and it reaches a maximum conversion efficiency of 55.4%, since the absorption for the photon-generated current density becomes 100%. Without considering the piezoelectric field, the maximum conversion efficiency is 46.0%. The existence of the piezoelectric field further pushes up the efficiency limit. The results presented pave the way for the fabrication of InGaN based solar cells with ultra solar cell conversion efficiencies.

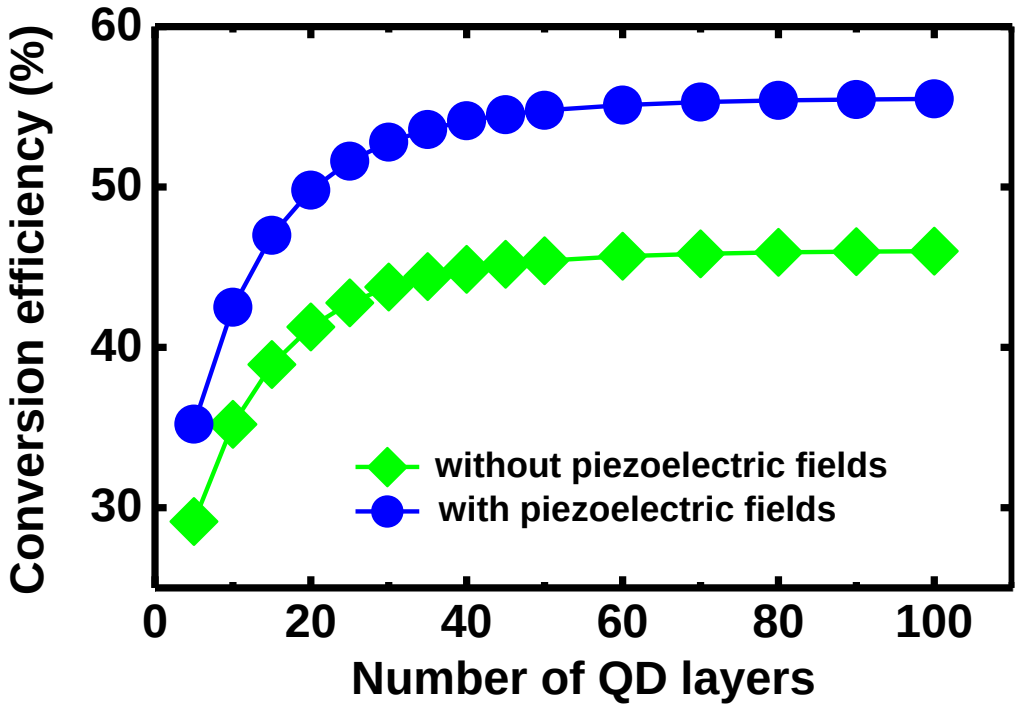

Figure 6.4 Calculated conversion efficiency of the designed InGaN QD-IBSCs (single IB) as a function of the number of QD layers.

As has been mentioned in earlier context, the intermediate bands can also be formed by transition metal doping. The most common transition metal for InGaN-based IBSC is Mn[20]. One problem with Mn-doping InGaN IBSC is that, the energy of the Mn–introduced IB is dependent on the Indium content of the InGaN layer. Under the universal IBSC model, the IB energy can be set arbitrarily for an optimized value, while in the Mn-doped IBSC, the IB energy is set once the InGaN matrix energy is

known[20]. Consequently, the optimized Mn-doped InGaN IBSC has a conversion efficiency 10% lower than the predicted efficiency limit.

Therefore, in terms of the theoretical efficiency limit, the quantum dot IBSC is more favorable comparing with the Mn-doped IBSC. The quantum dot system provides more flexibilities of the energy band levels by varying the sizes and shapes of quantum dots. The IB energy in QD IBSC is hence not fixed when the InGaN band matrix energy is known.

For the multiple-level IBSC, both quantum dot IBSC and the Mn-doped IBSC face a lot of difficulties and presently are limited in theoretical research only. For the Mn-doped IBSC, a two band doping has been raised in Si-based solar cell by doping sulphur (S) and selenium (Se)[21]. For the GaN based QD IBSC, the QD-in-nanowire[22] structure provides possibilities in future experimental research of multi-level QD-IBSCs. There's still a long way to explore the multiple-level IBSC for GaN-based materials.

6.4. Summary

In summary, the InGaN based quantum dot intermediate band solar cell (QD-IBSCs) take advantages of two favorable properties, the IBSC structure and the piezoelectric field. The IBSC structure enhances the solar cell performances by providing an extra level of absorption and this directly increases the short circuit current density. The QD structure outweighs other low dimensional structures (e.g. QW and Quantum wire) because of the special phonon bottleneck effect in QDs. In the QW structure, electrons can easily relax from CB to IB. However, in the QD structure, the discontinuity of the density of states enables the separation of the intermediate band (IB) and conduction band (CB).

The piezoelectric field exists in the InGaN QD structure and it is in the same direction with the built-in potential across the p-n junction. The piezoelectric charge

is on the *n*-type side and according to the Poisson equation, the built-in potential double integrates the charges. The extra piezoelectric charge increases the value of the built-in potential. Since the increased built-in potential directly lowers down the Fermi-level on the *n* side, the reverse saturation current density that is closely associated with the Fermi level is affected. In the current-voltage functions of solar cells, the open circuit voltage is hence increased.

The optimal InGaN QD-IBSC structure is designed, for which the intersubband transitions can be effectively used as an IB for solar cells. The conversion efficiency, the open-circuit voltage and short-circuit current have been calculated on the designed structure considering the piezoelectric potential. For the $In_{0.4}Ga_{0.6}N$/ $In_{0.8}Ga_{0.2}N$ QD single-IB solar cell, the highest conversion efficiency obtained is 55.4%. The inspiring results on conversion efficiencies pave the way for the fabrication of InGaN based solar cells with ultra high conversion efficiencies.

Reference

[1] Luque, A., & Martí, A. (1997). Increasing the efficiency of ideal solar cells by photon induced transitions at intermediate levels. *Phys. Rev. Lett.*,78(26):5014-5016

[2] Martí, A., López, N., Antolin, E., Canovas, E., Stanley, C., Farmer, C., & Luque, A. (2006). Novel semiconductor solar cell structures: The quantum dot intermediate band solar cell. *Thin Solid Films*, 511: 638-644

[3] Cuadra, L., Martí, A., López, N., & Luque, A. (2004, September). Phonon bottleneck effect and photon absorption in self-ordered quantum dot intermédiate band solar cells. In *Proc. of the 19th European Photovoltaic Solar Energy Conference* , pp, 250-254

[4] Zhang, Y., Liu, Y., & Wang, Z. L. (2011). Fundamental theory of piezotronics.

Adv. Mater., 23(27): 3004-3013

[5] Zhang, Y., Yang, Y., & Wang, Z. L. (2012). Piezo-phototronics effect on nano/microwire solar cells. *Energy & Environmental Science*, 5(5): 6850-6856

[6] Chuang, S. L., & Chang, C. S. (1996). k· p method for strained wurtzite semiconductors. *Phys. Rev. B*, 54(4): 2491-2497

[7] Birner, S. (2011). *Modeling of Semiconductor Nanostructures and Semiconductor -electrolyte Interfaces*. Verein zur Förderung des Walter-Schottky-Inst. der Techn. Univ. München.

[8] Luttinger, J. M., & Kohn, W. (1955). Motion of electrons and holes in perturbed periodic fields. *Phys.Rev.*, 97(4): 869-875

[9] Kane, E. O. (1957). Band structure of indium antimonide. *J. Phys. Chem. Solids*, 1(4): 249-261

[10] Vurgaftman, I., & Meyer, J. R. (2003). Band parameters for nitrogen-containing semiconductors. *J. Appl. Phys.*, 94(6):3675-3696

[11] Zhao, H., Arif, R. A., & Tansu, N. (2009). Design analysis of staggered InGaN quantum wells light-emitting diodes at 500–540 nm. *Selected Topics in Quantum Electronics, IEEE Journal of*, 15(4):1104-1114

[12] Wu, J., Walukiewicz, W., Yu, K. M., Ager III, J. W., Haller, E. E., Lu, H., & Schaff, W. J. (2002). Small band gap bowing in InGaN alloys. *Appl. Phys. Lett.*, 80: 4741-4743

[13] Fonoberov, V. A., & Balandin, A. A. (2004, January). Optical Properties of Wurtzite GaN and ZnO Quantum Dots. In *MRS Proceedings* .818:M8-2-M8-4. Cambridge University Press

[14] Wang, Z.L. (2010) Piezopotential Gated Nanowire Devices: Piezotronics and Piezo-phototronics. *Nano Today*, 5: 540-552

[15] Wen, B, Zhou, J.J, Jiang, R. L, … & Zheng. Y.D. (2007). Theoretical calculation of conversion efficiency of InGaN solar cells. *Chin. J. Semicond.* 28: 1392-1936

[16] Shockley, W., & Queisser, H. J. (1961). Detailed balance limit of efficiency of p-n junction solar cells. *J. Appl. Phys.*, 32(3): 510-519

[17] AM 1.5 Solar spectrum. Retrieved from: http://rredc.nrel.gov/solar/spectra/am1.5/

[18] Geyter, B.D, & Hens, Z. (2010). The absorption coefficient of PbSe/CdSe core/shell colloidal quantum dots. *Appl.Phys. Lett.*, *97*(16), 161908-161911

[19] Jani, O. K. (2008). Development of Wide-Band Gap InGaN Solar Cells for High-Efficiency Photovoltaics, pp. 80. Ph.D. thesis, Georgia Institute of Technology, Atlanta, Georgia

[20] Mart ί, A., Tablero, C., Antol ń, E., Luque, A., Campion, R. P., Novikov, S. V., & Foxon, C. T. (2009). Potential of Mn doped $In_{1-x}Ga_xN$ for implementing intermediate band solar cells. *Solar Energy Mater. Solar Cells*, 93(5): 641-644

[21] He, H., Chen, C., & Liu, S. (2012). Microstructured silicon with two impurity bands for solar cells. *J. Appl. Phys.*, 111(4): 043102-043105

[22] Nozawa, T., & Arakawa, Y. (2013). Theoretical analysis of multilevel intermediate-band solar cells using a drift diffusion model. *J. Appl. Phys.*, *113*(24): 243102-243105

7. Conclusion and future work

The III-nitrides has been a promising material with wide application in opto-electronic devices, including light-emitting diodes (LEDs), laser diodes and solar cells. For all the devices, however, they face the fundamental issues of how to improve their working efficiency. This has been the main theme for this research, with a concern of the efficiency and an approach from fundamental mechanisms of the III-nitride nanostructures.

The nanorod structures have been found to relieve the quantum-confined-stark effect (QCSE) and reduce the electron-longitudinal-optical phonon coupling strength which is reflected by the Huang-Rhys Factor. Since the phonon assisted indirect Auger recombination has been regarded as a major cause of the efficiency droop, smaller indirect Auger recombination and an attenuated droop could be realized in nanorod LEDs. In future work, more factors could be considered to explain the effect of nanorod structures on PL emission including the strain, the confinement of wavefunction and surface states, through designing relative experiments.

The surface plasmon–exciton coupling effect enhances the internal quantum efficiency and the coupling effect is found to be motivated by the exciton delocalization. The SP-exciton coupling, which is essentially a dipole-dipole coupling, only has a high coupling rate at a certain range of the in-plane wave number. The localized excitons have a wavefunction with its mean value at zero in the *k*-space, leading to a very low coupling rate. The delocalized excitons can easily gain adequate momentum and their wave number corresponds to a high coupling rate. A further increase of temperature leads to a higher wave number that exceeds the optimal range, and then lowers down the coupling rate. Such a dipole-dipole coupling mechanism is worth to be further researched. Future work can involve

varying the capping layer thickness and the coupling rate would have a different relationship on the in-plane wave number. This would render a more systematic study of the exciton-SP coupling for InGaN LEDs.

The theoretical work on the whispering gallery mode ring cavity structures suggests the ideal radius for the ring cavities is 1000-1500nm, where the Q-factor can reach 1×10^6 at the blue and green spectrum (400-500nm). The mode splitting effect with the separation of bonding and anti-bonding modes has been observed in a pair of adjacent rings. A Q-factor 2-3 times higher can be realized when edges of two ring is 25-50nm apart, while the Q-factor degrades when the two rings are in different sizes. Future work regarding to InGaN ring cavities could take into consideration of the InGaN properties, for instance, whether the strain of the InGaN layer would affect the cavity properties.

InGaN QD solar cells take advantages of both the intermediate band solar cell (IBSC) structure and the prominent piezoelectric field in III-nitrides. By optimizing the structure, InGaN QD-IBSC reaches the highest conversion efficiency of 55.4%. In future work of InGaN QD solar cells, the InGaN QD-IBSC with multiple intermediate bands can be researched, which can potentially produce higher conversion efficiencies. The InGaN QD structures pave the way for the fabrication of InGaN based solar cells with ultra high conversion efficiency.

In conclusion, the structures including nanorods, surface plasmon coating, whispering gallery mode cavities and intermediate band solar cell have been studied for the InGaN-based LEDs, laser diodes or solar cells. Further application of these structures would contribute to a better performance of the III-nitride nanostructures and opto-electronic devices.

Appendix

Appendix I

MEEP commands for FDTD calculation on InGaN ring cavities

```
(define-param eps 5.35) ;dielectric constant of GaN
(define-param r 1.0 ) ; external ring radius(μm)
(define-param d 0.05) ; ring distance(μm)

(define-param pad 1) ; padding between waveguide and edge of PML
(define-param dpml 1) ; thickness of PML

(define sy (* 2 (+ r pad dpml))) ; cell size on y
(define sx (* 2 (+ r r r pad dpml))); cell size on x
(set! geometry-lattice (make lattice (size sx sy no-size))) ;2D structure

(set! geometry (list
      (make cylinder (center 0 0) (height infinity)
             (radius r) (material (make dielectric (epsilon eps)) ))
     (make cylinder (center 0 0) (height infinity)
             (radius (- r 0.1)) (material air))   ; define the first ring

      (make cylinder (center (+ r r d) 0) (height infinity)
            (radius r) (material (make dielectric (epsilon eps)) ))
      (make cylinder (center (+ r r d) 0) (height infinity)
            (radius (- r 0.1)) (material air))))  ;define the second ring

(set! pml-layers (list (make pml (thickness dpml))))
(set-param! resolution 50)

(define-param fcen 2.3) ; pulse center frequency
(define-param df 0.1)  ; pulse width (in frequency)
(define-param nfreq 500); number of frequencies to compute

(set! sources (list
             (make source
               (src (make gaussian-src (frequency fcen) (fwidth df) ))
               (component Ez) (center (- r 0.05) 0 ) )))
```

```
; A single point source is put at some arbitrary place, and Ez(E out of
; the plane)in the TM modes is studied.

(set! symmetries (list (make mirror-sym (direction Y))))

(define trans (add-flux fcen df nfreq (make flux-region (center (* r 1.1)
0 ) (size 0 (* r 2.2)) )))

(run-sources+ 300
         (at-beginning output-epsilon)
         (after-sources (harminv Ez (vector3 (- r 0.05) 0) fcen df)))

(run-until (/ 1 fcen) (at-every (/ 1 fcen 20) output-efield-z))

(display-fluxes trans) ; print out the flux spectrum

; meep ring-xvarysize-ar750-1.ctl | tee ring-xvarysize-ar750-1.out

unix%  meep fcen=2.30 df=0.05 ring-xvarysize.ctl

unix%h5topng -RZc dkbluered -C ring-xvarysize-ar750-1-eps-000000.00.h5
ring-xvarysize-ar750-1-ez-*.h5 ; Export the field to graphs

unix% convert ring-nm-ez-*.png ring-nm-ez-3.125.gif
```

Note:

The words after ";" are the explanations for the commands, as defined by MEEP.

Calculated whispering gallery mode eigenvalues with a resonance wavelength (λ_R) around 430nm, 460nm and 490nm

Radius (nm)	Mode Number *m*	Angular Frequency (PHz) Re(ω)	Im(ω)	Quality factor Q	Wavelength λ_R (nm)
250	6	4.4076	-1.0893E-02	2.02E+02	427.66
500	13	4.3844	-3.2377E-05	6.77E+04	429.92
750	20	4.3586	-3.8463E-06	5.67E+05	432.47
1000	27	4.3461	-2.2241E-06	9.77E+05	433.71
1500	41	4.3314	-1.8149E-06	1.19E+06	435.18
2000	55	4.3237	-2.1455E-06	1.01E+06	435.96
3000	84	4.3565	-4.6349E-06	4.70E+05	432.68
5000	141	4.3584	-8.3792E-07	2.60E+06	432.49
10000	283	4.3657	-2.4305E-06	8.98E+05	431.765

Radius (nm)	Mode Number *m*	Angular Frequency (PHz) Re(ω)	Im(ω)	Quality factor Q	Wavelength λ_R (nm)
500	12	4.1156	-8.7675E-05	2.29E+04	458.00
750	18	4.0108	-1.3648E-05	1.47E+05	469.97
1000	25	4.0904	-2.5102E-06	8.15E+05	460.83
1500	38	4.0807	-8.9002E-07	2.29E+06	461.92
2000	51	4.0741	-1.8804E-06	1.08E+06	462.66
3000	77	4.0683	-2.7773E-06	7.32E+05	463.33
5000	130	4.0638	-1.3777E-06	1.47E+06	463.84
10000	261	4.0598	-1.8421E-06	1.10E+06	464.30

Radius (nm)	Mode Number *m*	Angular Frequency (PHz) Re(ω)	Im(ω)	Quality factor Q	Wavelength λ_R (nm)
250	5	3.8136	-2.4127E-02	7.91E+01	494.27
500	11	3.8432	-2.2936E-04	8.38E+03	490.46
750	17	3.8349	-2.1023E-05	9.12E+04	491.52
1000	23	3.8319	-1.1451E-06	1.67E+06	491.91
1500	35	3.8257	-8.2067E-07	2.33E+06	492.71
2000	47	3.8221	-1.2988E-06	1.47E+06	493.17
3000	71	3.8185	-2.6900E-06	7.10E+05	493.63
5000	120	3.8155	-1.5098E-06	1.26E+06	494.02
10000	241	3.8127	-6.3619E-07	3.00E+06	494.39

Appendix II

Nextnano commands for calculation of the band structure for InGaN/GaN quantum dot intermediate band solar cells

```
!*************** OVERALL SIMULATION PARAMETERS*******************!
$simulation-dimension
 dimension   = 3
 orientation = 1 1 1
$end_simulation-dimension
!----------------------------------------------------------------!
$global-parameters
 lattice-temperature = 300.0d0                    ! in the unit of Kelvin
$end_global-parameters
!----------------------------------------------------------------!
$strain-minimization-model
boundary-condition-z       = Neumann  ! Neumann boundary condition
$end_strain-minimization-model
!----------------------------------------------------------------!
%FunctionParser = yes
%Width = 8e0                      ! width of the bottom hexagon of the QD
%Height  = 3e0                                    ! height of the QD
%Wetting  = 0.5e0                              ! wetting layer thickness
%Distance  = 10e0
%Boundary1 = %Distance*2 + %Width*2*0.865
%Boundary2 = %Distance*2 + %Width*2
%Boundary3 = %Distance*2 + %Wetting +%Height
%Boundary4 = %Distance + %Wetting
%Boundary5 = %Distance + %Width*2
%Boundary6 = %Distance + %Wetting+ %Height
%Boundary7 = %Boundary6 + 3
%Basex2 = %Distance+%Width*2*0.865
%Topx1 = %Distance+(%Width*0.75)*0.865
%Topx2 = %Distance+(%Width*1.25)*0.865
%Topy1 = %Distance+%Width*0.75
%Topy2 = %Distance+%Width*1.25
%Centerx = %Distance + %Width*0.865
%Centery = %Distance + %Width
!************ END OVERALL SIMULATION PARAMETERS ******************!

!************** REGIONS AND CLUSTERS *****************************!
```

```
$regions                                                              !
 region-number = 1   base-geometry = cuboid  region-priority = 1
x-coordinates         = 0.0d0 %Boundary1   ! InGaN barrier
 y-coordinates         = 0.0d0 %Boundary2
 z-coordinates         = 0.0d0 %Boundary3
 region-number = 2   base-geometry = cuboid  region-priority = 2
x-coordinates         = 0.0d0 %Boundary1    ! InGaN wetting layer
 y-coordinates         = 0.0d0 %Boundary2
 z-coordinates         = %Distance  %Boundary4
 region-number = 3  base-geometr =hexagonal-obelisk region-priority= 3
 base-coordinates ! InGaN hexagonal quantum dot
= %Distance  %Basex2 %Distance %Boundary5   %Boundary4 %Boundary4
top-coordinates  = %Topx1  %Topx2 %Topy1 %Topy2   %Boundary6 %Boundary6
$end_regions                                                          !
!---------------------------------------------------------------------!
$grid-specification !
 grid-type       =    1 1 1                !Define the grid for computing
 x-grid-lines    =    0d0 %Distance %Topx1 %Topx2 %Basex2 %Boundary1
 x-nodes         =     9         9     9      9    9
x-grid-factors  =      1d0 1d0 1d0 1d0 1d0             ! 0.50 nm
 y-grid-lines    = 0d0 %Distance %Topy1  %Topy2  %Boundary5  %Boundary2
 y-nodes         =      9         9     9      9    9
 y-grid-factors   =      1d0 1d0 1d0  1d0 1d0
 z-grid-lines
=0d0 %Distance %Boundary4 %Boundary6 %Boundary7 %Boundary3
 z-nodes         =      9         3      9            9     9
 z-grid-factors   =      1d0 1d0 1d0 1d0 1d0
$end_grid-specification
!---------------------------------------------------------------------!
$region-cluster
 cluster-number = 1    region-numbers = 1           !  matrix
 cluster-number = 2    region-numbers = 2           !  wetting layer
 cluster-number = 3    region-numbers = 3 4      !  hexagonal quantum dot
$end_region-cluster
!**************** END REGIONS AND CLUSTER ***************************!

!******************* MATERIALS AND ALLOY PROFILES********************!
$material
material-number = 1
 material-name   = In(x)Ga(1-x)N                  ! Define the material
 cluster-numbers = 1
 alloy-function  = constant
```

```
 material-number = 2
 material-name   = In(x)Ga(1-x)N
 cluster-numbers = 2
 alloy-function  = constant
 material-number = 3
 material-name   = In(x)Ga(1-x)N
 cluster-numbers = 3
 alloy-function  = constant
$end_material
!---------------------------------------------------------------------!
$alloy-function
 material-number = 1                                  ! Define In content
 function-name   = constant
 xalloy          = 0.4d0
material-number = 2
 function-name   = constant
 xalloy          = 0.8d0
 material-number = 3
 function-name   = constant
 xalloy          = 0.8d0
$end_alloy-function
!---------------------------------------------------------------------!
$ternary-wz-default
 ternary-type                    = In(x)Ga(1-x)N-wz-default
apply-to-material-numbers          = 1 2 3
binary(x)                        = InN-wz-default
 binary(1-x)                     = GaN-wz-default
 bow-conduction-band-energies    = 1.43d0  0d0 0d0 ! Bowing factor=1.43
$end_ternary-wz-default
!***************** END MATERIALS AND ALLOY PROFILES *****************!

!**********************QUANTUM REGIONS*****************************!
$quantum-regions
 region-number         = 1                ! define the active region
base-geometry         = hexagonal-obelisk
 region-priority       = 1
$end_quantum-regions
!******************** END QUANTUM REGIONS ***************************!

!************************ OUTPUT ***********************************!
$output-bandstructure
destination-directory     = band_struc1/
```

```
 conduction-band-numbers  = 1
valence-band-numbers      = 1 2 3 !heavy hole, light hole, split-off hole
 potential                = yes
$end_output-bandstructure
!---------------------------------------------------------------------!
$output-densities
destination-directory               = densities1/
 piezo-electricity                  = yes
$end_output-densities
!---------------------------------------------------------------------!
$output-kp-data
 destination-directory               = kp_data1/
$end_output-kp-data
!********************** END OUTPUT *******************************!
```

Note:

The words after "!" are the explanations for the commands, as defined by Nextnano. The material parameters of InN and GaN have been listed in Table 6.1. For simplicity, the relevant commands are not provided here.

Matlab commands for calculation of the solar cell current density

```
function[RT] = am15(Em0, Em1)
% read the datasheet of the AM1.5 spectrum
   B = xlsread('C:\solar cell modeling database\AM15');
[Row Col] = size(B);
AM = zeros(Row, 2);
for i = 1:Row
    AM (i,1) = B(i,1);
    AM (i,2) = B(i,2);
end
E0 = 1243.1/Em1;
E1 = 1243.1/Em0;

% Find the starting data point
if 1243.1/Em1 <= 280
    k = 1;
end
for i = 1: Row
    if E0 <= AM(i,1)
      break
    end
    k = i;
```

```
end
% disp (k);
QI = zeros(Row-k+1,2);
for p = k: Row
    q = p-(k-1);    QI(q,2)= AM(p,2);
    QI(q,1)= AM(p,1);
end

%Find the ending data point
for q = 2: (Row-k+1)
    if E1 <= QI(q,1)
      break
    end
     n = q;
end
% disp (n);
 nf = n;
Q = zeros(nf,2);
for i = 1: nf
   Q(i,1)= QI(i,1);  Q(i,2)= QI(i,2);
end
%Q(n+1,1) = E1;  %Q(n+1,2) = Q(n,2);

% Sum up the total number of absorbed photons
RT = 0;
for i = 1:n-1
    % sum = Q(i,2)*(Q(i+1,1)-Q(i,1));
     sum =
Q(i,2)*(Q(i+1,1)-Q(i,1))*(1-exp(-5.7e5*sqrt(1243.1/Q(i+1,1)/0.92-1)*
0.0000003*5));  % G=G0*(1-exp(a0*sqrt(E/E0-1)*d))

    RT = RT + sum;
end
RT = RT + Q(1,2)*(Q(1,1)-E0)+ Q(nf,2)*(E1-Q(nf,1));
% Then the photon generated current density Jsc = am15(Em0,Em1)*1.6e-19
```

Note:

The words after "%" are the explanations for the commands, as defined by Matlab.